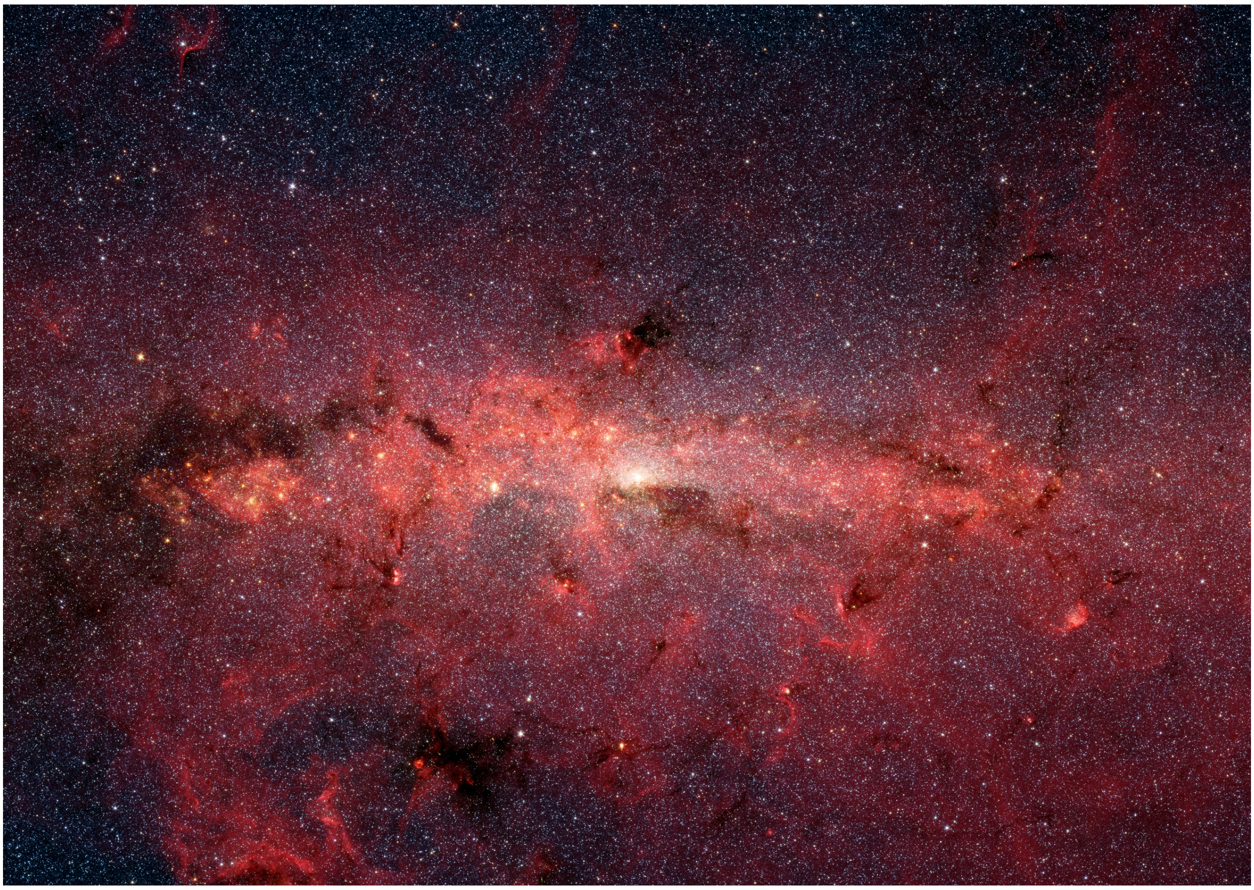

The Core Mass Function in the Galactic Center

Probing Star Cluster Formation in an Extreme Environment

Master's thesis in Physics

ALVA KINMAN

DEPARTMENT OF SPACE, EARTH AND ENVIRONMENT
CHALMERS UNIVERSITY OF TECHNOLOGY
Gothenburg, Sweden 2024
www.chalmers.se

Master's thesis 2024

The Core Mass Function in the Galactic Center

Probing Star Cluster Formation in an Extreme Environment

ALVA KINMAN

Department of Space, Earth and Environment
Division of Astronomy and Plasma Physics
Chalmers University of Technology
Gothenburg, Sweden 2024

The Core Mass Function in the Galactic Center
Probing Star Cluster Formation in an Extreme Environment
ALVA KINMAN

Supervisor: Dr. Maya Petkova
Examiner: Prof. Jonathan Tan

Master's Thesis 2024
Department of Space, Earth and Environment
Division of Astronomy and Plasma Physics
Chalmers University of Technology
SE-412 96 Gothenburg
Telephone +46 31 772 1000

Cover: Spitzer image of the Galactic center. Courtesy NASA/JPL-Caltech.

Typeset in $\LaTeX$
Gothenburg, Sweden 2024

The Core Mass Function in the Galactic Center
Probing Star Cluster Formation in an Extreme Environment
ALVA KINMAN
Department of Space, Earth and Environment
Chalmers University of Technology

Abstract

The Initial Mass Function (IMF) of stars is important for many fields of astrophysics, but its origin is still under debate. Certain star formation theories involve a close connection between the IMF and the Core Mass Function (CMF), which describes the mass distribution of dense cores in molecular clouds. Some early observational results found the CMF to be similar in shape to the IMF, with a high-mass power law index close to the Salpeter value of 1.35. However, in recent years, CMFs of some more distant star-forming regions have been reported that differ from the Salpeter IMF. Here we study the CMF of three clouds in the Central Molecular Zone (CMZ): G0.253+0.016 ("The Brick"), Sgr B2 (Deep South field) and Sgr C. We use Band 6 continuum images from the Atacama Large Millimeter/submillimeter Array (ALMA) archive and identify cores as peaks in thermal dust emission via the dendrogram algorithm. A total of 711 cores are found, with masses ranging from 0.4-780 $M_\odot$. Completeness corrections are applied, derived using synthetic core insertion. The synthetic cores are given mass-dependent radii derived from observed core radii. After corrections, a power law of the form $\mathrm{d}N/\mathrm{d}\log M \propto M^{-\alpha}$ is fit to the individual cloud CMFs above 2 $M_\odot$. The three regions are different from each other, with the Brick showing a Salpeter-like power law index $\alpha = 1.21 \pm 0.11$ and the other two regions showing shallower slopes ($\alpha = 0.92 \pm 0.09$ for Sgr C and $\alpha = 0.66 \pm 0.05$ for Sgr B2-DS). The differences in CMF could be related to evolutionary stage of the regions, since the Brick is mostly quiescent while Sgr B2 and Sgr C are known to be actively star-forming. Furthermore, we analyze the spatial distribution of cores, calculating both Q parameter and mass segregation parameter Λ_{MSR} for each region. Sgr C and Sgr B2-DS show signs of mass segregation, but the Brick does not. The results could be explained by a model in which cores grow in mass by accreting from the surrounding clump.

Keywords: core mass function, initial mass function, star formation, Galactic center, Central Molecular Zone.

Acknowledgements

I would like to thank Prof. Jonathan Tan for giving me the opportunity to do this project, as well as for his guidance during its course. I also want to thank my supervisor Dr. Maya Petkova for all her support, and for her comments that helped me improve this thesis. I want to thank Carl and my family for all their encouragement. A special thanks goes out to my grandmother Agnete for being my biggest fan, and expressing her support for me many times during this project.

Alva Kinman, Gothenburg, January 2024

List of Acronyms

Below is the list of acronyms that have been used throughout this thesis listed in alphabetical order:

ALMA	Atacama Large Millimetre and submillimetre Array
CDF	Cumulative Distribution Function
CMF	Core Mass Function
CMZ	Central Molecular Zone
FWHM	Full Width at Half Maximum
IMF	Initial Mass Function
ISM	Interstellar Medium
MLE	Maximum Likelihood Estimator
MSR	Mass Segregation Ratio
MST	Minimum Spanning Tree
RMS	Root Mean Square
SFR	Star Formation Rate
WLS	Weighted Least-Squares

Contents

List of Figures

List of Tables

1

Introduction

Star formation is a fundamental part of astrophysics, and a field that still contains many open questions. The life cycle of stars is a large part of what drives the evolution of galaxies. Stars are born from interstellar gas clouds, spend their lifetime injecting energy in the form of radiation and stellar winds into the galaxy, and end their lives by returning enriched material to the gas clouds. Stars are responsible for the formation of almost all elements that make up the universe. Star formation is also tightly linked to the formation of planets such as the Earth (McKee & Ostriker, 2007). Stars come in a wide range of masses, from a tenth of a solar mass to a few hundred solar masses. However, all stars do not form with the same probability. Stars with masses of 0.2-0.3 $M_\odot$ are most common, while stars with tens of solar masses are few and far between. Even though the large stars are much more massive individually, the majority of the stellar mass in a galaxy is found in low-mass stars.

1.1 The initial mass function

The distribution describing the probability of stars forming with different masses is known as the Initial Mass Function, often shortened to the IMF. At high masses ($\gtrsim 1\ M_\odot$) it can approximately be described as a power law, with the number of stars formed at each mass given by $\frac{\mathrm{d}N}{\mathrm{d}M} = M^{-2.35}$ (Salpeter, 1955). Understanding the origin of the IMF is an important part of star formation theory.

In addition to being interesting in its own right, the IMF is of vital importance to many areas of astrophysics. When observing distant galaxies, it is not possible to resolve individual stars. We can only observe the sum of all stellar light, which is dominated by the massive stars. To use this light to infer information about all the stars in the galaxy, such as the total stellar mass or the star formation rate, we need knowledge of the IMF (Hopkins, 2018). The IMF is also important for understanding how the abundance of different elements in a galaxy evolves with time. The IMF is needed to predict the number of stars that become supernovae and enrich the interstellar gas with heavy elements (Hopkins, 2018).

1.2 The core mass function

To understand how the IMF gets its shape, we need to turn to the regions where stars form and study the initial conditions. Stars are born from the Interstellar Medium (ISM): the gas and dust that is found between the stars.

The ISM consists mainly of hydrogen (70 % by mass) and helium (28% by mass). The remaining 2% of the mass consists of heavier elements, that can be found both in the gas phase and in dust grains (Draine, 2011). The ISM has different phases, characterized by different temperatures and densities. Stars are formed in molecular clouds, which represent the coldest, densest phase of the ISM. Here, most of the hydrogen is in molecular form (Draine, 2011). Molecular clouds are not uniform, but contain local dense regions known as clumps and cores. The clumps are large enough to form entire star clusters. A clump contains several cores, which are smaller-scale overdensities that can form one or a few stars. The initial masses of stars may be linked to the mass distribution of the cores.

The Core Mass Function (CMF) is the distribution of masses of dense cores in molecular clouds. Like the IMF, it follows a power law at high masses (Offner et al., 2014). Currently there are two important open questions about the CMF. The first question is whether the CMF in universal, or if it varies with the environment. Does the density, temperature, magnetic field strength and other physical conditions influence the masses of cores, or are the physical processes that form them independent of such variations? The second question is how the IMF and CMF are related to each other. Is the mass of each star directly proportional to the mass of the core it was born from, or is the relationship between core and stellar masses more complicated? The shape of the CMF compared to the IMF can help distinguish between different theories of star formation (Offner et al., 2014). To answer these questions, the CMF must be studied in different Galactic environments.

Studying the CMF poses great observational challenges. Firstly, the individual cores need to be resolved, which places high demands on angular resolution. Secondly, the mass surface density of cores is usually calculated using thermal dust emission. Converting flux density to mass requires assumptions about temperature and dust properties. Thirdly, the cores are usually identified by some peak-finding algorithm. The number and masses of identified cores depend on the algorithm used (Offner et al., 2014). The algorithms are likely to miss smaller cores, which leads to a biased core mass function. In order to obtain an accurate CMF, it is essential that we quantify the biases of the algorithm and correct them.

1.3 The Central Molecular Zone

The Central Molecular Zone (CMZ) is the main region that will be studied in this thesis. The CMZ is a region around the Galactic center with a radius of $\sim$ 300 pc (Henshaw et al., 2023). An overview of the region can be seen in Figure 1.1. The molecular clouds belonging to the CMZ are asymmetrically distributed around the supermassive black hole Sgr A*. Some notable structures are the Dust ridge (including the clouds Sagittarius B2 and the Brick), the Sagittarius A clouds and Sagittarius C. The physical conditions in the region are extreme. Gas densities, pressures, magnetic field strengths, turbulent motions and temperatures are several times greater than those in the solar neighborhood (Henshaw et al., 2023). The conditions are similar to those found in high-redshift galaxies (Kruijssen & Longmore, 2013). Studying the CMZ will not only provide information about our own galaxy, but can also help us understand star formation earlier in the history of the universe.

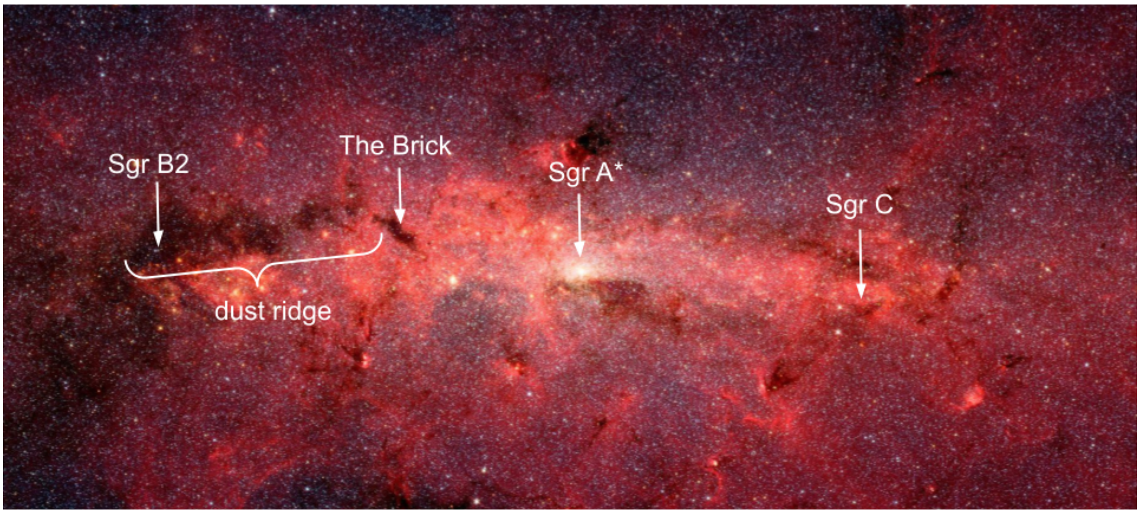

Figure 1.1: Infrared image of the CMZ taken by the Spitzer telescope. The wavelengths shown are 3.6 μm (blue), 4.5 μm (green), 5.8 μm (orange), and 8.0 μm (red). Courtesy of NASA/JPL-Caltech.

Despite the high densities, the star formation rate in the CMZ is lower than expected. Several studies agree on a star formation rate for the CMZ of 0.07 $M_\odot$/year (Henshaw et al., 2023, and references therein). This is inconsistent with star formation laws, that relate the star formation rate to the mass surface density of gas. For example, the star formation law by Lada et al. (2010) states that the star formation rate per area is proportional to the mass surface density of gas above a certain threshold. When comparing the CMZ to this relation, it deviates with about an order of magnitude (Longmore et al., 2013; Lu et al., 2019). Below follows a summary of the properties of the three CMZ clouds studied in this work.

"The Brick", formally known as G0.253+0.016, is an infrared dark cloud belonging to the dust ridge. With its mass of $\sim 10^5$ $M_\odot$ and radius of $2-3$ pc, it is one of the densest and most massive molecular clouds in the Galaxy (e.g. Lis et al., 1994; Longmore et al., 2012; Kauffmann et al., 2017). Despite this, few signs of ongoing star formation have been found in the Brick (Mills et al., 2015). However, recently the Brick has been discovered to harbor at least one forming star cluster (Walker et al., 2021). The low levels of star formation may be caused by the high levels of turbulence (Federrath et al., 2016). Turbulent motions can counteract gravity and prevent the gas from collapsing into stars (Hennebelle & Falgarone, 2012).

Sgr B2 is a molecular cloud complex with a mass of 7×10^6 $M_\odot$ within a radius of 38 pc (Schmiedeke et al., 2016). Sgr B2 is one of the most active massive-star-forming regions in the Galaxy, but despite this, the star formation rate in Sgr B2 is lower than expected from common star formation laws (Ginsburg et al., 2018). It has an average number density of $\sim 10^3$ cm^{-3} while the central part has a number density of $\sim 10^5$ cm^{-3}. Embedded in the central region are dense clumps with sizes of ~ 0.5 pc and number densities of 10^7 cm^{-3}. The clumps host both dense cores, protostars and HII regions. HII regions are formed around massive stars (O and B type), when the strong UV radiation from the star ionizes the surrounding gas. There are three local hotspots with significant star formation, located along a north-south line (Schmiedeke et al., 2016). Only the southern of these hotspots is included in the mosaic analyzed in this work. However, widespread massive star formation has also been found away from these hotspots, including in the deep south region (Sgr B2-DS) studied in this work (Ginsburg et al., 2018).

Sgr C has a mass of approximately 2×10^4 $M_\odot$ and a radius of ~ 2 pc (e.g. Kauffmann et al., 2017; Battersby et al., 2020). The region has been found to harbor star formation. For example, Lu et al. (2019) detected a number of water masers, which they attribute to protostellar outflows. A few potential ultra-compact HII regions were also detected, which indicates that the region is forming massive stars. Furthermore, Lu et al. (2019) found that a larger fraction of the gas in Sgr C is bound, compared to the Brick or Sgr B2.

1.4 Aim and outline

The aim of this thesis is to study the core mass function in the Central Molecular Zone. Data from the Atacama Large Millimeter/submillimeter Array (ALMA) will be used to derive core masses in the Brick, Sgr B2 and Sgr C from thermal dust emission. Cores will be identified with the dendrogram algorithm (Rosolowsky et al., 2008), following the methods of Cheng et al. (2018), Liu et al. (2018) and O'Neill et al. (2021) (hereafter Paper I, II and III). These works all applied completeness corrections to their CMFs, derived through inserting synthetic cores with the same shape as the beam and investigating how well the algorithm recovered them. We aim to extend their methods of completeness correction, by allowing the radius of the inserted cores to vary. This will make the shape of the synthetic cores more representative of the real cores in the image. We will then compare the CMFs for the different regions to each other and to the results of Paper I-III, thus exploring the impact of environmental conditions on star formation.

In Chapter 2, relevant theory and previous studies are summarized. Chapter 3 explains the analysis methods, including the new method for completeness correction of the CMF. Chapter 4 presents the results, including obtained CMFs in the Central Molecular Zone, reanalyzed data from previous papers as well as some analysis of the spatial distribution of cores. In Chapter 5, the implications of the results are discussed, and conclusions are presented.

2

Theory

This chapter aims to give an overview of star formation, the current knowledge of the initial mass function (IMF) and core mass function (CMF). A brief introduction to radiative transfer theory and interferometry is also provided.

2.1 Star formation: an overview

Star formation is the topic of a large body of ongoing research. Core mass function studies form a small piece of the puzzle, attempting to shed light on the initial conditions. This section will provide a brief overview of how a star is formed.

Stars are born in molecular clouds, which represent the coldest, densest phase of the ISM. Here, most of the hydrogen is in molecular form. These clouds typically extend 10-50 pc with masses of 10^2-10^6 $M_\odot$. Their number densities are above 10^3 cm^{-3} and their temperatures usually range from 10-100 K (Girichidis et al., 2020). Molecular clouds are not uniform, but contain local dense regions known as clumps and cores. In order for a star to form, the gravitational force must overpower the thermal, magnetic and turbulent pressures that keep the core from collapsing.

2.1.1 Gravitational instability

There are a few ways to determine if a core is susceptible to gravitational collapse. One of them is the Jeans instability criterion. Assume that we have a uniformly distributed gas. The gas is then perturbed so that it becomes compressed in a certain region. If the perturbation is small enough, acoustic waves will spread out from the compressed region and return the gas to equilibrium. If the perturbation is sufficiently large however, gravity from the compressed region will attract more gas, and the overdensity will grow (Choudhuri, 2010). This instability was first demonstrated by Jeans (1929). Using conservation of mass, conservation of momentum and the gravitational potential, it is possible to derive a Jeans length, i.e. a minimum length scale that makes an accumulation of gas gravitationally unstable. A derivation can be found in Draine (2011). The Jeans length is given by

$$\lambda_J = \frac{2\pi}{k_J} = \left(\frac{\pi}{G\rho_0}\right)^{1/2} c_s \tag{2.1}$$

where G is the gravitational constant, ρ_0 is the gas density and c_s is the sound speed. If we assume the gravitationally unstable region to be spherical and uniform with diameter λ_J, we can derive a Jeans mass:

$$M_J = \frac{\pi^{5/2}}{6} \left(\frac{k_B T}{G\mu} \right)^{3/2} \frac{1}{\rho_0^{1/2}} \tag{2.2}$$

where T is the gas temperature, k_B is Boltzmann's constant and μ is the mean mass of the gas particles.

A gas cloud that has a size larger than the Jeans length λ_J, or a mass larger than the Jeans mass M_J, is likely to undergo gravitational collapse. Note that a higher temperature hinders collapse (since the Jeans mass is made larger) while a higher density facilitates collapse.

The Jeans instability criterion is derived using several simplifying assumptions, such as assuming uniform density and no magnetic fields. A slightly more general result is the virial theorem, which states that

$$2 < E_{KE} > +3 < \Pi - \Pi_0 > + < E_{mag} - E_{mag,0} > + < E_{grav} >= 0 \tag{2.3}$$

for a system in steady state (derived in (Draine, 2011)). Here, $<>$ denotes time averages, E_{KE} is the kinetic energy of the system, E_{grav} is the gravitational energy, $E_{mag} = \int \frac{B^2}{8\pi} \mathrm{d}V$ is the magnetic energy and $\Pi = \int p \mathrm{d}V$ is an integral over the pressure inside the system. Furthermore, $\Pi_0 = p_0 V$ and $E_{mag,0} = \frac{B_0^2}{8\pi} V$, where p_0 and B_0 are values at the boundary of the system and V is the enclosed volume.

In the unmagnetized case without external pressure, the theorem can be simplified to

$$2 < E_K > + < E_G >= 0, \tag{2.4}$$

(Choudhuri, 2010). This simpler form of the theorem allows us to define a virial parameter:

$$\alpha \equiv \frac{2E_K}{|E_G|}. \tag{2.5}$$

With a spherical, homogeneous cloud we obtain $E_G = -\frac{3}{5}\frac{GM^2}{R}$ and $E_K = \frac{3}{2} M\sigma^2$, where M is the mass of the cloud, R is the radius and σ is the one-dimensional velocity dispersion. This means that the virial parameter can be expressed as

$$\alpha = \frac{5R\sigma^2}{GM}. \tag{2.6}$$

A virial parameter close to 1 indicates that the cloud or core is gravitationally bound. If $\alpha \gg 1$ the core is unbound, and must either be held together by external pressure or disperse on a short timescale.

2.1.2 Core collapse and accretion

If the supporting pressure of a core is too small to withstand gravity, the core will start to collapse. As it collapses, heat will be generated. However, initially the extra heat can be radiated away by molecular line emission, effectively keeping the gas at a constant temperature (Shu et al., 1987). As seen in Equation (2.2), the Jeans mass decreases when the gas gets denser as long as the temperature stays the same. That means that the core may start to fragment into smaller pieces, each collapsing on its own. Fragmentation slows down once the infalling gas becomes optically thick, which prevents heat from escaping.

Cores typically rotate slowly, due to turbulence. When material is falling inwards, conservation of angular momentum causes the gas to rotate faster. The result is that a flat disk forms around the central object (Krumholz, 2015, Ch. 15). In order for the orbits of the disk material to be stable, the material further in has to rotate faster than the material further out. This follows from Kepler's third law. But in order for the gas to accrete onto the central protostar, the inner parts of the disk must somehow lose angular momentum. Although there are several possible mechanisms for this, one important process is the magneto-rotational instability (McKee & Ostriker, 2007; Krumholz, 2015, Ch. 15). As portions of gas at adjacent radii shear in relation to each other, magnetic field lines are stretched. This causes a magnetic tension, that strives to stop the shearing. This speeds up the outer gas and slows down the inner gas, transporting angular momentum outwards. The gas that is slowed down will no longer be able to remain in orbit. It falls in towards the center of the disk, where a hot, dense protostar is forming. During the accretion process, jets of material are launched from the accretion disk due to magnetic forces (Krumholz, 2015, Ch. 15). The temperature and density of the protostar increases as more gas is accreted. Eventually it becomes hot and dense enough for hydrogen fusion to begin, and the star enters the main sequence.

The above process describes the formation of a low mass star. Whether high mass stars are formed similarly or by a different process is a topic of ongoing research. There are a few problems that could hinder massive stars to form in this way. Firstly, there is a fragmentation problem. If a massive core contains several Jeans masses, it could start to fragment while collapsing, forming several low mass stars instead of one massive (Tan et al., 2014). Secondly, there is the so called radiation pressure problem. Massive stars contract faster than low-mass stars, which means that they enter the main sequence while still actively accreting. The UV radiation that the star emits exerts a pressure on the infalling material, halting the accretion (Kahn, 1974; Wolfire & Cassinelli, 1987). This would make it very difficult for the most massive observed stars to form. Any theory describing massive star formation would need to tackle these problems.

2.1.3 Formation scenarios for massive stars

There are two main theories describing massive star formation. On the one hand, we have core accretion models. According to these models, massive, gravitationally bound cores are needed to form massive stars. Each core collapses monolithically into one or a few stars, similarly to the formation of low-mass stars. These models assume that the efficiency of converting core mass to stellar mass is roughly constant for all stellar masses (Tan et al., 2014). A notable difference between high mass cores and low mass cores is that turbulence may dominate over thermal motions in high mass cores. To describe the high mass case, McKee & Tan (2003) developed the Turbulent Core Accretion model. Their model predicts an accretion rate that is high enough to overcome the radiation pressure of the forming star. To avoid fragmentation of massive cores, a few different solutions have been presented. For example, Tan et al. (2013) argued that magnetic support can hinder the fragmentation. Another suggestion is that accretion radiation from surrounding protostars may heat the core, leading to a higher Jeans mass and thus preventing fragmentation (Krumholz & McKee, 2008). Another solution to the radiation pressure problem has also been suggested: Protostellar outflows. As found by e.g. Krumholz et al. (2005); Rosen & Krumholz (2020), the outflows that are launched from the poles of the protostar sweep up dust and gas, creating optically thin channels that the radiation can escape through. This alleviates the radiation pressure on the gas and dust accreting from other directions, and decreases the importance of radiation pressure in the formation of a massive star.

On the other hand, there are competitive accretion models (e.g. Bonnell et al., 1997, 2001). These models describe star formation within a cluster, where material for each protostar is not only drawn from the parent core, but can be accreted from a larger part of the clump. The most gas is accreted onto the stars in the center of the forming cluster, since they are located in the deepest part of the gravitational potential well. If the protostars are sufficiently close together, stellar collisions may make the central stars even more massive. The final mass of each star is not determined by the initial core mass. In order for massive stars to form by competitive accretion, no massive, gravitationally bound, starless cores need to exist, which means that the fragmentation problem can be avoided.

2.2 The initial mass function

The initial mass function (IMF) of stars is the mass distribution of newly formed stars, i.e. the fraction of stars that are formed within each mass interval. A number of analytical forms of the IMF have been suggested. For stars more massive than a few solar masses, the distribution approximately follows a power law. This power law was first proposed by Salpeter (1955), and is still widely referenced today. It takes the form

$$\frac{dN}{dM} \propto M^{-2.35}, \tag{2.7}$$

where dN is the number of stars that have masses between M and $M + \mathrm{d}M$. It is often presented in its logarithmic form:

$$\frac{dN}{d\log M} \propto M^{-1.35}. \tag{2.8}$$

When plotted on logarithmic axes, the power law turns into a line with slope -1.35. The power law index can therefore be referred to as the “slope” of the IMF.

Since this relation diverges when M approaches zero, the power law behavior cannot continue down to arbitrarily small masses. Observations have shown that the IMF has a turning point, found to be at approximately 0.2 $M_\odot$ in nearby regions (Offner et al., 2014). This has led to other analytical forms being proposed, such as a log-normal distribution (Miller & Scalo, 1979), or a segmented power law (Kroupa, 2001). These are shown in Figure 2.1.

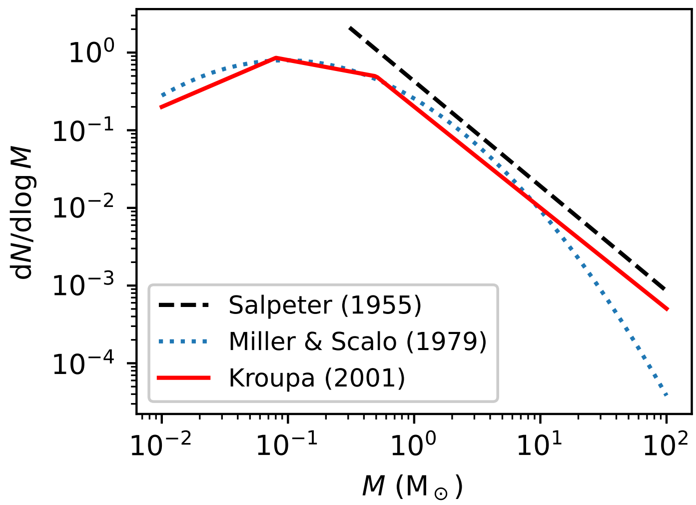

Figure 2.1: Different functional forms of the IMF. The IMFs by Kroupa (2001) and Miller & Scalo (1979) have been normalized.

2.2.1 Observations of the IMF

The IMF is difficult to observe for several reasons. The method of observing the IMF of resolved stellar populations is as follows: First, one determines a luminosity function of a complete sample of stars. Then, the luminosity is converted into present day mass using stellar models. Lastly, the present day mass function must be converted into an initial mass function. A number of factors such as stellar evolution, star formation history and binarity must then be taken into account (Offner et al., 2014). The IMF can also be observed for unresolved stellar populations, but more indirectly. The mass of a galaxy can be estimated from dynamics, and a mass-to-light ratio can be calculated. It can then be compared to population synthesis models, assuming an IMF (Offner et al., 2014).

For the field stars in the Milky Way, the observed IMF follows a Salpeter power law above 1 $M_\odot$, but is significantly flatter below. A segmented power law or log-normal distribution with peak at 0.2 $M_\odot$ works well to describe it (Offner et al., 2014). Young, nearby clusters have similar IMFs. The observations made up until a decade ago therefore pointed towards a universal IMF in the local universe. On this basis, the IMF is often assumed to be universal, even in high-redshift galaxies (Hopkins, 2018).

In the past decade, several studies have found different IMFs in a variety of environments. Schneider et al. (2018) studied a stellar cluster in the Large Magellanic

Cloud. The CMF was found to be top-heavy, i.e. containing more high-mass stars than predicted by the Salpeter power law. The power law index was $\alpha = 0.9^{+0.37}_{-0.26}$. Lu et al. (2013) derived an IMF for the Nuclear Star Cluster around Sgr A*, and obtained a top-heavy IMF with $\alpha = 0.7 \pm 0.2$. A similar result was found in the Arches cluster, located in the CMZ, with $\alpha = 0.8 \pm 0.08$ (Hosek et al., 2019). Other studies have instead found bottom-heavy IMFs, both in nearby galaxies (e.g. Ferreras et al., 2013; Cheng et al., 2023) and high redshift galaxies (e.g. van Dokkum et al., 2017).

2.3 The core mass function

In order to fully understand star formation, we need to study the initial conditions. These are described by the core mass function (CMF), which is the distribution of masses of prestellar cores. Just like the IMF, the high-mass end of the core mass function can be modeled by a power law of the form

$$\frac{\mathrm{d}M}{\mathrm{d}\log M} \propto M^{-\alpha}. \tag{2.9}$$

By observing the similarities or differences between the CMF and IMF, current models of star formation can be tested. In addition, if we were able to understand how the CMF arises and how it is connected to the IMF, we would be able to theoretically predict the IMF in different environments. This could decrease the large uncertainties that are currently introduced into studies of unresolved stellar populations, when a universal IMF is assumed.

2.3.1 Observations of the CMF

Observations of the CMF entail different difficulties than observations of the IMF. Instead of bright point sources, we are observing cold, extended cores embedded within molecular clouds. This puts large requirements on resolution, to be able to separate the cores from each other at long wavelengths. Furthermore, cores have a continuous density distribution that blends with the background cloud and neighboring cores. Observationally, cores are typically defined using an overdensity-finding algorithm. The results can be strongly dependent on which algorithm is used (see e.g. Paper I).

Due to these difficulties, the first observation of the CMF was done by Motte et al. (1998), more than 40 years after the publication of Salpeter's IMF power law. The early studies were limited to regions in the solar neighborhood, i.e. a few hundred parsec from the sun. Motte et al. (1998) identified approximately 60 cores in the ρ Ophiuchi cloud complex. A similar study was made by Testi & Sargent (1998) in the Serpens cloud. These pioneering studies were followed up by studies with larger samples. André et al. (2010) and Könyves et al. (2015) studied approximately 500 cores in the Aquila rift, obtaining significantly better statistics. The conclusion of all these studies was that the local CMF has a similar shape as the IMF, but is shifted towards higher masses by a factor 3 (Offner et al., 2014).

In recent years, with the development of interferometry allowing higher angular resolution, the study of the CMF has been extended to more distant parts of the Galaxy. Motte et al. (2018) studied the massive, star-forming cloud W43-MM1, at a distance of 5.5 kpc. They derived a top-heavy CMF with a slope of 0.96 ± 0.13. Top-heavy CMFs have also been found in infrared dark clouds (IRDCs) (Kong, 2019; Sanhueza et al., 2019), although Salpeter-like CMFs in IRDCs have also been reported (e.g. Ohashi et al., 2016).

Recently, the ALMA-IMF collaboration conducted an extensive study of the core mass function in the massive star-forming W43 cloud complex (Pouteau et al., 2022, 2023; Nony et al., 2023). Pouteau et al. (2022) reported that the total CMF of the region was top-heavy, with a slope of $0.93^{+0.07}_{-0.10}$. Pouteau et al. (2023) went on to divide the cloud complex into six different regions, deriving local CMFs for each. The core mass function was found to vary from Salpeter-like to significantly top-heavy between the different regions. A correlation was found between the evolutionary stage of the region and the core mass function. Quiescent regions tended to have CMF slopes close to 1.35, while regions undergoing star formation had shallower slopes. Additionally, Nony et al. (2023) divided the total core sample into prestellar and protostellar cores, using the absence or presence of protostellar outflows. The prestellar core sample was found to have a Salpeter-like CMF slope, meaning that the top-heavy shape of the total CMF was correlated with the protostellar cores.

In conclusion, there is a growing body of indications that the CMF slope differs from the Salpeter value in some environments. However, it may be misleading to directly compare the values of the power law indices from different studies, since both core-finding algorithms and fitting methods vary. As mentioned in the aim of the thesis, this work builds on a series of papers: Cheng et al. (2018) (Paper I), Liu et al. (2018) (Paper II) and O'Neill et al. (2021) (Paper III). These papers aimed to characterize the CMF in different Galactic environments, using standardized methods that allowed the CMFs to be compared to each other. Paper I studied the CMF in a massive protocluster at a distance of approximately 2.5 kpc and found 76 cores. They obtained a CMF power law index of 1.24 ± 0.17 for masses above 1 $M_\odot$, consistent with the Salpeter slope. Paper II studied the CMF in a sample of seven IRDCs, with distances between 2.4 and 5 kpc from the sun. They found a slightly shallower CMF slope, $\alpha = 0.70 \pm 0.13$. Finally, Paper III used data from the ALMAGAL survey to study the CMF in a sample of 28 clumps in massive protoclusters. They derived a high-mass slope of $\alpha = 0.94 \pm 0.08$, and also found indications of a break in the power law between 5 and 15 $M_\odot$.

2.3.1.1 The core mass function in the CMZ

There have been a few previous studies investigating cores in the Central Molecular Zone. A recent study of the CMF was made by Lu et al. (2020). The paper focused on Sgr C, the 20 km/s and 50 km/s clouds (belonging to the Sgr A cloud complex) and Sgr B1-off (part of the dust ridge). The images were taken by ALMA and had an angular resolution of $\sim 0.2''$, which is higher than in this work. The CMFs for the different regions were found to be slightly top-heavy, with slopes in the range

$0.83 - 1.07$. In particular, Sgr C had a CMF slope of $\alpha = 1.00 \pm 0.13$, starting from a minimum mass of 6.26 $M_\odot$.

Williams et al. (2022) also derived a high-resolution core mass function in the CMZ. Their paper examined "cloud d", located in the dust ridge. 96 cores were detected by dendrogram at the 3σ level, but only 9 at the 5σ level. The study did not find any evidence of star formation in the cloud, and a virial analysis showed that most of the detected cores were unlikely to be gravitationally bound. The core mass function in cloud d was found to be bottom-heavy compared to the Salpeter IMF.

In conclusion, there are some indications that the CMF has different slopes in different parts of the CMZ. In agreement with other recent CMF results, there may be a tendency towards shallow CMF slopes in massive star-forming regions.

2.3.2 Origin of the CMF

One aim of observing the CMF is of course to understand the physics behind its origin. Most of the attempts at predicting the CMF analytically build on supersonic turbulence. Turbulence describes random, macroscopic fluid motion, in contrast to thermal motion happening at microscopic scales. The motions of a fluid must adhere to the momentum conservation equation

$$\frac{\partial}{\partial t}(\rho \mathbf{v}) = -\nabla \cdot (\rho \mathbf{v}\mathbf{v}) - \nabla P + \rho \upsilon \nabla^2 \mathbf{v} \tag{2.10}$$

(Krumholz, 2015, Ch. 4). The right hand side contains three terms. The first describes advection, or momentum flow in and out of a point. The second describes change in momentum due to pressure forces, and the third describes momentum redistribution due to viscosity. Viscosity is the effect of momentum diffusion between adjacent fluid elements, and causes bulk motion to be converted into random motion (Krumholz, 2015, Ch. 4). Two numbers important to describe turbulence are the Mach number, $\mathcal{M} = V/c_s$, and the Reynolds number, $Re = LV/\nu$. The Mach number is defined as the ratio between the characteristic velocity and the sound speed. It determines the importance of the pressure term in the momentum equation. A low Mach number means large pressure term. The Reynolds number is defined in terms of the characteristic velocity scale, length scale and kinematic viscosity ν of the fluid. It determines the importance of the viscosity term, such that a low Reynolds number leads to a large viscosity term. Effectively, the Reynolds number defines a length scale where viscosity becomes important. Flows at larger scales do not lose energy, while flows at smaller scales are damped (Krumholz, 2015, Ch. 4). In the interstellar medium, the Reynolds number is typically very large.

To describe turbulence, the structure of the velocity field is important. Starting from a velocity field $v(r)$ as a function of position, one can take the absolute value squared of its Fourier transform: $\Psi(k) = |\tilde{v}(k)|^2$ (Krumholz, 2015, Ch. 4). This defines the power spectrum. The power spectrum provides the fraction of the power that is present in motions at each wave number $k = 2\pi/\lambda$, i.e. at each length scale. The power spectrum will look different depending on if the turbulence is subsonic or supersonic.

In the subsonic case, Mach number is low which means that pressure is important. The fluid is non-compressible and the density is relatively uniform. In this case, the power spectrum is proportional to $k^{-5/3}$. In the supersonic case on the other hand, the pressure term becomes unimportant. The high velocity gas motions will create shocks that compress the gas locally and form large density contrasts. Since the velocity field will resemble a number of step functions, its power spectrum becomes proportional to k^{-2} (Krumholz, 2015, Ch. 4). This leads to a log-normal density distribution, meaning that the probability for each point (or mass element) to have a specific density follows a log-normal distribution.

One of the first turbulence-based models for the CMF was created by Padoan et al. (1997). They simulated supersonic turbulent flows, and obtained a log-normal density distribution. They then assumed that dense regions would collapse if their mass exceeded the thermal Jeans mass. The Jeans mass is proportional to $\rho^{-1/2}$, as seen in Section 2.1.1. The relation between the Jeans mass and the density allowed them to derive the mass distribution of the collapsing cores. The distribution turned out to be log-normal, similar to the IMF proposed by Miller & Scalo (1979). This work was built on by Padoan & Nordlund (2002). Instead of simulating turbulence, they took an analytical approach. As starting point, they took a power spectrum of power law form. They assumed that cores would form from the compressed sheets of gas created by shocks, and that the core size would be determined by the sheet thickness. With this approach, they derived a CMF with a slope close to the Salpeter slope. By varying the mean density, they could obtain various locations of the distribution peak, but the high mass slope was unaffected. This work thus predicted a universal CMF slope.

Another analytical model was proposed by Hennebelle & Chabrier (2008), and later developed by Hopkins (2012). It uses the Press & Scheckter formalism, first developed for cosmology. Hennebelle & Chabrier (2008) predicted a power law slope of the CMF. Finally, Hopkins (2012) used excursion set theory to determine not only the CMF, but the mass function of gigantic molecular clouds. Hopkins (2012) predicted a uniform CMF slope within the galaxy.

In summary, most models predict a uniform CMF slope. The models mentioned here cannot explain the indications of top-heavy CMFs observed in distant regions.

2.3.3 Connection between IMF and CMF in different star formation scenarios

A central question for the theory of star formation is how the CMF and the IMF are connected. How the CMF and IMF relate to each other depends on the processes by which stars form. According to the core accretion model (e.g McKee & Tan, 2003), each core collapses monolithically into one or a few stars. If the accretion efficiency is the same for all cores, this would predict an IMF that has the same shape as the CMF. These models are consistent with observations in the solar neighborhood if the star formation efficiency is around 0.3 (Offner et al., 2014).

In the competitive accretion scenario, there is no direct mapping between the mass of a core and the mass of the star that forms from it. This means that the CMF and IMF do not necessarily have the same shape. For example, if the accretion rate is proportional to the stellar mass, the IMF would be top-heavy compared to the CMF (Pouteau et al., 2022).

However, a recent work by Pelkonen et al. (2021) indicates that it could be possible for the CMF to resemble the IMF for a stellar population even if there is no relation between individual core and stellar masses. Pelkonen et al. (2021) performed a star formation simulation in a molecular cloud with supersonic turbulence. The star formation was found to be chaotic, with most of the stars accreting mass from a much larger region than their progenitor core. More than 50 percent of the mass of each star originated outside of the core, with the percentage being highest for massive stars. The star formation thus resembled the competitive accretion scenario rather than monolithic core collapse. Despite this, the resulting CMF and IMF had similar slopes to each other. Surprisingly, they also peaked at similar mass, instead of having a factor 3 shift as the local observations indicate. The authors conclude that the CMF models by Hennebelle & Chabrier (2008) and Hopkins (2012) may be incomplete, since they assume isolated cores. It also shows that it is possible for core masses and stellar masses to follow the similar distributions, even if stars do not form from single, collapsing cores.

In conclusion, theoretical models predict relations between the CMF and IMF, that can be tested by observations. The slope of the CMF can provide clues about the star formation process. Furthermore, the theoretical models generally predict a universal CMF, independent of environment and location in the galaxy. As mentioned in Section 2.3.1, some observations indicate that the CMF is not universal. If the CMF does depend on density, temperature, magnetic fields and other physical conditions, observing the CMF in a variety of environments is crucial to develop new models.

2.4 Mass estimates using radiative transfer

Most observations of the CMF build on using thermal dust emission as a probe for gas mass. In order to convert from brightness to mass surface density, radiative transfer theory is needed.

A central quantity for this theory is the specific intensity I_ν of radiation. The specific intensity is defined as emitted power per area per unit bandwidth per unit solid angle and is often measured in units of Jy/beam (which corresponds to 10^{-26} W/m^2/Hz/beam solid angle). Radiation passing through a medium is governed by the radiative transfer equation:

$$\mathrm{d}I_\nu = -I_\nu \alpha_\nu \mathrm{d}s + j_\nu \mathrm{d}s. \tag{2.11}$$

α_ν is the attenuation coefficient, has units 1/length and describes the effect of absorption and stimulated emission. j_ν is the emissivity coefficient, has units power per unit frequency, volume and solid angle and describes the effect of spontaneous emission in the material (Draine, 2011, Ch. 7). The subscript ν indicates that the quantities vary as a function of frequency. s denotes the path length traveled through the material. The equation is often written in terms of the optical depth τ_ν, which is defined as

$$\tau_\nu = \int \alpha_\nu \mathrm{d}s \tag{2.12}$$

Changing variables to $\mathrm{d}\tau_\nu = \alpha_\nu \mathrm{d}s$, and defining the source function $S_\nu = j_\nu/\alpha_\nu$, the equation can be rewritten as

$$\mathrm{d}I_\nu = -I_\nu \mathrm{d}\tau_\nu + S_\nu \mathrm{d}\tau_\nu. \tag{2.13}$$

We can then apply Kirchoff's law:

$$S_\nu = B_\nu(T_{exc}),$$

which states that the source function is equal to the blackbody specific intensity at the excitation temperature of the material. The blackbody specific intensity is given by the Planck function:

$$B_\nu(T) = \frac{2h\nu^3}{c^2}\frac{1}{e^{h\nu/k_B T} - 1}. \tag{2.14}$$

Finally, we assume a uniform temperature T and local thermodynamic equilibrium, which implies $T_{exc} = T$. This leads to a simplified solution to the radiative transfer equation:

$$I_\nu = I_\nu(0)\mathrm{e}^{-\tau_\nu} + B_\nu(T)(1 - \mathrm{e}^{-\tau_\nu}). \tag{2.15}$$

Under the assumption that the material is optically thin, that is, $\tau \ll 1$, an additional simplification can be made:

$$I_\nu \approx I_\nu(0) + B_\nu(T)\tau_\nu. \tag{2.16}$$

There is a proportionality between optical depth τ and mass surface density of dust Σ_d: $\tau_\nu = \kappa_{\nu,dust}\Sigma_d$. The proportionality constant $\kappa_\nu, dust$ is known as the dust opacity coefficient. The dust opacity coefficient depends on the size and composition of the grains and can be obtained from models (see e.g. Ossenkopf & Henning, 1994). Since we are interested in the total mass of a core and not only the dust mass, we also need to know the dust-to-gas mass ratio. This can be obtained empirically or from from models. Then we can calculate the total dust opacity coefficient, given by

$$\kappa_\nu = \frac{M_{dust}}{M_{gas} + M_{dust}}\kappa_{\nu,dust} \tag{2.17}$$

We can now obtain the formula relating total mass surface density Σ to specific intensity of dust emission. If the background term $I_\nu(0)$ is assumed to be negligible, we can rearrange Equation (2.16) to get

$$\tau_\nu = \frac{I_\nu}{B_\nu(T)} \implies \Sigma = \frac{F_\nu}{\Omega\kappa_\nu B_\nu(T)}. \tag{2.18}$$

Here we have rewritten the specific intensity I_ν as the flux density F_ν divided by the solid angle Ω over which F_ν is measured.

2.5 The principles of interferometry

This thesis uses observations made by the ALMA telescope, which is a radio interferometer. To allow the reader to understand the properties and potential problems of the data, a brief overview of the technique is provided here.

An interferometer consists of multiple telescopes working together. The angular resolution that can be achieved by a single-dish telescope is given by

$$\theta \approx \frac{\lambda}{D}, \tag{2.19}$$

where λ is the wavelength of the radiation and D is the diameter of the dish (Condon & Ransom, 2016, p. 126). Technical concerns limit the size of radio telescopes, and thus the achievable angular resolution. But by connecting multiple telescopes, separated from each other by large distances, it is possible to create the illusion of a much larger dish.

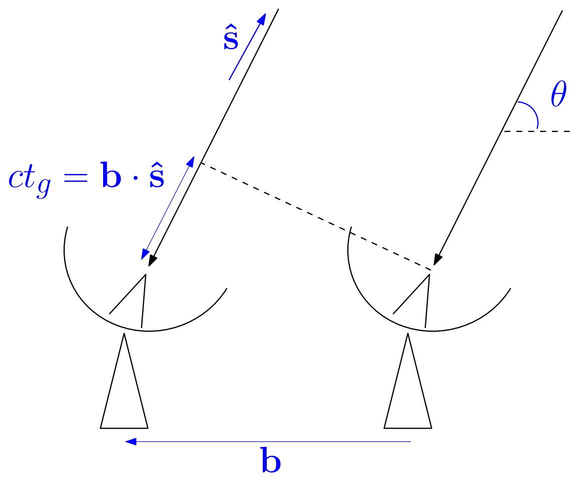

Figure 2.2: Illustration of the basic principle of a 2-antenna interferometer.

In principle, an interferometer uses the time difference between the signals recorded by different telescopes to determine the angle of the source. Consider two antennas separated by a baseline $\vec{b}$ (see Figure 2.2). The source is located in the direction $\hat{s}$. An electromagnetic plane wave from the source reaches both antennas, but due to the location of the source, the signal to one of the antennas is delayed by a time t_g. Antenna 1 will output the voltage $U_1 \propto Ee^{i\omega t}$, while Antenna 2 will output the voltage $U_2 \propto Ee^{i\omega(t-t_g)}$, where E is the electric field strength. The signals are then cross-correlated. In practice, this is achieved by multiplication followed by integration over a time T much larger than the period (Wilson et al., 2013, p. 240-241):

$$R(t_g) = \int_0^T U_1(t)U_2^*(t-t_g)\mathrm{d}t \propto \frac{E^2}{T}\int_0^T e^{i\omega t}e^{i\omega(t-t_g)}\mathrm{d}t \tag{2.20}$$

Since the integration time T is set to be much larger than the period $2\pi/\omega$, we will obtain approximately the same result by integrating over a single period:

$$R(t_g) \propto E^2 \frac{\omega}{2\pi} \int_0^{2\pi/\omega} e^{i\omega t_g} \mathrm{d}t = E^2 e^{i\omega t_g}. \tag{2.21}$$

Since the geometric time delay t_g can be expressed as $t_g = \vec{b} \cdot \hat{s}/c$, we see that the correlated signal contains information about both the direction $\hat{s}$ of the source and its brightness I (since $I \propto E^2$). In addition to the source properties, the response is also affected by the effective collecting area $A(\hat{s})$ of each antenna in the direction $\hat{s}$ (Wilson et al., 2013, p. 241). If the source is extended, we can treat it as consisting of a number of point sources, and get the response

$$\begin{aligned} R \propto \iint_\Omega A(\hat{s}) I(\hat{s}) e^{i\omega t_g} \mathrm{d}\Omega = \iint_\Omega A(\hat{s}) I(\hat{s}) e^{i\omega(\vec{b}\cdot\hat{s}/c)} \mathrm{d}\Omega = \\ = \iint_\Omega A(\hat{s}) I(\hat{s}) e^{i2\pi(\vec{b}\cdot\hat{s}/\lambda)} \mathrm{d}\Omega \equiv \mathcal{V}(\vec{b}) \end{aligned} \tag{2.22}$$

where Ω is the solid angle of the source and $\hat{s}$ is the direction vector towards different parts of the source. $\mathcal{V}$ is known as the complex visibility (Wilson et al., 2013). We obtain different visibility values for each baseline, i.e. for each pair of antennas with a unique separation vector. By using an array of antennas with different distances from each other, the visibility function is sampled in a large number of points.

To obtain the brightness distribution $I'(\hat{s}) = A(\hat{s})I(\hat{s})$, an inverse Fourier transform is needed. The transform goes from the so called *uv* plane, where (u, v) are coordinates of the baselines, to the image plane, where (x, y) are angular coordinates on the sky. However, since we only have finitely many samples of the visibility (determined by the number of unique baselines), we are missing information about the function we are transforming. Each point in the *uv* plane corresponds to a spatial frequency. The spatial frequencies that do not have measured visibilities will be missing in the image.

For an intuitive understanding, note that small scales in Fourier space correspond to large scales in regular space, and vice versa. If no long baselines are observed, small structures in the image will not be detected. The angular resolution is approximately determined by the longest baseline, $\theta_{min} \approx \lambda/b_{max}$. Similarly, if no short baselines are observed, extended structures in the image will not be detected. This means that an interferometer, in contrast to a single-dish telescope, has a maximum recoverable scale $\theta_{max} \approx \lambda/b_{min}$ determined by the shortest baseline. Emission that is uniform over scales larger than this will be filtered out from the image (Wilson et al., 2013, p. 246). This point is important when interpreting interferometric observations.

The image we obtain after inverse Fourier transformation is known as the dirty image, since it is distorted by the missing spatial frequencies. The observed visibility function is a product between the true visibility and the baseline pattern (where the baseline pattern is taken to be 1 in the points corresponding to the observed baselines and 0 in all other points). A product in Fourier space corresponds to a convolution in regular space. This means that the dirty image is a convolution between the true image and the dirty beam, or Point Spread Function (Wilson et al., 2013, p. 269).

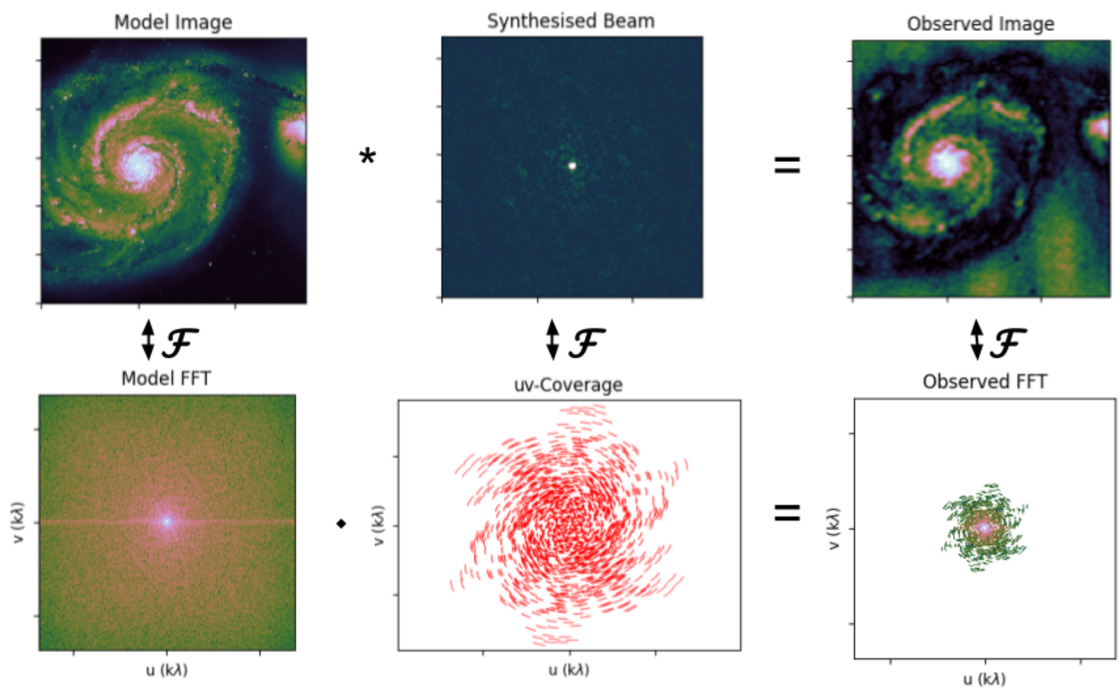

Figure 2.3: Illustration of the concepts of interferometry. The true image convolved with the synthesized beam (P_D) gives the observed (dirty) image. The bottom row is related to the top row by Fourier transform, and the corresponding relation holds: The true visibility multiplied by the uv coverage gives the observed visibility. Images created with the Friendly Virtual Radio Interferometer, Copyright 2017 - 2022 Cormac R. Purcell and Roy Truelove.

The point spread function (P_D) is the Fourier transform of the baseline pattern, and the interferometer's response to a point source. The relation between the different quantities in xy and uv space are visualized in Figure 2.3, and can be written as follows.

$$\mathcal{V}_{obs}(u,v) = \mathcal{V}_{true}(u,v)\tilde{P_D}(u,v) \xrightarrow{\mathcal{F}^{-1}} I_{dirty}(x,y) = I'(x,y) * P_D(x,y) \tag{2.23}$$

To obtain the true image, deconvolution is needed. Unfortunately the problem lacks a unique solution, since several intensity distributions could produce the same sample of visibilities. However, there are several algorithms developed for finding a likely solution, for example the CLEAN algorithm (Högbom, 1974).

Finally, the obtained clean image needs one last correction. As one can see in Equation (2.22), the quantity we get from the inverse transform of $\mathcal{V}$ is $I'(x,y) = A(x,y)I(x,y)$, where $I(x,y)$ is the true brightness distribution of the source. $A(x,y)$ is known as the primary beam response, depends on the antenna properties and needs to be divided by to obtain the true brightness distribution (Wilson et al., 2013, p. 252).

3

Methods

The methods used in this thesis build on the core extraction methods used by Cheng et al. (2018), Liu et al. (2018) and O'Neill et al. (2021) (Paper I, II and III). In this chapter, the observational data used in this work will first be presented. Then, the method of identifying cores via the dendrogram algorithm will be described. This method is the same as in the three papers. Furthermore, the methods of flux and number correction will be described. Here this work differs from Paper I, II and III since the corrections are modified to take the typical radius of the cores into account. Thereafter, some statistical tools used for analyzing core mass functions are presented. Finally, methods for examining the dense gas fraction and the spatial distribution of cores are introduced.

3.1 Observations

The data was obtained by the Atacama Millimeter and Sub-millimeter Array (ALMA). ALMA is a radio interferometer consisting of 66 antennas, located on the Chajnantor Plateau in Chile. 50 of the antennas belong to the so called 12 m array, where each telescope dish has a diameter of 12 m. It is this array that has been used to capture the data used in this thesis. The antennas in the 12 m array can achieve separations up to 16 km. The remaining antennas have diameters of 12 or 7 m and belong to the Compact Array. These have shorter separations, and can be used together with the 12 m array to compensate for the missing short baselines (Cortes et al., 2023).

Continuum images obtained by the 12 m array in receiver band 6 were used. Mosaics of the three regions the Brick, Sagittarius B2 Deep South (hereafter Sgr B2-DS) and Sagittarius C were obtained from the ALMA archive with IDs 2012.1.00133.S, 2017.1.00114.S and 2016.1.00243.S respectively. The central wavelengths of the images were 1.16 mm for the Brick and 1.33 mm for Sgr B2 and Sgr C. The original Full Width at Half Maximum (FWHM) beam sizes for the images were $1.03'' \times 0.855''$ for the Brick, $0.46'' \times 0.37''$ for Sgr B2 and $0.80'' \times 0.60''$ for Sgr C. The most important properties are summarized in Table 3.1. More technical details can be found in Appendix A. The three primary-beam-corrected mosaics are shown in Figure 3.1.

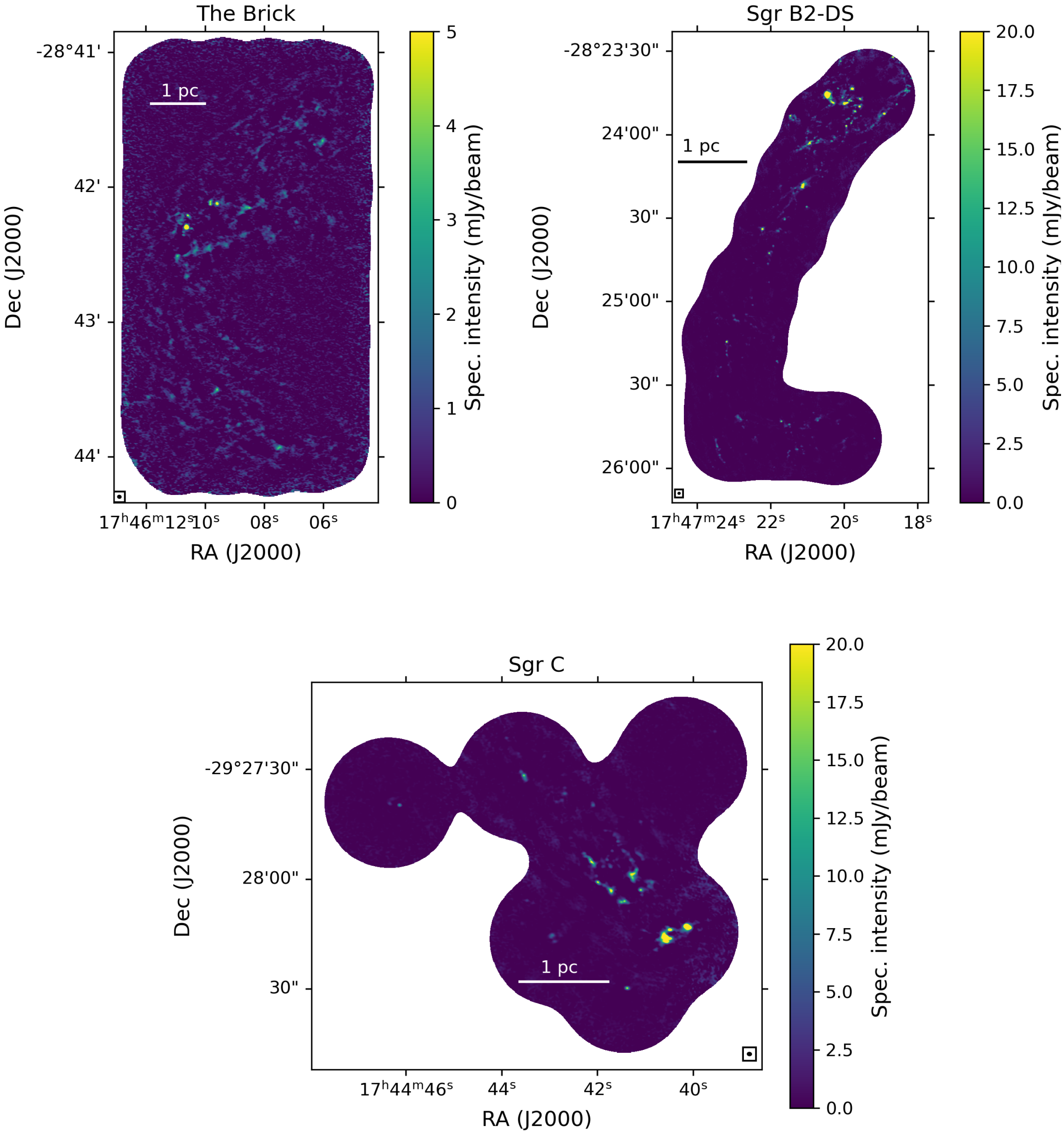

Figure 3.1: ALMA images of the three CMZ regions. Top left: The Brick, top right: Sgr B2-DS, bottom: Sgr C.

Table 3.1: Details of ALMA images.

Region	ALMA ID	Wavelength	Beam size	Max. recoverable scale
The Brick	2012.1.00133.S	1.16 mm	$1.03'' \times 0.855''$	$10.6''$
Sgr B2-DS	2017.1.00114.S	1.33 mm	$0.46'' \times 0.37''$	$6.5''$
Sgr C	2016.1.00243.S	1.33 mm	$0.80'' \times 0.60''$	$6.4''$

It is important to note that the ALMA images are interferometric, and thus large scale emission is missing (see Section 2.5). Emission that is extended over larger angles than the maximum recoverable scale listed in Table 3.1 is filtered out. To estimate the total mass within each region, another dataset is therefore needed. For this purpose, 1.1 mm continuum images from the Bolocam Galactic Plane Survey (Ginsburg et al., 2013) were used. The images have a beam FWHM of $33''$.

3.1.1 Noise

The RMS noise of the ALMA images determines the parameters of the dendrogram algorithm, so an accurate noise estimation is of importance. The calculation was done separately for each non-primary-beam-corrected ALMA image. Firstly, beam-sized patches were randomly placed in the image, and the mean intensity in each patch was obtained. If the mean was larger than 0.1 times the maximum signal in the image, the patch was considered as containing signal and discarded. The final result was found to be insensitive of this threshold. This was repeated 10 000 times. A Gaussian distribution was then fit to the distribution of intensities. The noise dispersion σ was taken to be the standard deviation of the Gaussian. To lessen the effect of random sampling, the above was repeated 100 times and the median of σ was used. The obtained noise levels were 0.174 mJy/beam for the Brick, 0.111 mJy/beam for Sgr B2 and 0.127 mJy/beam for Sgr C. Examples of noise distributions can be seen in Figure 3.2. In the noise distributions for Sgr B2 and Sgr C, a tendency towards non-Gaussian "wings" can be seen. This is likely caused by cleaning residuals around the brightest sources.

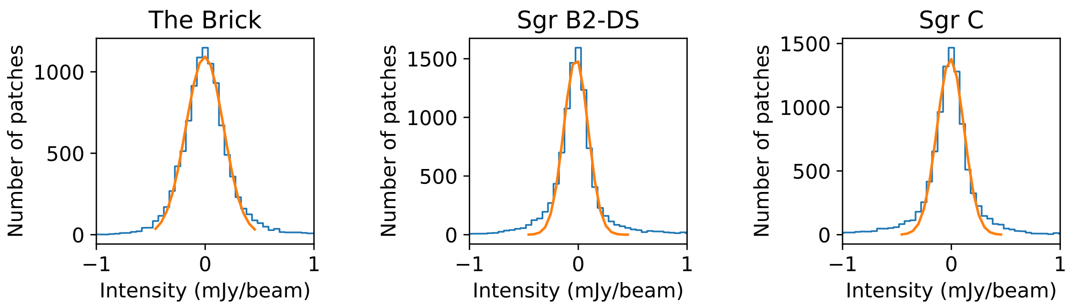

Figure 3.2: Noise distributions (blue) and fitted Gaussians (orange) for the different regions.

3.2 Core identification

Cores were identified using the algorithm dendrogram (Rosolowsky et al., 2008), implemented in the python package `astrodendro`[1]. The choice of algorithm can have a significant effect on the results (see e.g. Paper I). By choosing the same algorithm as Paper I-III, we ensure that our results are comparable to theirs.

Dendrogram identifies peaks in data and sorts them into a hierarchical structure. There are two types of structures: branches, containing multiple sub-structures, and leaves, that contain no sub-structure. Cores were defined as the dendrogram leaves.

The algorithm works as follows. It first locates the brightest pixel in the map, taking this as the starting point of the first leaf. Then it evaluates the next brightest pixel, deciding whether to join it to the existing structure or create a new one. If a local maximum is found, meaning that the pixel value is larger than those of its neighbors, it is taken as the starting point of a new structure. Otherwise, it is joined to the existing structure. The algorithm keeps considering pixels with lower and lower values. If a pixel is found to be adjacent to two different structures, the structures are joined into a branch.

There are a number of parameters that can be set in order to handle noise in the data. Firstly, a minimum value F_{min} can be set. Pixels below this value will not be considered by the algorithm. This prevents identification of background noise as peaks. Secondly, a minimum significance δ_{min} for structures can be set. This means that local maxima that are smaller than this value will not be considered independent structures. Lastly, the minimum number of pixels N_{min} for a structure can be specified. This is useful to exclude structures that are smaller than the synthesized beam.

In this study, the fiducial dendrogram parameters from Paper I, II and III are used: $F_{min} = 4\sigma$, $\delta_{min} = \sigma$ and N_{min}=half the number of pixels in the beam. σ denotes the RMS noise of the image. To calculate N_{min}, the following equation was used:

$$N_{min} = \frac{\pi \theta_{maj} \theta_{min}}{8 A_{pix}}, \tag{3.1}$$

where θ_{maj} and θ_{min} are the major and minor full width half maxima of the beam in arcseconds and A_{pix} is the area of each pixel in arcseconds squared.

Following Paper II and III, cores were identified in the non-primary-beam-corrected images. The non-corrected images have a more uniform noise level, allowing for use of the same dendrogram parameters everywhere in the image. Primary beam correction increases the noise near the edge of an image in particular, which could lead to false core detections there. Furthermore, the detection of cores was restricted to the parts of the mosaic where the primary beam response exceeded 0.5.

[1] `https://dendrograms.readthedocs.io/en/stable/`

3.3 Core mass estimation

Once cores have been identified, the next step is to convert millimeter flux density into mass surface density Σ. This can be done using the following relation, as presented in Section 2.4:

$$\Sigma = \frac{F_\nu}{\Omega \kappa_\nu B_\nu(T_d)}. \tag{3.2}$$

where F_ν is the flux density integrated over the solid angle Ω, κ_ν is the dust opacity coefficient and $B(T_d)$ is the blackbody specific intensity at the dust temperature. This relation can be normalized, resulting in the following equation:

$$\Sigma = 0.369 \left(\frac{F_\nu}{1 \text{ mJy}}\right) \left(\frac{\Omega}{(1'')^2}\right)^{-1} \frac{\lambda_{1.3}^3}{\kappa_{0.00638}} \left[\exp\left(0.553 T_{20}^{-1} \lambda_{1.3}^{-1}\right) - 1\right], \tag{3.3}$$

where $\lambda_{1.3}$ is the wavelength of observation divided by 1.3 mm, $\kappa_{0.00638} = \kappa_\nu/0.00638$ cm^2g^{-1} and $T_{20} = T_d/20$ K. Since we do not have temperature data for each core, a dust temperature of 20 K has been assumed, as in Paper I, II and III. 20 K has been found to be a typical dust temperature of protostellar cores (Zhang & Tan, 2015). It is also consistent with dust temperature measurements for the CMZ (Longmore et al., 2012; Ginsburg et al., 2016; Kauffmann et al., 2017; Santa-Maria et al., 2021). Note that the dust temperature in the CMZ is significantly different from the gas temperature (Ginsburg et al., 2016, and references therein). However, it is possible that the temperature varies among the cores. If a dust temperature of 15 K was assumed instead, it would change the calculated mass by a factor of 1.48 . If the temperature was increased to 30 K, the mass would change by a factor of 0.604. Note that there may be systematic temperature variations: for example brighter cores could be warmer. In that case, the more massive cores would have their masses overestimated.

To get the value of the dust opacity coefficient for 1.3 mm emission, an opacity per unit dust mass $\kappa_{1.3mm,dust} = 0.899$ cm^2g^{-1} was assumed (moderately coagulated thin ice mantle model of Ossenkopf & Henning 1994). The values in Ossenkopf & Henning (1994) are estimated to be accurate within a factor of 2. Using a gas-to-refractory-component-dust ratio of 141 (Draine, 2011), we obtain the opacity coefficient per total mass $\kappa_{1.3mm} = 6.38 \times 10^{-3}$ cm^2g^{-1}. Since the Brick is not observed at 1.3 mm, the value of κ_ν needs to be adjusted. This was done by linear interpolation between the 1.0 mm and 1.3 mm values presented in Ossenkopf & Henning (1994), resulting in $\kappa_{1.16mm} = 7.93 \times 10^{-3}$ cm^2g^{-1}.

To obtain core masses, the mean mass surface density is multiplied by the area of the core:

$$M = \Sigma A = 0.113 \frac{\Sigma}{\text{g cm}^{-2}} \frac{\Omega}{(1'')^2} \left(\frac{d}{1 \text{ kpc}}\right)^2 M_\odot, \tag{3.4}$$

where Ω is the solid angle of the core and d is the distance from the sun. In this work, a distance of 8.3 kpc is adopted for all regions, consistent with the distance of 8277 pc to Sgr A* found by GRAVITY Collaboration et al. (2022). The individual clouds may be displaced along the line of sight on the order of a few hundred pc compared to Sgr A*, but the precise morphology of the CMZ is not settled by the literature (see e.g. Henshaw et al., 2023). Therefore we do not apply individual distances to the regions. An error of 5 % ($\sim$ 400 pc) in the estimated distances results in a $\sim$ 10 % error in the masses.

3.4 Flux and number correction

In order for the obtained CMF to resemble the true CMF, corrections need to be done. Firstly, dendrogram excludes pixels with intensity less than F_{min}. This means that some of the flux of the cores is lost. Secondly, the algorithm may miss small and faint cores entirely. To correct for these two effects, a flux recovery fraction f_{flux} and a number recovery fraction f_{num} are needed. Their behavior could vary in each image, depending on the noise level as well as the degree of crowding. Flux and number recovery fractions can be obtained by core insertion experiments. A number of synthetic cores of a given flux are randomly placed into the image. Then, dendrogram is run on the new image. The fraction of the flux and number of artificial cores recovered gives the value of f_{flux} and f_{num}. This is repeated for a range of fluxes, in order to obtain both f_{flux} and f_{num} as a function of flux (or equivalently, mass).

In previous papers (I, II, III), the synthetic cores were given the same shape as the synthesized beam, in order to represent small, unresolved cores. In this work, we insert cores of more realistic sizes. This is motivated by the observation that a significant number of the identified cores are larger than the beam. Furthermore, there is a positive correlation between estimated core mass and size (see Figure 3.3).

3.4.1 Radius determination

To determine sizes of cores, the radius calculated by the `astrodendro` package was used. `astrodendro` calculates a standard deviation of the flux distribution along the major and minor axis of the core (Rosolowsky et al., 2008). The direction of the major axis is determined by principal component analysis, i.e determining along which direction the variance in position is largest. Once the direction of the major axis has been determined, the major standard deviation σ_{maj} is given by

$$\sigma_{maj}^2 = \frac{\sum I_i (x_{maj,i} - \bar{x}_{maj})^2}{\sum I_i} \tag{3.5}$$

where I_i is the intensity of pixel i, $x_{maj,i}$ is the pixel's position along the major axis, $\bar{x}_{maj}$ is the mean value of x_{maj} and the index i ranges over all pixels within the dendrogram structure. The equation for σ_{min} is analogous. The radius is then calculated as the geometric mean of the major and minor standard deviation: $\sigma_{dendro} = \sqrt{\sigma_{maj}\sigma_{min}}$. This radius measure was chosen over the equal-area radius $R_c = \sqrt{A/\pi}$, since it is easily translated into the size of a synthetic Gaussian core. For a perfectly detected, circular, Gaussian core, σ_{dendro} equals the true standard deviation of the Gaussian.

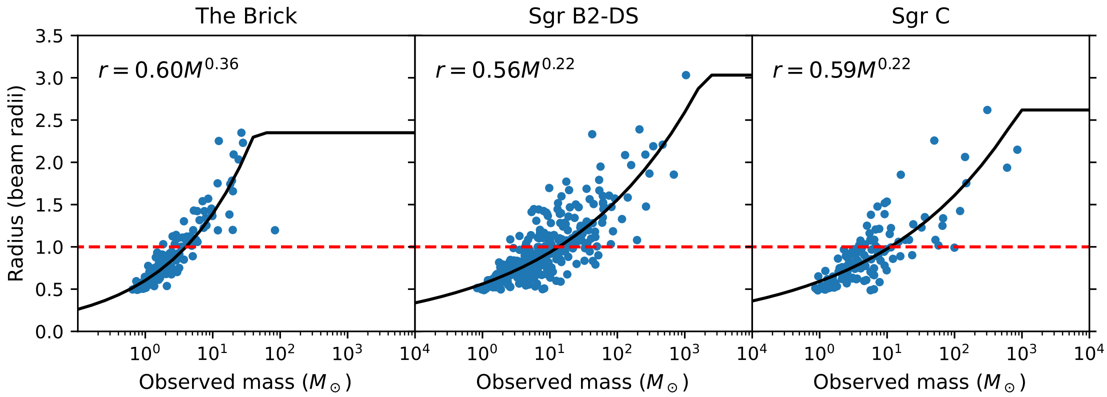

Figure 3.3: Mass-radius relations, before any iterations have been done. While the Brick data shows a strong correlation between mass and radius, the cores in Sgr B2 and Sgr C are more scattered. Note that r in the equation is in units of beam radii, while M is in units of $M_\odot$.

Once the observed mass and radius of each core was determined, a line was fitted to the logarithmic data points (corresponding to a power law in linear space). The radius function was cut off at the radius of the largest observed core, to stop the inserted cores from growing unrealistically large. The obtained power law was then used to determine the size of the synthetic cores. The observed core properties and fitted mass-radius relations can be seen in Figure 3.3. There is a clear trend towards larger radii for more massive cores, although the cores do not follow the power law perfectly. The index of the fitted power law differs between regions. While the Brick has a power law index close to 0.33, as expected if cores have constant density, the other two regions both have a lower power law index of 0.22. The data points of Sgr B2 and Sgr C are also more scattered than those of the Brick.

3.4.2 Iterations

There is a notable caveat with determining core sizes in this way, namely that the mass-radius relation is made from observed masses and radii. For a core insertion experiment, we ideally need to know the true radius of a core with a given true mass. There is no straight-forward way to correct this, since the conversion from observed to true mass requires known flux recovery fractions. To solve this issue, we took an iterative approach.

First, a power law is fitted to observed core properties as described in Section 3.4.1. Then, cores are inserted with radii given by said power law. The flux recovery and radius recovery fractions are calculated, and applied to the masses and radii of observed cores. A new power law is fitted, but this time using the flux-corrected masses and radius-corrected radii. The process is iterated 20 times. Note that the flux and radius corrections are always applied to the observed cores, not the core properties from the last iteration. This means that the masses and radii can both increase and decrease between iterations.

An issue that was seen in early tests of the iterative method is that the flux recovery curve did not converge towards a single result, but rather oscillated between two distinct shapes. To mitigate this issue, a damping step was introduced into the calculation. Instead of feeding the flux recovery from one iteration directly into the next, an average was taken between the previous and new flux recovery:

$$f_{flux,n} = \frac{f_{flux,n,raw} + f_{flux,n-1}}{2}.$$

A few supplementary figures showing the effect of iterations can be found in Appendix B.

3.4.3 Probability distribution

If synthetic cores are inserted uniformly into the image, the results may be biased depending on the amount of empty space in the image. Cores inserted on an empty background are much more likely to be detected than cores inserted in a crowded environment. To mitigate this, cores were inserted according to a probability distribution. To obtain said distribution, the ALMA image of each region was smoothed to a scale of 20″ and normalized. This effectively meant that cores were more likely to be inserted in regions with many other cores. The smoothing scale was chosen to be much larger than a typical core, in order to avoid inserting cores only around the few brightest sources in the image.

3.4.4 Details on core insertion and recovery

Each core insertion experiment consists of inserting three cores of a given flux into the image. The cores are randomly placed according to the probability distribution described above. The number of inserted cores is kept low to avoid unnecessary blending. To get better statistics, the experiment is repeated 100 times. The process is done for a range of logarithmically spaced masses, with 5 mass bins per decade. The bins are centered on 1 $M_\odot$, 10 $M_\odot$, 100 $M_\odot$ etc. After each core insertion, dendrogram is run again. All new cores, i.e. those that do not have an exact correspondence among the old observed cores, are compared to the positions of inserted cores. If the position of an inserted core matches one of the new cores, that core counts as detected. However, if the detected peak also matches with the peak of an old core, and said old core is more massive than the inserted core, the detection is discarded. This is to avoid false detections. If e.g. a 1 $M_\odot$ core is inserted close to the peak of an existing 100 $M_\odot$ core, and the sum of the two cores is detected, it should not count as a detection of a 1 $M_\odot$ core.

The flux recovery fraction f_{flux} is obtained as the median ratio between recovered flux and inserted flux. Cores whose recovered flux is larger than their true flux are not counted. These cores are considered to have falsely assigned fluxes, which could for example happen if a small core is inserted on a noise feature or the edge of a larger core. The number recovery fraction f_{num} is simply obtained as the number of recovered cores divided by the number of inserted cores.

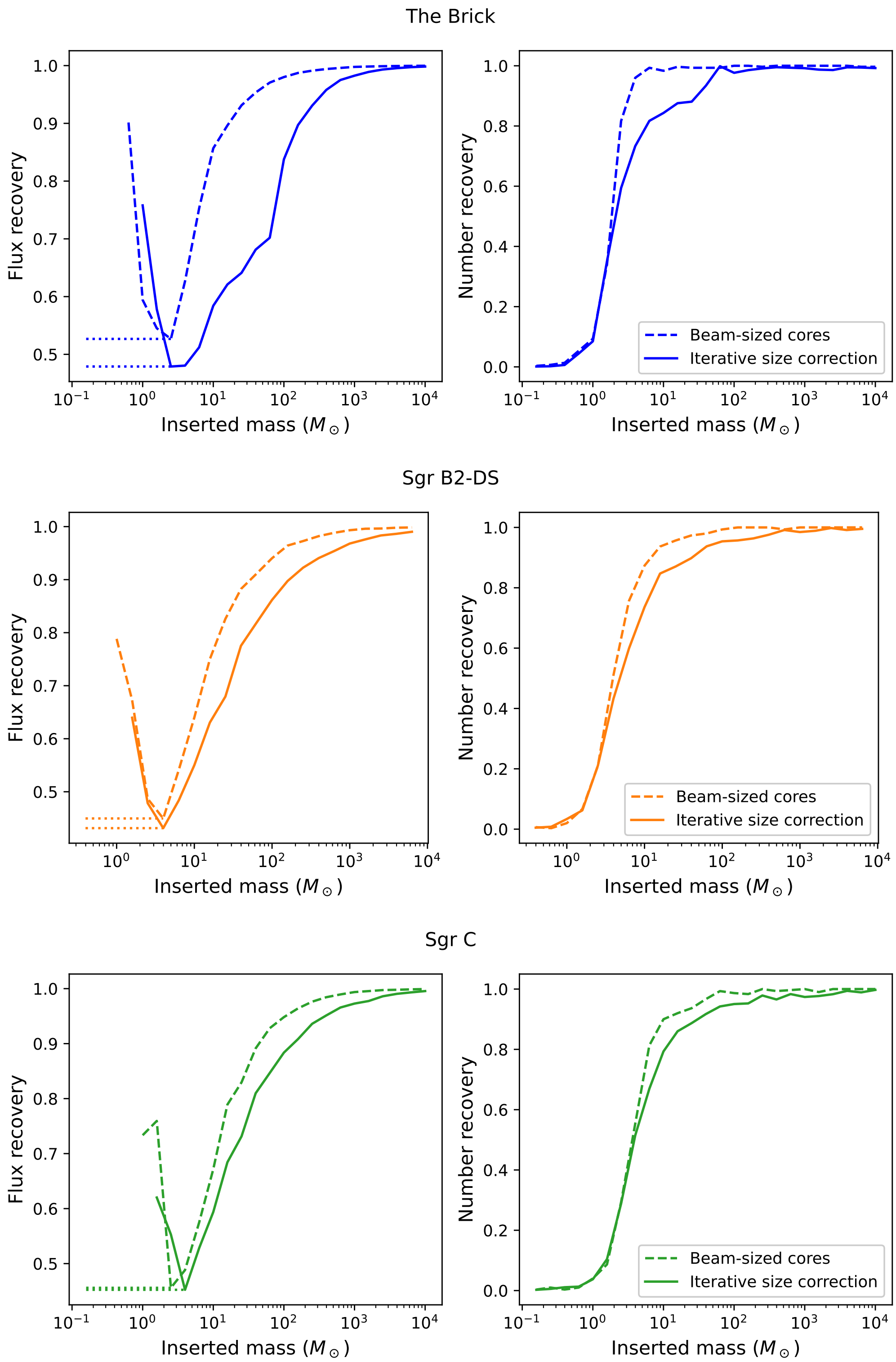

Figure 3.4: Flux and number recovery fractions for the three regions in the CMZ. 20 iterations were performed in the iterative method. When allowing the size of the cores to vary, both flux and number recovery decrease.

3.4.5 Recovery curves

The left column of Figure 3.4 shows the obtained flux recovery fractions for two different core insertion methods: Insertion of beam-sized cores, similar to Paper I, II and III, and iterative core insertion with realistic sizes. The new method gives lower flux recoveries than the insertion of beam sized cores. The effect is most pronounced in the Brick data. This difference is expected. With the new method, core radius increases at the same time as core mass, which means that the peak intensity of the synthetic core increases more slowly than in the beam-sized case. In an ideal situation without noise, the flux recovery of a Gaussian core is directly determined by the peak intensity relative to the dendrogram threshold F_{min}.

For both methods, large values of f_{flux} are obtained for the lowest mass cores. This could be due to noise features getting falsely identified. To remove this effect, masses below the mass with minimum f_{flux} are assumed to have constant f_{flux}. This correction is also done within the iterative process of the realistic size core insertion.

Note that the values on the x axis of Figure 3.4 represent inserted, or “true” mass. In order to correct core masses, true mass must be converted to observed mass. This is done by multiplying the center mass of each bin with the corresponding flux recovery fraction.

The right column of Figure 3.4 shows the number recovery fractions. For all three regions, number recoveries are low for masses below 1 $M_{\odot}$, but thereafter rise quite steeply. For the new method, the number recovery rises more slowly towards unity. Again, this is expected since the cores are flatter, and therefore do not stand out against the background as much as if they had been beam-sized.

3.4.6 Corrections to previous CMFs

In order to compare the results from this thesis to the three previous papers, the developed core insertion method needs to be applied to the regions from Paper I-III. The ALMA data used in Paper I is a single mosaic, so the method described in Section 3.4 can be applied directly. The ALMA data for the regions from Paper II and III consists of numerous single pointings with a small number of cores detected in each. This means that the method developed in this thesis needs a few subtle changes to be applicable. The changes are detailed below.

There are too few cores in each pointing to form a meaningful mass-radius relation. The pointings also have different beams, noise levels, and distances to the source, which means that the flux recovery fraction as a function of mass may be very different for each region. However, as shown in Paper III, recovery curves in different regions become similar if they are expressed as a function of normalized flux instead of mass. The flux value in Jy is normalized by dividing by the noise level σ expressed in Jy/beam.

Instead of a mass-radius relation, a relation between normalized flux and radius (in terms of beam radii) was used to determine the size of the inserted cores in the

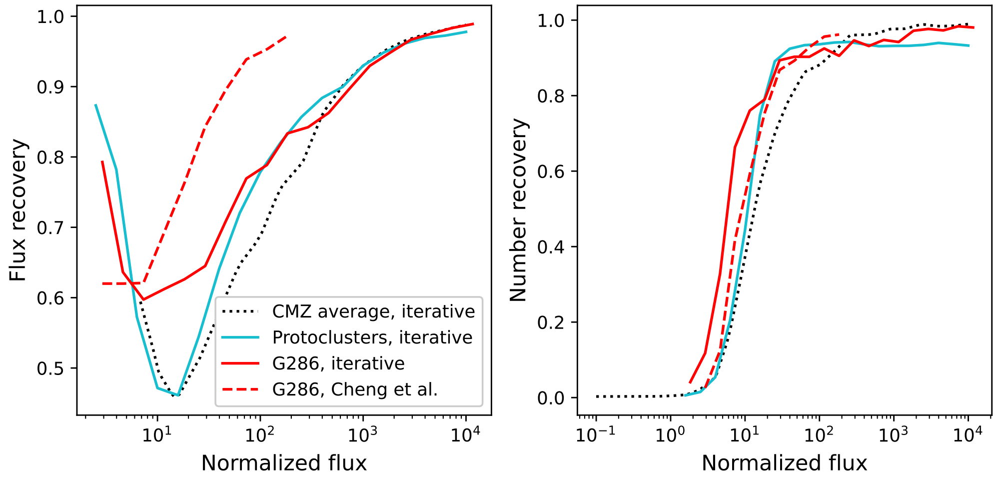

Figure 3.5: Flux and number corrections for G286.21+0.17 and massive protoclusters, as a function of normalized flux. The dotted line shows an average of the three CMZ regions as a comparison. The red dashed line shows the flux and number recovery obtained by Cheng et al. (2018).

ALMAGAL pointings from Paper III. The flux and number recovery curves were calculated as functions of normalized flux, rather than mass. The recovery curves obtained from the ALMAGAL pointings were used to correct the IRDC sample from Paper II as well. Recovery curves for the previous regions can be seen in Figure 3.5.

3.5 Statistics

The quantitative result that is most important for this thesis is the high-mass power law index of the CMF. Two different methods are used to derive the power law index. Firstly, we consider the method used in all three previous papers. The method is to fit a power law to the binned CMF using a weighted least squares (WLS) approach, starting from a predetermined bin. The WLS method aims to minimize the quantity

$$\chi^2 = \sum_i \frac{(y(x_i) - y_i)^2}{\sigma_i^2}, \tag{3.6}$$

where $y(x) = b - \alpha x$ is a straight line in log space, $y_i = \lg(\Delta N/\Delta \lg M)$ is the logarithm of the histogram height of bin i, $x_i = \lg(M_i)$ is the logarithm of the center mass of bin i and σ_i is the error. The error is taken to be the Poisson counting error normalized by the bin width, $\epsilon_i = \sqrt{N_i}/(\Delta \lg M)$. Since a symmetric relative error is needed for fitting in log space, the error σ_i is set to be $\sigma_i = \frac{1}{2} \lg\left(\frac{y_i+\epsilon_i}{y_i-\epsilon_i}\right)$. If a bin is empty, the error is set to be the same as for a bin with one core.

There are however disadvantages with the above described method. It has been argued by e.g. Clark et al. (1999) and White et al. (2008) that a least squares-fit to binned power law data may introduce systematic errors in the slope estimate. Clauset et al. (2009) suggests using a maximum likelihood estimator (MLE) to obtain accurate results. The formula for the MLE is

$$\hat{\alpha} = n \left[\sum_{i=1}^{n} \ln \frac{x_i}{x_{min}} \right]^{-1}, \tag{3.7}$$

with α defined as in Equation (2.9). Note that the definition of α in Clauset et al. (2009) differs by 1 from this work, so the expression presented in their paper looks slightly different. x_{min} is the value of x where the power law behavior starts and n is the number of cores with masses above x_{min}. The standard error is given by

$$\Delta\hat{\alpha} = \frac{\hat{\alpha}}{\sqrt{n}} + \mathcal{O}(1/n). \tag{3.8}$$

This MLE requires individual core masses, not binned data. That means that it is not applicable to the number-corrected CMF, which is only defined by the bin height. Therefore, a second MLE is needed. We use the MLE for binned data presented in Virkar & Clauset (2014) (hereafter called MLE-B). In the case when the bins can be written on the form $(c^s, c^{s+1}, ...c^{s+k})$ (i.e. logarithmically spaced bins), the MLE for the slope is

$$\hat{\alpha} = \log_c \left[1 + \frac{1}{s - 1 - \log_c b_{min} + (1/n) \sum_{i=min}^{k} i h_i} \right]. \tag{3.9}$$

b_{min} represents the minimum bin and h_i represents the number of counts in each bin. The standard error is

$$\Delta\hat{\alpha} = \frac{c(c^{\hat{\alpha}} - 1)}{c^{(2+\hat{\alpha})/2} \ln c \sqrt{n}}. \tag{3.10}$$

Again, note that the definition of α in Virkar & Clauset (2014) differs by 1 from this work.

Furthermore, we would like to assess whether the CMFs are significantly different from each other. This can be done with the Kolmogorov-Smirnov (K-S) test. The K-S statistic is defined as

$$D = max|F_1(M) - F_2(M)|, \tag{3.11}$$

where F_1 and F_2 are cumulative distribution functions. A lower value of D means larger similarity between the distributions. From the value of D and the number of samples, a p-value can be calculated. The p-value represents the probability that two sets of samples would be more different than the evaluated ones, if drawn from the same distribution. A low p-value thus indicates that the two sample sets are more different than what would be expected due to random sampling, and are likely from different underlying distributions. With a high p-value, we cannot reject the hypothesis that the samples are drawn from the same distribution.

3.6 Dense Gas Fraction

The dense gas fraction of a region can be used to determine its evolutionary stage. It indicates the fraction of the gas that is contained within dense cores, and thus available for star formation. In this work, the dense gas fraction is defined as the total mass of the cores divided by the total mass of the region. Note that different definitions can be found in the literature, so comparisons between works should be done with caution. To calculate the total core mass, we use the number-corrected CMF. The mass of the cores in each bin is estimated as the number of cores multiplied by the center mass of the bin.

Furthermore, we estimate the total mass of each region using 1.1 mm continuum images from the Bolocam Galactic Plane Survey, version 2 (Ginsburg et al., 2013). The mass surface density is calculated over the entire ALMA footprint, using Equation (3.3). The mass surface density is then converted to mass using Equation (3.4). $T_d = 20$ K is assumed and κ_ν is obtained in the same way as for the core mass calculation. Note that cores are not detected in the entire ALMA field of view, but only in the region where the primary beam response is above 0.5. Ideally, we would want to match the area over which the mass is measured to the area where cores are detected. However, we want to avoid using a patch from the Bolocam data that is significantly smaller than the beam. Since the Sgr B2 map in particular covers a thin strip, restricting to primary beam response > 0.5 gives a region that is thinner than the Bolocam beam FWHM by a factor of ~ 2. A similar issue arises with the Sgr C map. Therefore, the estimated dense gas fractions are likely underestimations.

3.7 Spatial distribution of cores

In order to connect core observations to theories of star formation, the spatial distribution of cores in the cloud is of interest. In this work, two aspects of the distribution will be quantified: the degree of clustering and the mass segregation.

3.7.1 Q parameter

The Q parameter was introduced by Cartwright & Whitworth (2004) as a quantitative measure of a star cluster's structure. The Q parameter allows us to differentiate clusters with an even, radial distribution from clusters with a clumpy, substructured distribution. In order to define the Q parameter, one must first compute the Minimum Spanning Tree (MST).

The MST is a concept used in graph theory. A spanning tree is a graph that connects all nodes in a sample and contains no cycles. The minimum spanning tree is defined as the spanning tree that minimizes the edge weight. When used for analysis of star clusters, the edge weight is taken to be the projected distance between the sources.

The Q parameter is defined by taking the ratio of two cluster distribution metrics:

$$Q = \frac{\bar{m}}{\bar{s}}. \tag{3.12}$$

$\bar{m}$ is the normalized mean edge length of the MST of the cluster. The purpose of the normalization is that $\bar{m}$ should be the same for clusters with the same distribution, even though one of them may contain more sources. For example, a uniform distribution over a circular area should result in the same value of $\bar{m}$, regardless of if the cluster contains 100 or 10 000 sources. The total length of the MST has been found to be proportional to $\sqrt{AN}$, where A is the projected area of the cluster and N is the number of sources (Beardwood et al., 1959). When the mean length is considered instead of the total length, we also obtain the proportionality constant $\frac{1}{N-1}$, since the MST of N sources has $N-1$ edges. The desired normalization of the mean length thus becomes

$$\bar{m} = \frac{< e > (N-1)}{\sqrt{AN}}, \tag{3.13}$$

where $< e >$ is the mean edge length of the MST, or equivalently

$$\bar{m} = \frac{\sum e_i}{\sqrt{AN}} \tag{3.14}$$

where $\sum e_i$ is the total length of the MST. The area is given by $A = \pi R_{cluster}^2$, where $R_{cluster}$ is the distance between the mean position of the sources and the furthest source.

The $\bar{s}$ parameter is defined as the normalized pairwise mean separation of sources. It is given by

$$\bar{s} = \frac{< d_i >}{R_{cluster}}, \tag{3.15}$$

where d_i is the distance between each pair of sources in the sample. Just like $\bar{m}$, $\bar{s}$ is independent of the number of sources in the cluster (Cartwright & Whitworth, 2004).

A Q parameter above 0.8 indicates that the cluster has a large-scale radial density gradient, while a Q parameter below this value indicates that the cluster is substructured. A lower Q parameter indicates stronger subclustering.

3.7.2 Mass segregation parameter

Mass segregation denotes the tendency of massive objects to be grouped together. To evaluate whether a cluster is mass segregated, the mass segregation parameter Λ_{MSR}, defined by Allison et al. (2009), can be used. Just like the Q parameter, Λ_{MSR} is calculated using minimum spanning trees. To calculate Λ_{MSR}, we first choose the N most massive cores in the sample, and calculate the MST of only those cores. We then choose N cores at random, and calculate the MST of only those cores. Finally, we define the mass segregation parameter as

$$\Lambda_{MSR} = \frac{< l_{random} >}{l_{massive}}, \tag{3.16}$$

where l_{random} and $l_{massive}$ are the total lengths of the MSTs. Since l_{random} depends strongly on the choice of cores, it should be calculated a large number of times, and the mean value $< l_{random} >$ should be used in the calculation. When N is small, the standard error on l_{random} will be large due to stochastic effects. This means that a larger number of calculations is needed to get a stable value. For this reason, 1000 calculations were made when $N \leq 20$, while 100 calculations were made for larger N.

If the cluster is mass segregated, we expect the most massive cores to be closer together than a group of randomly selected cores, giving $\Lambda_{MSR} > 1$. An inversely mass segregated cluster, where the most massive cores are more spaced out than other cores, would have $\Lambda_{MSR} < 1$. More extreme segregation yields values further from 1.

The choice of sample size N is arbitrary and provides the mass segregation on one specific mass scale only. To probe the degree of mass segregation at different masses, many different values of N must be tested.

4

Results

In this chapter, core mass functions for the three regions in the Central Molecular Zone will be presented. Core mass functions for the regions of Paper I-III will also be presented, reanalyzed with the new correction methods. All CMFs will be compared to each other and used to illustrate the impact of the new correction method compared to the old one. Finally, the analysis is extended by examining the dense gas fraction and spatial distribution of cores in the CMZ regions.

4.1 Identified cores

In Figure 4.1, the mosaics of the Brick, Sgr B2-DS and Sgr C are shown, with dendrogram-identified cores marked in red. The number of cores identified were 215 for the Brick, 337 for Sgr B2-DS and 159 for Sgr C.

Due to the resolution constraints, only cores more massive than ~ 0.8 $M_\odot$ could be detected. The smallest mass that can theoretically be observed depends on beam size and noise level. For the dendrogram algorithm to identify a core, it must contain a minimum of one pixel at 5σ level and $N_{min} - 1$ pixels at 4σ level. For the Brick, such a core would have a mass of 0.36 $M_\odot$. After flux correction, the theoretical minimum mass increases to 0.75 $M_\odot$. Corresponding masses for Sgr B2 and Sgr C are 0.35 $M_\odot$ and 0.39 $M_\odot$ in raw mass, and 0.81 $M_\odot$ and 0.87 $M_\odot$ in corrected mass.

Some statistics of the detected cores can be found in Table 4.1. The individual core properties are listed in Appendix C. Notably, the cores in Sgr B2 and Sgr C are generally more massive than in the Brick.

4.2 Core mass functions

The calculated core mass functions for the three regions in the CMZ can be seen in Figure 4.2. The figure shows the "raw" CMF, i.e. before corrections, the flux-corrected CMF, and the number-corrected ("true") CMF. Note that the number-corrected CMF is obtained by applying number correction to the flux-corrected CMF. The binning is the same as in Paper I, II and III: the bins are evenly spaced in log space with 5 bins per decade, and one bin centered on 1 $M_\odot$. The y axis shows the quantity $\mathrm{d}N/\mathrm{d}\log M$, i.e. the number of cores in the bin divided by the

Table 4.1: Data on the detected cores in the CMZ regions. Masses are given in $M_\odot$, and are presented both before flux correction (raw) and after (corr.). Mass surface density is given in g cm^{-2}.

	The Brick	Sgr C	Sgr B2-DS
N_{cores}	215	159	337
M_{min}, raw	0.45	0.51	0.44
M_{min}, corr.	0.95	1.13	1.02
M_{max}, raw	83.79	601.96	756.73
M_{max}, corr.	100.01	623.62	787.67
M_{median}, raw	1.46	3.07	6.29
M_{median}, corr.	3.04	5.92	11.07
Σ_{median}	0.20	0.60	2.56

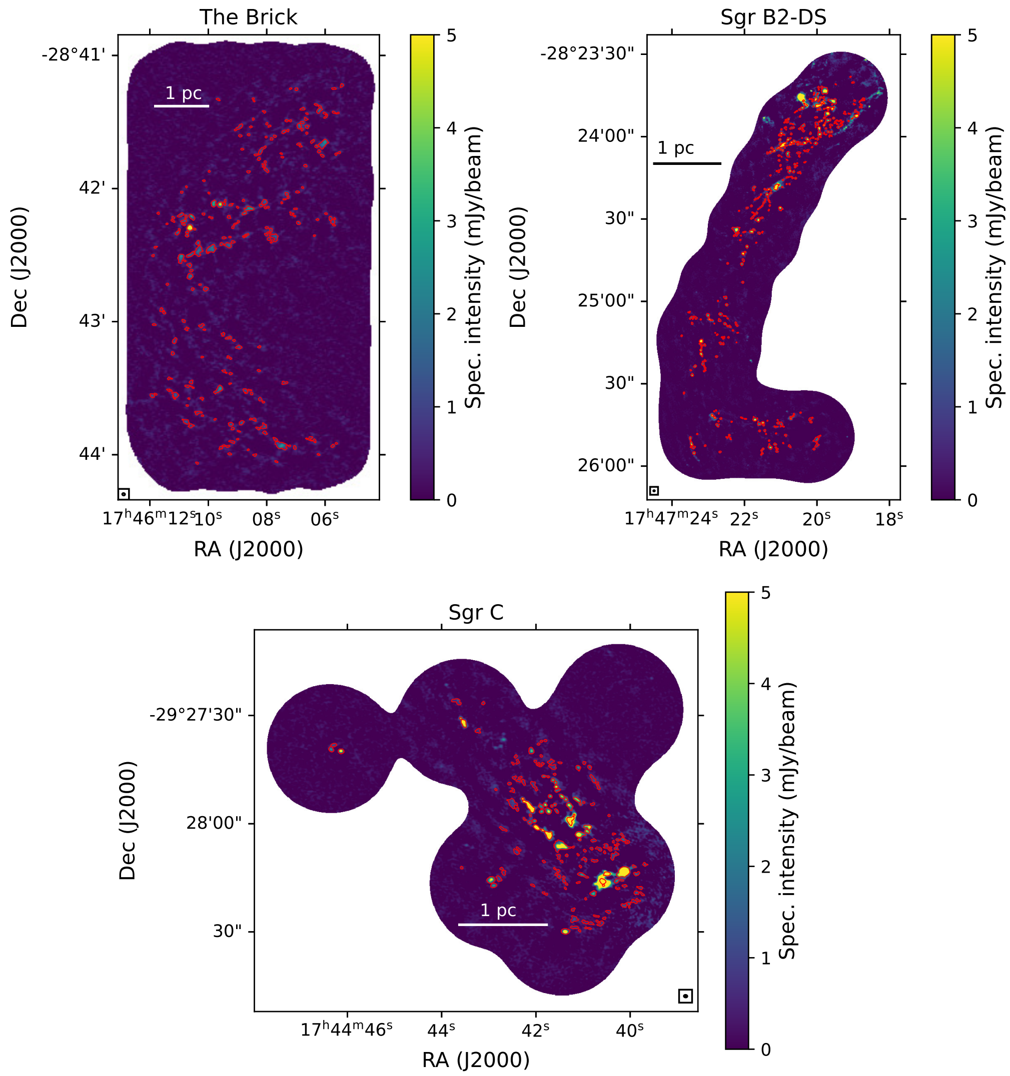

Figure 4.1: Detected cores in the three CMZ regions. Top left: The Brick, top right: Sgr B2-DS, bottom: Sgr C.

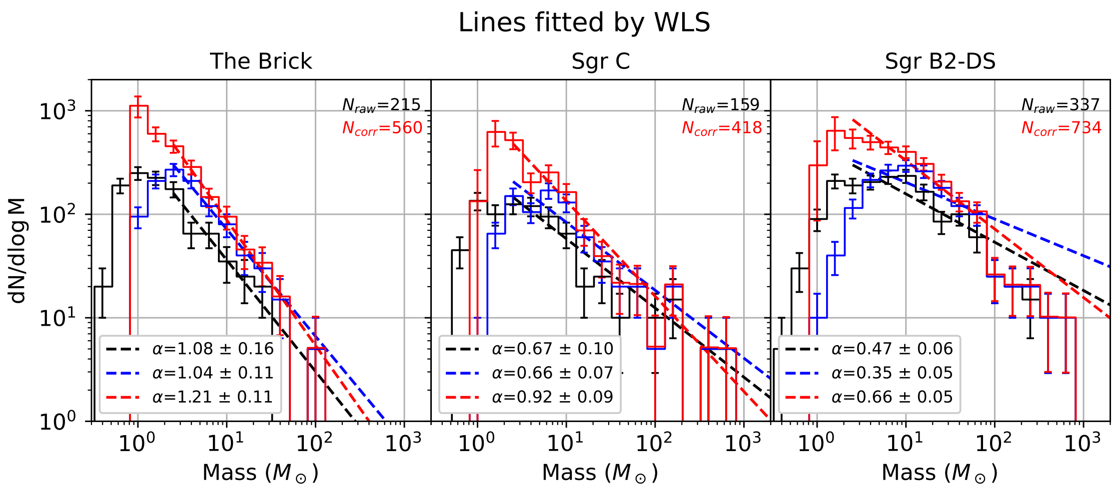

Figure 4.2: Core mass functions for The Brick (left), Sgr C (middle) and Sgr B2-DS (right). The black histogram shows the "raw" CMF, the blue histogram shows the flux-corrected CMF and the red histogram shows the number-corrected CMF. Lines are fitted using the weighted least squares method.

logarithmic bin width. The error bars on the raw and flux-corrected CMF denote $\sqrt{N}$ Poisson counting errors, while the errors on the number-corrected CMF are set to be the same relative size as on the flux-corrected CMF. Note that these do not take the uncertainty in f_{flux} or f_{num} into account.

As can be seen, number correction has a dramatic effect on the low mass end of the core mass function, but a negligible effect on the high mass end. Flux correction on the other hand has an impact on intermediate to high mass bins as well. This is in contrast to the previous method of completeness correction, as is discussed further in Section 4.3.

The power laws in Figure 4.2 are fitted using the weighted least squares method, as described in Section 3.5. The error on α shown in the figure is the standard error of the fit. In Paper I, II and III, the power laws were fitted over a standard range starting at the bin centered at 1 $M_\odot$. However, due to the higher mass sensitivity threshold of the CMFs in this thesis, the starting bin is instead taken to be the bin centered at 2.5 $M_\odot$.

It can be seen that the power law index differs between the different regions. While the true CMF of the Brick has a power law slope of $\alpha = 1.21 \pm 0.11$, which is consistent with the Salpeter slope of 1.35, Sgr B2 and Sgr C have considerably shallower slopes. Their true CMFs have power law indices of $\alpha = 0.66 \pm 0.05$ and $\alpha = 0.92 \pm 0.09$ respectively.

As described in Section 3.5, we also fit power laws using a Maximum Likelihood Estimator (MLE) of the slope. The result from this fit can be seen in Figure 4.3 and Table 4.2. Although the values of α increase slightly compared to the WLS method, the difference in true CMF is within one standard error. The Brick CMF retains a

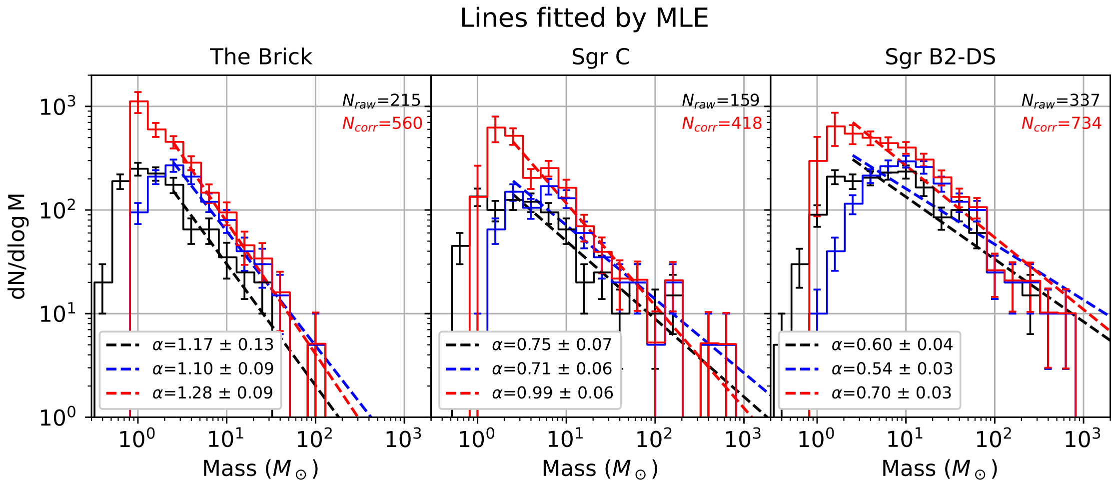

Figure 4.3: Core mass functions for The Brick (left), Sgr C (middle) and Sgr B2-DS (right). The black histogram shows the raw CMF, the blue histogram shows the flux-corrected CMF and the red histogram shows the number-corrected CMF. Lines are fitted using the maximum likelihood estimator method.

Salpeter-like slope while the other two regions have smaller values of α.

In Figure 4.4, the CMFs of the three regions are normalized and plotted together, highlighting the differences between them. Most notably, the Brick is deficient in high-mass cores compared to the other two. In the right panel, the differences in slope are also clearly illustrated.

4.3 Comparison between correction methods

In this section, we investigate the effect on the CMF caused by using the completeness correction method described in this thesis, as opposed to the method used in Paper I-III. In this comparison, we include both the Central Molecular Zone CMFs and the CMFs from Paper I-III. To ensure comparability between CMF slopes, we redo the power law fit to the CMFs from previous papers, starting from the bin centered at 2.5 $M_\odot$.

In Figure 4.5, the flux-corrected CMF is shown for both the old and new method. In Figure 4.6, the number-corrected CMF is shown for the two methods. For the CMZ regions, the "old" corrections are derived by inserting beam sized cores into the image (see dashed curves in Figure 3.4). For the other regions, the old CMFs are taken directly from the respective paper.[1]

We note the new method appears to shift the flux-corrected CMF to higher mass than than the old method. This is especially visible for The Brick and G286.21+0.17,

[1]With the exception of the massive protocluster CMF from Paper III, where the masses have been recalculated due to a previous error.

Table 4.2: Power-law indices for best-fit power laws (starting from 2 $M_\odot$).

CMF	α, WLS	α, MLE	α, MLE-B
The Brick			
Raw	1.08 ± 0.16	1.17 ± 0.13	1.18 ± 0.07
Flux-corrected	1.04 ± 0.11	1.10 ± 0.09	1.13 ± 0.09
True	1.21 ± 0.11	-	1.28 ± 0.09
Sgr B2-DS			
Raw	0.47 ± 0.06	0.60 ± 0.04	0.60 ± 0.07
Flux-corrected	0.35 ± 0.05	0.54 ± 0.03	0.54 ± 0.03
True	0.66 ± 0.05	-	0.70 ± 0.03
Sgr C			
Raw	0.67 ± 0.10	0.75 ± 0.07	0.75 ± 0.07
Flux-corrected	0.66 ± 0.07	0.71 ± 0.06	0.72 ± 0.06
True	0.92 ± 0.09	-	0.99 ± 0.06

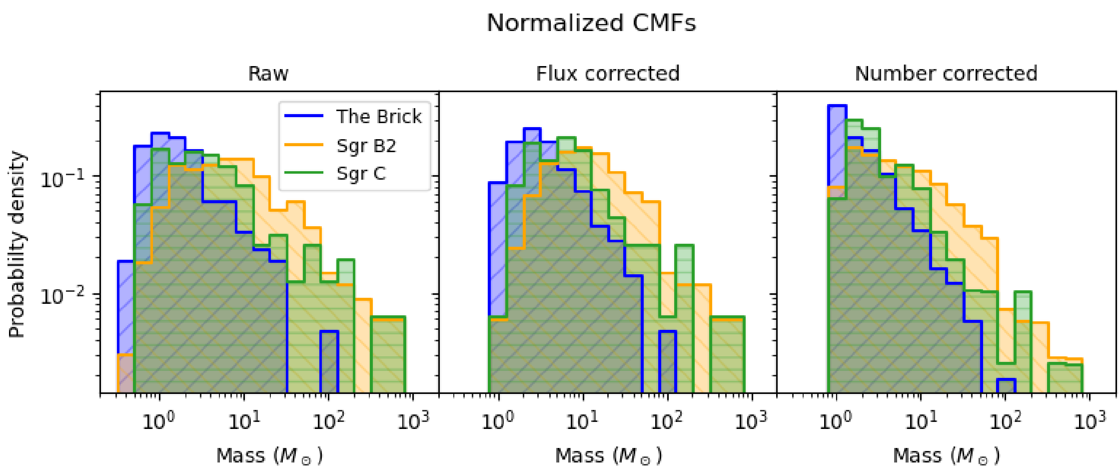

Figure 4.4: Comparison between normalized CMFs. Left: Raw CMFs, middle: flux-corrected CMFs, right: number-corrected CMFs.

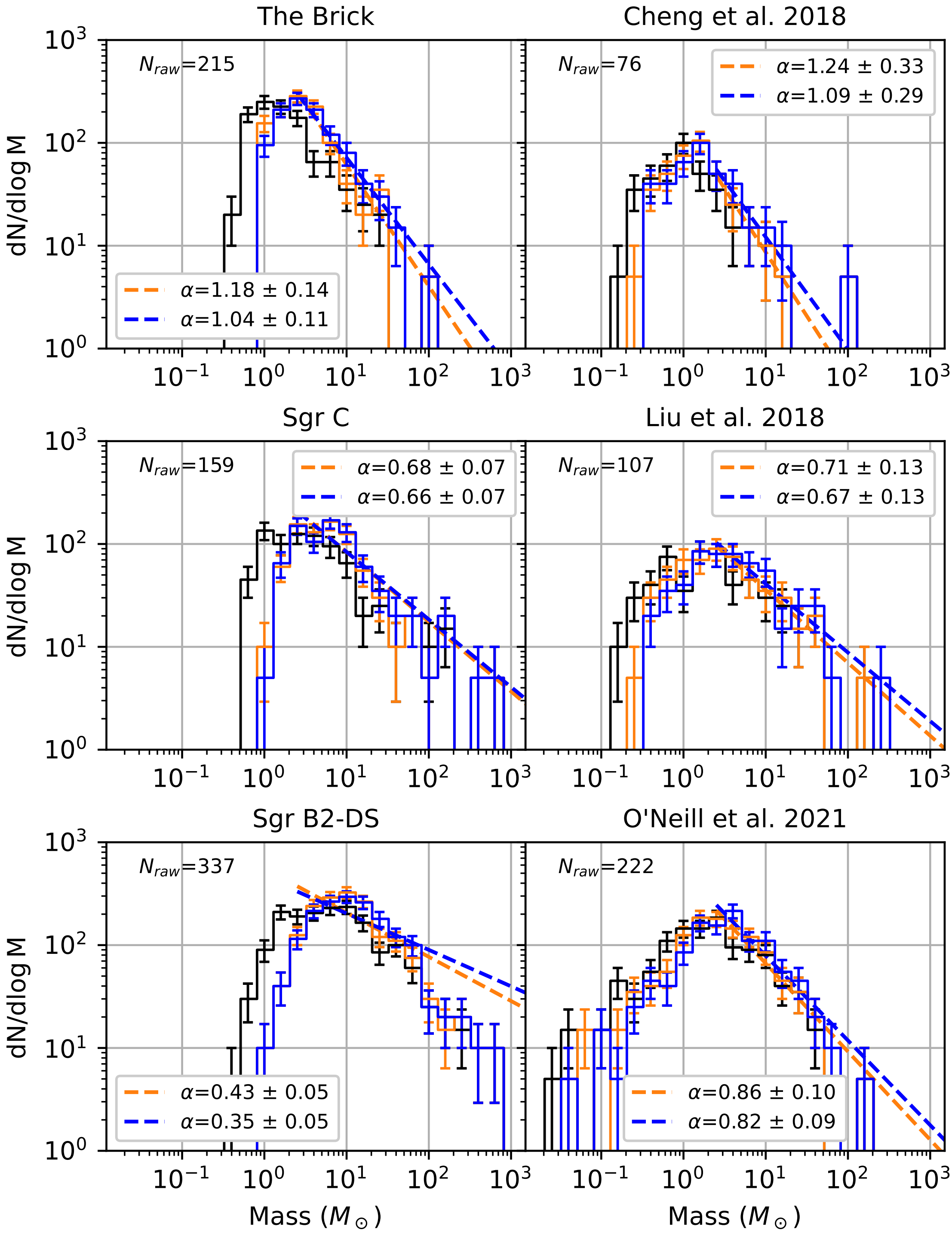

Figure 4.5: Raw and flux-corrected CMFs for the two different methods, The black histogram shows the raw CMF. The orange histogram shows the flux-corrected CMF using the old method (core insertion with beam-sized cores). The blue histogram shows the flux-corrected CMF using the new method described in this work. Power laws are fitted through the WLS method starting from 2 M$_\odot$. Left column: Regions in the CMZ. Right column: Regions studied in Paper I, II and III. From top to bottom: G286.21+0.17, IRDCs and massive protoclusters.

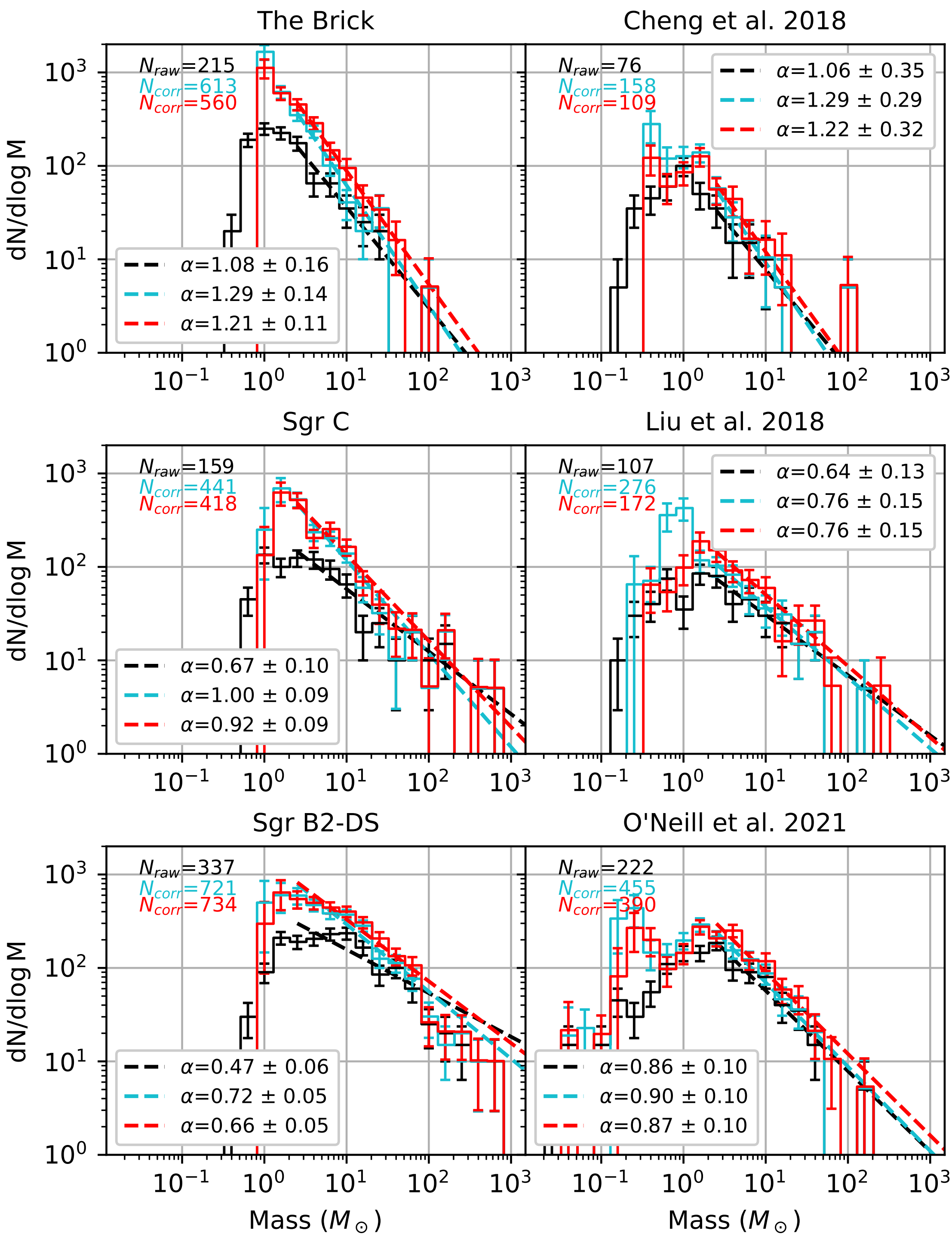

Figure 4.6: Raw and number-corrected CMF with the two different methods. The black histrogram shows the raw CMF. The cyan histogram shows the number-corrected CMF using the old method (core insertion with beam-sized cores). The red histogram is the number-corrected CMF using the new method described in this work. Power laws are fitted through the WLS method starting from 2 $M_\odot$. Left column: Regions in the CMZ. Right column: Regions studied in Paper I, II and III. From top to bottom: G286.21+0.17, IRDCs and massive protoclusters.

shown in the top left and top right panel. This is because the new method generally gives lower flux recovery fractions over the whole mass range, and therefore the corrections have a larger effect. In all the core samples, the new flux-corrected CMF has a shallower slope than the old one.

Differences in the number-corrected CMF are shown in Figure 4.6. Note that the new version of the number-corrected CMF tends to have slightly higher values towards the high mass bins than the old method. The effect is most clearly visible in The Brick (top left), G286.21+0.17 (top right) and the IRDC sample (middle right).The slopes of the number-corrected CMFs are however quite robust under the change of method. As with the flux-corrected CMFs, there is a trend towards shallower CMFs with the new method. However, the change in α is within the 1σ standard error in all cases.

The peak of the CMF may be more influenced by the new method than the slope. As can be seen in the CMFs from Paper II and III (middle and bottom right in Figure 4.6), the large peaks present in the old CMFs becomes significantly smaller with the new method. This is likely because the flux-correction factor for the smallest cores increases with the new method, moving the least massive cores upwards on the mass scale. The low end of the number correction factor is however very modestly affected by the new method, meaning that the smallest cores are moved into a mass range with less number corrections than before.

4.4 Statistical comparison of CMFs

A Kolmogorov-Smirnov (K-S) test was performed to determine if any of the CMFs analyzed in this thesis are similar enough to be sampled from the same underlying distribution, or if the apparent difference between them is statistically significant. The p-values for the different pairs of true CMFs can be seen in Table 4.3. The p-value represents the probability that two sets of samples drawn from the same distribution would be more different than the tested CMFs. If the p-value is 0.05 for example, 95 % of all sample sets drawn from the same distribution would be more similar than the tested sample sets. This means that the tested samples are most likely from different distributions.

To perform a K-S test, individual samples rather than histograms are used. Since the number-corrected CMF is only defined by bin height, a sampling was made. Samples were taken uniformly within each bin, with the number of samples given by the bin height. The samples from two number-corrected CMFs were then compared with the K-S test. The procedure was repeated 3000 times to obtain a reliable average p-value. This is the same procedure used in e.g. Paper II.

In Table 4.3, the p-values obtained from the K-S test can be seen for each pair of CMFs. A low p-value indicates that the samples are likely drawn from different distributions. We choose $p < 0.05$ as the limit of statistical significance. To avoid any influence from different mass sensitivities, only the cores exceeding 2 $M_\odot$ (consistent with the lowest fitting bin) were included.

Table 4.3: p-values of K-S test on number-corrected CMFs, including only cores above 2 $M_\odot$. p-values below 0.05 are marked in red, indicating that the distributions are significantly different.

	Sgr B2-DS	Sgr C	G286	IRDCs	Massive protocl.
The Brick	1.5×10^{-13}	9.0×10^{-3}	0.785	0.049	1.4×10^{-3}
Sgr B2-DS		5.9×10^{-7}	3.6×10^{-3}	9.4×10^{-3}	9.9×10^{-4}
Sgr C			0.395	0.660	0.012
G286				0.383	0.221
IRDCs					0.396

The number-corrected CMFs of the CMZ region are all found to be different from each other. Sgr B2 and the Brick are also significantly different from the CMFs derived in previous papers (with the exception of the Brick and G286, which may have the same underlying distribution). The CMFs of the old regions cannot be distinguished from each other or from Sgr C. However, note that the old regions have rather small numbers of cores above 2 $M_\odot$, which decreases the power of the K-S test. If a lower limit of 0.79 $M_\odot$ is applied instead, almost all the CMFs are significantly different. Only the CMF from Paper II remains potentially similar to Paper III and Sgr C.

4.5 Dense gas fraction

In Table 4.4, total core masses, masses estimated from Bolocam data and dense gas fractions are shown for the three CMZ regions. The Brick has the lowest dense gas fraction, with only 3 % of its mass contained in dense cores. Sgr B2-DS has a dense gas fraction of 14 %, while Sgr C has a value of 24 %. We note that there may be systematic errors in our dense gas fraction values. The core mass and total mass are estimated by different instruments and at different wavelengths. When we compare our Bolocam-derived masses to Herschel-masses from Battersby et al. (2020), we find that their masses for the Brick and Sgr C-Dense are larger by a factor ∼1.5. However, systematic uncertainties should not strongly affect our regions relative to each other. Differences in maximum recoverable scale between the ALMA images could affect how much flux is recovered, but we note that the region with the largest maximum recoverable scale (the Brick), which should recover most flux at the core scale, is also the region with the lowest dense gas fraction. If all regions had the same maximum recoverable scale, the difference between the Brick and the others would only increase.

4.6 Spatial distribution of cores

A Q parameter test was carried out according to the method in Section 3.7.1. The minimum spanning trees can be seen in Figure 4.7. The size of the symbols is proportional to the mass of the cores. Q parameters for each region are found in Table 4.5. All Q parameters are below 0.8, which indicates that the regions are

Table 4.4: Core masses, total masses and dense gas fractions.

Region	Core mass (10^3 M$_\odot$)	Total mass (10^3 M$_\odot$)	Dense gas fraction
The Brick	1.8	54	0.03
Sgr C	4.0	17	0.24
Sgr B2-DS	11	80	0.14

substructured rather than radially distributed. The most strongly substructured region is Sgr B2 with $Q = 0.32$, followed by the Brick with $Q = 0.52$ and Sgr C with $Q = 0.71$. However, the Q parameter is developed for clusters that are approximately circular in projection, and can be biased if the region deviates too strongly from that. The map of Sgr B2 is very elongated, which can explain the low Q value. To decrease this effect, the Q parameter is also calculated for the north end of the Sgr B2-DS map, where the aspect ratio has been limited to 2:1. Note that this region (seen in Figure 4.7, lower left) contains 153 cores, which is close to half of the cores in the original map. The obtained Q value for the limited region is significantly higher, $Q = 0.67$.

Table 4.5: Normalized mean length of MST ($\bar{m}$), normalized mean separation ($\bar{s}$) and Q parameter for the CMZ regions.

Region	$\bar{m}$	$\bar{s}$	Q
The Brick	0.37	0.71	0.52
Sgr B2-DS	0.21	0.63	0.32
Sgr B2-DS, lim.	0.43	0.65	0.67
Sgr C	0.27	0.37	0.71

Furthermore, a mass segregation analysis was carried out for all of the regions. The mass segregation parameter Λ_{MSR} was calculated for every number of sample cores, from two up to all cores in the image (see Section 3.7.2). The result can be seen in Figure 4.8. For the Brick, Λ_{MSR} is close to 1 for all sample sizes. Even though Λ_{MSR} is significantly different from 1 below the scale of 5 M$_\odot$, the size of the difference is small enough to be negligible. Sgr C on the other hand shows elevated values of Λ_{MSR} for high masses, with a value $\sim$ 1.9 for cores above $\sim$ 80 M$_\odot$. The maximum difference from 1 is just below two standard deviations. Sgr B2-DS presents even clearer evidence of mass segregation, with a difference from 1 that is above two standard deviations for a range of masses between 100 and 290 M$_\odot$. In the approximate range 160-290 M$_\odot$(the 5-11 most massive cores) we obtain $\Lambda_{MSR} \sim 1.7 - 2.2$, while the mass range 100-160 M$_\odot$ (the 12-14 most massive cores) shows a lower segregation of $\Lambda_{MSR} \sim 1.3$.

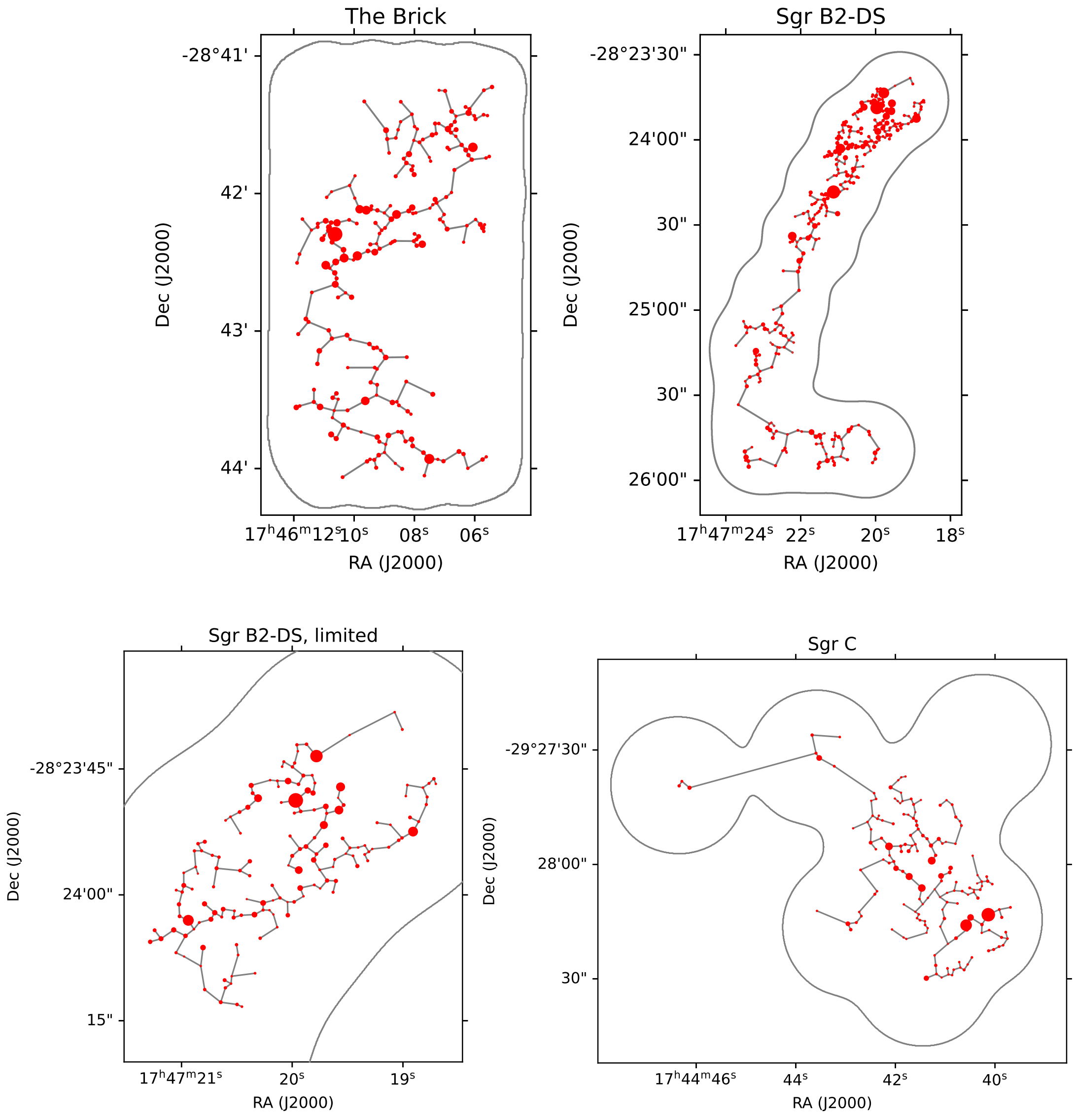

Figure 4.7: Minimum spanning trees for the CMZ regions. The circular symbols represent the cores identified by this work, and their area is proportional to the estimated core mass. Note that the area normalization differs between regions.

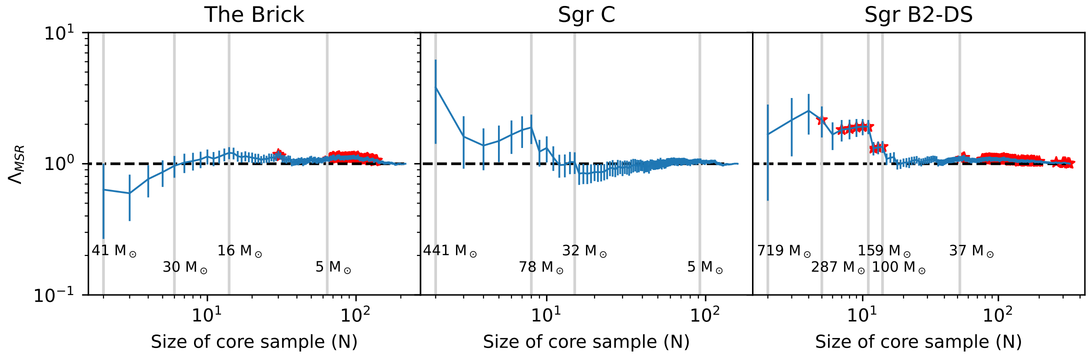

Figure 4.8: Mass segregation parameter Λ_{MSR} as a function of core number N. Red stars mark values that deviate from 1 by more than two standard deviations. While the Brick does not show any notable positive mass segregation, both Sgr C and Sgr B2 show signs of mass segregation for the few most massive cores.

5

Discussion & Conclusions

In this chapter, the results presented in the previous chapter will be discussed. The regions will be compared to each other, potential sources of error will be discussed, as well as the implications of the results for star formation theories. Finally, conclusions will be presented.

5.1 Relation between CMF slope and evolutionary stage

We have calculated the core mass function in three regions in the CMZ, in order to investigate how the CMF varies with environment. The CMFs of the three CMZ regions were found to be significantly different from each other, with the Brick having the steepest slope and Sgr B2 the shallowest. This could be related to the evolutionary stage of the regions. The dense gas fraction in the Brick (0.03) is significantly lower than in Sgr B2-DS (0.14) and Sgr C (0.24), which indicates an earlier evolutionary stage. Since Sgr B2-DS and Sgr C have dense gas fractions of the same order, we cannot say with certainty that one is more evolved than the other. When comparing our dense gas fractions to the values reported in Battersby et al. (2020) (defined as the fraction of mass in 0.1-2 pc scale structures), we find a similar relation between the Brick and Sgr C, which strengthens our conclusion that the Brick is in an earlier evolutionary stage than Sgr C.

Furthermore, the evolutionary stage can be indicated by the star formation rate. The Brick shows few signs of star formation (Immer et al., 2012; Mills et al., 2015), and its star formation rate is estimated to $10^{-4} - 10^{-3}$ $M_\odot$/yr (Lu et al., 2019; Henshaw et al., 2023). Both Sgr B2 and Sgr C have been found to harbor massive star formation (e.g. Ginsburg et al., 2018; Lu et al., 2019). The star formation rate in Sgr B2 has been estimated in the range $\sim 0.04 - 0.08$ $M_\odot$/yr (Kauffmann et al., 2017; Ginsburg et al., 2018), while the star formation rate in Sgr C has been found to be $\sim 0.003 - 0.008$ $M_\odot$/yr (Kauffmann et al., 2017; Lu et al., 2019). Although the global SFR in Sgr B2 is much higher than in Sgr C, Sgr B2 is also much more massive. The SFR per mass is therefore similar for the two clouds. Previous studies have shown shallow core mass functions in high density regions and regions with massive star formation (Kong, 2019; Motte et al., 2018; Pouteau et al., 2022, 2023). Our results are in agreement with that relation.

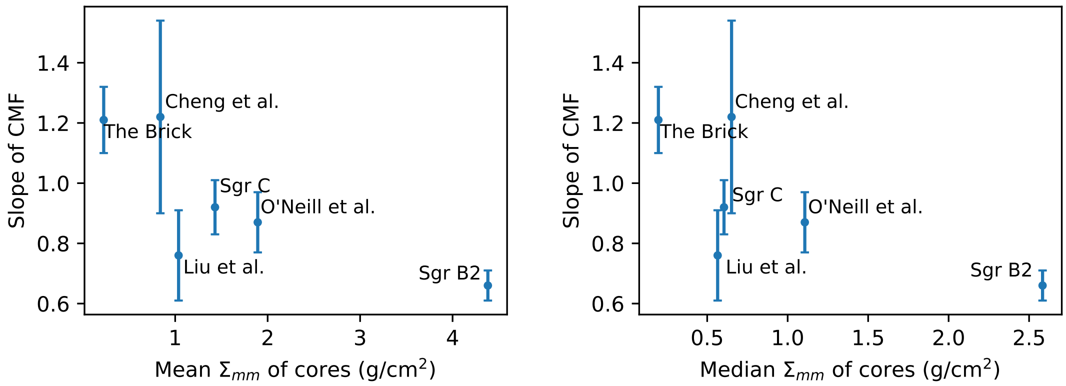

Figure 5.1: Relation between core mass surface density and CMF power law index (WLS fit from 2 $M_\odot$). Left: CMF slope as a function of mean core Σ_{mm}. Right: CMF slope as a function of median core Σ_{mm}.

There are however different ways to interpret such a correlation. One possibility is that the regions that favor massive star formation (for example due to high density) may also favor the development of a top-heavy CMF. The CMF in these regions may never have been Salpeter-like. Another possibility is that the slope of the CMF is directly related to the evolutionary stage of the cores. This view is supported by Nony et al. (2023), who found that prestellar cores in the cloud complex W43 had a steeper CMF than protostellar cores in the same region. The protostellar cores were also more massive in general. This indicates that the CMF slope decreases as the cores of the region evolve. Cores must thus accrete more material during their lifetime, and massive cores need to have a higher accretion rate than low mass cores. However, results from the previous papers in this series compel us to add some nuance to this view. The G286 region is known to be relatively evolved, but still has a CMF slope close to the Salpeter slope. The IRDCs from Paper II on the other hand are in an earlier evolutionary stage, yet present a shallow CMF slope.

Sanhueza et al. (2019) proposed a scenario where the CMF starts out Salpeter-like, to then become shallower due to massive cores accreting gas at a higher rate. Once the most massive cores stop accreting, and fragmentation increases the number of low-mass cores, the CMF evolves towards a Salpeter slope again. This could be one way to explain the relatively steep CMF slope of the G286 protocluster.

In Paper III, a correlation between high mass surface density and shallow CMF slope was discussed. The results from the CMZ seem to follow a similar pattern, if we consider the mass surface density of cores. The region with the lowest core mass surface density (The Brick) has the steepest CMF slope and the highest core mass surface density region (Sgr B2) has the shallowest. In Figure 5.1, the mean and median mass surface density of cores is plotted together with the slope of the CMF for the six core populations studied in this paper series. With the exception of the IRDC sample from Paper II, there is a discernible trend towards shallower CMF slopes in regions with high mass surface density cores.

Both these observations, that the CMF gets shallower due to evolution and high mass surface density, can be explained if the cores accrete gas from the surrounding clump. According to the core accretion model of McKee & Tan (2003), cores are expected to accrete gas from the surroundings with a rate that depends on the clump mass surface density: $\dot{M}_{acc} \propto \Sigma_{cl}^{3/4}$. This would mean that all cores get more massive as they evolve, but the effect is most noticeable in high-density regions. The accretion rate is also expected to be higher for more massive cores. The fact that we do not see any flattening of the CMF in the G286 protocluster can then be explained by the region's low mass surface density compared to the regions studied in this work. The accretion may be too slow to make any difference in the CMF slope in the time it takes for star formation to commence.

5.2 Implications for star formation theories

In order to draw any conclusions about star formation theories, we need to take into account that the IMF of the stars forming in the CMZ may become top-heavy. Top-heavy IMFs have been observed in the Galactic center, e.g. by Lu et al. (2013) in the Nuclear Star Cluster and Hosek et al. (2019) in the Arches cluster in the CMZ. They found slopes of $\alpha = 0.7$ and 0.8 respectively. The top-heavy CMFs in Sgr B2-DS and Sgr C could be consistent with a core accretion model with constant star formation efficiency, as long as the emerging IMF is also top-heavy.

It is difficult to explain how a top-heavy CMF could turn into a canonical IMF. The issue is discussed in (Pouteau et al., 2022), where they propose different shapes of the emerging IMF based on their observed CMF and various fragmentation scenarios and star formation efficiencies. Their CMF has a power law index of 0.95 ± 0.04, which is similar to our Sgr C results with power law index 0.92 ± 0.09 (although derived by a different fitting method). In order to obtain a Salpeter-like IMF through fragmentation, Pouteau et al. (2022) need to assume a number of fragments per core given by $N_{frag}(M) \propto M^{0.4}$. This can be compared to the number of fragments for thermal Jeans fragmentation, which is given by $N_{frag} \propto M$, under the assumption of constant density and temperature in all cores. So in order for Jeans fragmentation to explain the difference between CMF and IMF, the Jeans mass would need to be substantially higher in massive cores. This could be the case if the more massive cores have much higher gas temperatures. Most other scenarios discussed by Pouteau et al. (2022) either lead to an IMF that is even shallower than the CMF, or produce a IMF that is much steeper than the Salpeter slope.

In conclusion, the shallow CMFs observed in Sgr C and Sgr B2 could be consistent with a core accretion scenario as long as the IMF of the region is also top heavy (as some observations indicate). Competitive accretion, where more massive protostars have a higher accretion rate, would on its own make the IMF shallower than the CMF. However, one could imagine a combination of fragmentation and competitive accretion producing a steeper or equal slope of the IMF. This means that we cannot distinguish the different star formation theories based on our CMF results alone.

5.3 Mass segregation and clustering

The mass segregation was found to be different between the three regions. While the Brick lacked any signs of mass segregation, Sgr C showed indications of mass-segregation up to $\Lambda_{MSR} \sim 2$. The mass segregation in Sgr B2-DS is of a similar scale, but more statistically significant. A correlation between mass segregation and evolutionary stage can be seen. This fits in well with the cores accreting gas from the clump, which was discussed in Section 5.1. The cores that are located in the densest parts of the cloud are expected to accrete gas from the clump at a higher rate, causing them to grow more massive. Thus the most massive cores should be localized in the densest region rather than being randomly distributed in the cloud.

It is important to note that the mass segregation of ~ 2, although significant, is low compared to some other regions from the literature. For example, Plunkett et al. (2018) found a mass segregation of ~ 3.7 in the star forming region Serpens South, while Dib & Henning (2019) reported mass segregations of 3.8 an 8.8 in the nearby regions Aquila and Corona Australis, and 3.5 in the W43 complex.

Dib & Henning (2019) found a correlation between the Q parameter and the star formation rate, finding that regions with a higher star formation rate tended to be more centrally concentrated (i.e. higher Q values). This seems to be consistent with our results, since the Brick has a lower Q value than Sgr C, which is known to be forming stars. The northern part of the Sgr B2-DS map has a Q value similar to Sgr C. As mentioned in Section 4.6, the low Q value for the entire Sgr B2-DS map is likely biased due to the shape of the map.

We can also compare our results to Paper III, which calculated Q values for the clumps in their sample with the most detected cores. These clumps were all classified as protostellar, and had Q parameters in the range $0.67 - 0.82$. Furthermore, Moser et al. (2020) calculated the Q value for 35 protostellar cores in an IRDC, obtaining a value of 0.67. These results are similar to our values for Sgr C (0.71) and the limited Sgr B2 map (0.67), but higher than the Brick value (0.52). Wu et al. (2017) performed simulations of star cluster formation, with and without cloud collision. In the non-colliding case, they found that Q quickly stabilized at very low values (~ 0.2). Our results are more consistent with the colliding case, for which the Q value stabilizes at ~ 0.6. However, the simulations by Wu et al. (2017) do not support a monotonic increase of Q with evolutionary stage. In the colliding case, Q first grows towards a peak above 0.8, to then drop to ~ 0.3 before growing towards ~ 0.6 again. Note that these simulations are simplified and do not include feedback from the forming stars. Nevertheless, they indicate that the relationship between Q and evolutionary stage could be complex.

When interpreting the mass segregation and Q parameter for Sgr B2-DS, it is important to keep in mind that the ALMA image shows the outskirts of a larger cloud complex, Sgr B2. It might not be directly comparable to the Brick and Sgr C, where the ALMA map shows the main cloud. The results should therefore be treated with caution.

5.4 Caveats

There are a few caveats with the results that one needs to be aware of. Firstly, variations in core temperature may cause systematic errors in the mass estimation. As mentioned in Section 3.3, cores that are warmer than we assume will have their masses overestimated. It is highly possible that the most massive cores in Sgr B2 and Sgr C are protostellar, and thus have higher dust temperatures than the less massive, prestellar cores. This would lead to an overestimation of the masses of the most massive cores specifically, causing the core mass function we derive to be biased towards shallower slopes. Recently, Jeff et al. (2024) identified nine hot cores in Sgr B2-DS, and estimated gas temperatures in them between 200 and 400 K. The positions of the hot cores all match with cores that are among the 20 most massive in our sample. Jeff et al. (2024) argue that their cores are dense enough for the gas and dust to be coupled. If this is the case, it could significantly affect the masses of the most massive cores in our Sgr B2-DS CMF. To make sure that the difference in CMF between the regions is not heavily influenced by temperature differences, high-resolution temperature estimates of the CMZ are needed.

Another notable caveat is that the resolution of our ALMA data is limited, with the beam corresponding to a physical scale of $\sim 0.02 - 0.04$ pc depending on the region. It is likely that the larger cores, with diameters of a few beams, would appear fragmented if imaged with higher resolution. The effect of resolution on the CMF was investigated in Paper I, where a lower resolution was found to give a slightly shallower true CMF.

5.5 Completeness correction

The method developed in this thesis aimed to derive more accurate flux and number recovery fractions than the method of Paper I-III. They inserted synthetic cores the size of the beam, for all core masses. This is a valid approximation only for small, unresolved cores, although a significant part of the core sample consists of cores that extend over several beams. Approximating these as beam-sized without altering the mass, results in synthetic cores that have much higher peak intensities, which make them easier to detect than their observed counterparts.

To make the radius of the inserted cores realistic, a mass-radius relation needed to be derived. In this thesis, a power law fit was chosen. In principle, another functional form could have been used. The choice of a power law was guided by the distribution of radii and masses of the observed regions. In particular, the cores of the Brick could be seen to be well described by a power law (see Figure 3.3). A power law is also the expected form of the mass radius relation if all cores have similar density (in that case $M \propto r^3$, so $r \propto M^{1/3}$). All the CMZ regions can be seen in Figure 3.3 to be reasonably well-described by a power law. However, the Sgr B2 and Sgr C cores started to deviate from the power law form after a few iterations. An example can be seen in Figure B.1, Appendix B. This highlights that a power law is an imperfect description of the core sample, since the radial scatter for a given mass is large for some of the regions.

One could try to create a mass-radius relation without assuming any explicit functional form. Such an approach was investigated early during the thesis work. The radius of the inserted cores of mass M was determined by the median radius of observed cores within a logarithmic mass bin around M (with the same binning scheme as for the construction of the CMF). However, this approach lead to problems. In the higher mass bins, the number of cores is typically low. Combined with a large radius scatter, this could make the median radius very different in adjacent mass bins. If the radius increases too steeply from one bin to the next, the inserted cores with higher mass may actually have a smaller peak intensity. This leads to more massive cores being more difficult to detect, and unphysical "spikes" being present in the recovery curves. An example can be seen in Figure B.2, Appendix B. This approach was therefore abandoned.

Using the new completeness correction method instead of the old one had a modest impact on the CMF slope. In relation to this, it is worth to note the increased computational complexity of the method. The computation time scales with the number of iterations, making the core insertion and recovery $\sim$ 20 times slower than the method from Paper I-III. The computation time of the core insertion code is mainly determined by the dendrogram algorithm. For the typical situation in this thesis, 20 iterations were performed, 25 masses were tested and 100 insertion experiments were performed at each mass. This gives a total of 50 000 runs of the dendrogram algorithm. The computational complexity of dendrogram scales linearly with the number of analyzed pixels. For large mosaics with many pixels, speed may need to be prioritized. In future studies, the modest change in results therefore needs to be weighed against the increased complexity of the correction computation.

5.6 Conclusions

We have measured the core mass function in three different clouds in the Central Molecular Zone, a region known to harbor extreme physical conditions compared to the local interstellar medium. The Brick is mostly quiescent, while Sgr C and Sgr B2 are active star formation sites. A total of 711 cores were identified using the dendrogram algorithm in ALMA band 6 continuum images.

Flux correction and number correction was performed on the core samples, using a new method that takes core size into account. We also used this method to reanalyze the core samples from Paper I, II and III. The new correction method increased the number of high-mass cores compared to the previous method, but the difference in the derived slope was small.

We fitted power laws to the CMFs above 2 $M_\odot$, using both a weighted least squares fit and a maximum likelihood estimator. Since the difference in the fits is small, we report the WLS parameters as our final results. For the Brick, a slope of 1.21 ± 0.11 was found above 2 $M_\odot$, consistent with the Salpeter slope. The CMFs of Sgr C and Sgr B2 were found to be top-heavy, with slopes of 0.92 ± 0.09 and 0.66 ± 0.05 respectively. The three CMZ regions were all significantly different from each other.

Furthermore, we analyzed the spatial distribution of cores by calculating the Q parameter and the mass segregation parameter Λ_{MSR}. The Q parameter was notably smaller for the Brick ($Q = 0.52$) than the other two regions ($Q = 0.71$ for Sgr C and $Q = 0.67$ for the densest part of Sgr B2-DS). The values indicate that all the regions are substructured rather than radially distributed, but that the Brick has the highest degree of substructure. The Brick showed no evidence for mass segregation. Sgr C showed a mass segregation of ~ 2 for the 8 most massive cores, but the difference from 1 was less than two standard deviations. Sgr B2-DS was seen to be significantly mass segregated at a level of $\Lambda_{MSR} \sim 2$ for the 5-11 most massive cores, and a lower Λ_{MSR} value for the 12-14 most massive cores. The values of Λ_{MSR} suggest that the mass segregation is related to the evolutionary stage of the cores.

We find that our results, both the CMFs and the mass segregation parameters, are consistent with a model in which cores grow over time through accretion from the surrounding clump. When it comes to star formation scenarios, neither core accretion nor competitive accretion can be ruled out based on our results. However, core accretion would likely lead to a top-heavy IMF in Sgr C and Sgr B2. Such an IMF has indeed been observed in other parts of the Galactic center.

Our results join the growing body of evidence against the universality of the CMF, by demonstrating that the CMFs in the three studied regions are different above 2 $M_\odot$. However, the constant temperature assumption is a significant source of error. In order to confirm these results, high-resolution temperature estimates of the CMZ are needed for future studies. Furthermore, the regions need to be studied in higher resolution in order to fully constrain the CMF. This work has focused on determining the high-mass power law index, but with sufficient resolution, the CMF peak could also be located.

Bibliography

Allison, R. J., Goodwin, S. P., Parker, R. J., et al. 2009, MNRAS, 395, 1449, doi: 10.1111/j.1365-2966.2009.14508.x

André, P., Men'shchikov, A., Bontemps, S., et al. 2010, A&A, 518, L102, doi: 10.1051/0004-6361/201014666

Battersby, C., Keto, E., Walker, D., et al. 2020, ApJS, 249, 35, doi: 10.3847/1538-4365/aba18e

Beardwood, J., Halton, J. H., & Hammersley, J. M. 1959, Mathematical Proceedings of the Cambridge Philosophical Society, 55, 299

Bonnell, I. A., Bate, M. R., Clarke, C. J., & Pringle, J. E. 1997, MNRAS, 285, 201, doi: 10.1093/mnras/285.1.201

—. 2001, MNRAS, 323, 785, doi: 10.1046/j.1365-8711.2001.04270.x

Cartwright, A., & Whitworth, A. P. 2004, MNRAS, 348, 589, doi: 10.1111/j.1365-2966.2004.07360.x

Cheng, C. M., Villaume, A., Balogh, M. L., et al. 2023, MNRAS, 526, 4004, doi: 10.1093/mnras/stad2967

Cheng, Y., Tan, J. C., Liu, M., et al. 2018, ApJ, 853, 160, doi: 10.3847/1538-4357/aaa3f1

Choudhuri, A. R. 2010, Astrophysics for Physicists (Cambridge University Press)

Clark, R. M., Cox, S. J. D., & Laslett, G. M. 1999, GeoJI, 136, 357, doi: 10.1046/j.1365-246X.1999.00728.x

Clauset, A., Shalizi, C. R., & Newman, M. E. 2009, SIAM review, 51, 661

Condon, J. J., & Ransom, S. M. 2016, Essential radio astronomy, Vol. 2 (Princeton University Press)

Cortes, P. C., Vlahakis, C., Hales, A., et al. 2023, ALMA Technical Handbook (ALMA Doc. 10.3, ver. 1.0), doi: https://doi.org/10.5281/zenodo.4511521

Dib, S., & Henning, T. 2019, A&A, 629, A135, doi: 10.1051/0004-6361/201834080

Draine, B. T. 2011, Physics of the Interstellar and Intergalactic Medium (Princeton University Press)

Federrath, C., Rathborne, J. M., Longmore, S. N., et al. 2016, ApJ, 832, 143, doi: 10.3847/0004-637X/832/2/143

Ferreras, I., La Barbera, F., de La Rosa, I. G., et al. 2013, MNRAS, 429, L15, doi: 10.1093/mnrasl/sls014

Ginsburg, A., Glenn, J., Rosolowsky, E., et al. 2013, ApJS, 208, 14, doi: 10.1088/0067-0049/208/2/14

Ginsburg, A., Henkel, C., Ao, Y., et al. 2016, A&A, 586, A50, doi: 10.1051/0004-6361/201526100

Ginsburg, A., Bally, J., Barnes, A., et al. 2018, ApJ, 853, 171, doi: 10.3847/1538-4357/aaa6d4

Girichidis, P., Offner, S. S. R., Kritsuk, A. G., et al. 2020, Space Sci. Rev., 216, 68, doi: 10.1007/s11214-020-00693-8

GRAVITY Collaboration, Abuter, R., Aimar, N., et al. 2022, A&A, 657, L12, doi: 10.1051/0004-6361/202142465

Hennebelle, P., & Chabrier, G. 2008, ApJ, 684, 395, doi: 10.1086/589916

Hennebelle, P., & Falgarone, E. 2012, A&A Rev., 20, 55, doi: 10.1007/s00159-012-0055-y

Henshaw, J. D., Barnes, A. T., Battersby, C., et al. 2023, in Astronomical Society of the Pacific Conference Series, Vol. 534, Protostars and Planets VII, ed. S. Inutsuka, Y. Aikawa, T. Muto, K. Tomida, & M. Tamura, 83, doi: 10.48550/arXiv.2203.11223

Högbom, J. A. 1974, A&AS, 15, 417

Hopkins, A. M. 2018, PASA, 35, e039, doi: 10.1017/pasa.2018.29

Hopkins, P. F. 2012, MNRAS, 423, 2037, doi: 10.1111/j.1365-2966.2012.20731.x

Hosek, Matthew W., J., Lu, J. R., Anderson, J., et al. 2019, ApJ, 870, 44, doi: 10.3847/1538-4357/aaef90

Immer, K., Menten, K. M., Schuller, F., & Lis, D. C. 2012, A&A, 548, A120, doi: 10.1051/0004-6361/201219182

Jeans, J. 1929, Astronomy and cosmogony (CUP Archive)

Jeff, D., Ginsburg, A., Bulatek, A., et al. 2024, arXiv e-prints, arXiv:2401.09749, doi: 10.48550/arXiv.2401.09749

Kahn, F. D. 1974, A&A, 37, 149

Kauffmann, J., Pillai, T., Zhang, Q., et al. 2017, A&A, 603, A89, doi: 10.1051/0004-6361/201628088

Kong, S. 2019, ApJ, 873, 31, doi: 10.3847/1538-4357/aaffd5

Könyves, V., André, P., Men'shchikov, A., et al. 2015, A&A, 584, A91, doi: 10.1051/0004-6361/201525861

Kroupa, P. 2001, MNRAS, 322, 231, doi: 10.1046/j.1365-8711.2001.04022.x

Kruijssen, J. M. D., & Longmore, S. N. 2013, MNRAS, 435, 2598, doi: 10.1093/mnras/stt1634

Krumholz, M. R. 2015, Notes on Star Formation (arXiv e-prints), arXiv:1511.03457, doi: 10.48550/arXiv.1511.03457

Krumholz, M. R., & McKee, C. F. 2008, Nature, 451, 1082, doi: 10.1038/nature06620

Krumholz, M. R., McKee, C. F., & Klein, R. I. 2005, ApJ, 618, L33, doi: 10.1086/427555

Lada, C. J., Lombardi, M., & Alves, J. F. 2010, ApJ, 724, 687, doi: 10.1088/0004-637X/724/1/687

Lis, D. C., Menten, K. M., Serabyn, E., & Zylka, R. 1994, ApJ, 423, L39, doi: 10.1086/187230

Liu, M., Tan, J. C., Cheng, Y., & Kong, S. 2018, ApJ, 862, 105, doi: 10.3847/1538-4357/aacb7c

Longmore, S. N., Rathborne, J., Bastian, N., et al. 2012, ApJ, 746, 117, doi: 10.1088/0004-637X/746/2/117

Longmore, S. N., Bally, J., Testi, L., et al. 2013, MNRAS, 429, 987, doi: 10.1093/mnras/sts376

Lu, J. R., Do, T., Ghez, A. M., et al. 2013, ApJ, 764, 155, doi: 10.1088/0004-637X/764/2/155

Lu, X., Cheng, Y., Ginsburg, A., et al. 2020, ApJ, 894, L14, doi: 10.3847/2041-8213/ab8b65

Lu, X., Zhang, Q., Kauffmann, J., et al. 2019, ApJ, 872, 171, doi: 10.3847/1538-4357/ab017d

McKee, C. F., & Ostriker, E. C. 2007, ARA&A, 45, 565, doi: 10.1146/annurev.astro.45.051806.110602

McKee, C. F., & Tan, J. C. 2003, ApJ, 585, 850, doi: 10.1086/346149

Miller, G. E., & Scalo, J. M. 1979, ApJS, 41, 513, doi: 10.1086/190629

Mills, E. A. C., Butterfield, N., Ludovici, D. A., et al. 2015, ApJ, 805, 72, doi: 10.1088/0004-637X/805/1/72

Moser, E., Liu, M., Tan, J. C., et al. 2020, ApJ, 897, 136, doi: 10.3847/1538-4357/ab96c1

Motte, F., Andre, P., & Neri, R. 1998, A&A, 336, 150

Motte, F., Nony, T., Louvet, F., et al. 2018, Nature Astronomy, 2, 478, doi: 10.1038/s41550-018-0452-x

Nony, T., Galván-Madrid, R., Motte, F., et al. 2023, A&A, 674, A75, doi: 10.1051/0004-6361/202244762

Offner, S. S. R., Clark, P. C., Hennebelle, P., et al. 2014, in Protostars and Planets VI, ed. H. Beuther, R. S. Klessen, C. P. Dullemond, & T. Henning, 53–75, doi: 10.2458/azu_uapress_9780816531240-ch003

Ohashi, S., Sanhueza, P., Chen, H.-R. V., et al. 2016, ApJ, 833, 209, doi: 10.3847/1538-4357/833/2/209

O'Neill, T. J., Cosentino, G., Tan, J. C., Cheng, Y., & Liu, M. 2021, ApJ, 916, 45, doi: 10.3847/1538-4357/ac062d

Ossenkopf, V., & Henning, T. 1994, A&A, 291, 943

Padoan, P., & Nordlund, Å. 2002, ApJ, 576, 870, doi: 10.1086/341790

Padoan, P., Nordlund, A., & Jones, B. J. T. 1997, MNRAS, 288, 145, doi: 10.1093/mnras/288.1.145

Pelkonen, V. M., Padoan, P., Haugbølle, T., & Nordlund, Å. 2021, MNRAS, 504, 1219, doi: 10.1093/mnras/stab844

Plunkett, A. L., Fernández-López, M., Arce, H. G., et al. 2018, A&A, 615, A9, doi: 10.1051/0004-6361/201732372

Pouteau, Y., Motte, F., Nony, T., et al. 2022, A&A, 664, A26, doi: 10.1051/0004-6361/202142951

—. 2023, A&A, 674, A76, doi: 10.1051/0004-6361/202244776

Rosen, A. L., & Krumholz, M. R. 2020, AJ, 160, 78, doi: 10.3847/1538-3881/ab9abf

Rosolowsky, E. W., Pineda, J. E., Kauffmann, J., & Goodman, A. A. 2008, ApJ, 679, 1338, doi: 10.1086/587685

Salpeter, E. E. 1955, ApJ, 121, 161, doi: 10.1086/145971

Sanhueza, P., Contreras, Y., Wu, B., et al. 2019, ApJ, 886, 102, doi: 10.3847/1538-4357/ab45e9

Santa-Maria, M. G., Goicoechea, J. R., Etxaluze, M., Cernicharo, J., & Cuadrado, S. 2021, A&A, 649, A32, doi: 10.1051/0004-6361/202040221

Schmiedeke, A., Schilke, P., Möller, T., et al. 2016, A&A, 588, A143, doi: 10.1051/0004-6361/201527311

Schneider, F. R. N., Sana, H., Evans, C. J., et al. 2018, Science, 359, 69, doi: 10.1126/science.aan0106

Shu, F. H., Adams, F. C., & Lizano, S. 1987, ARA&A, 25, 23, doi: 10.1146/annurev.aa.25.090187.000323

Tan, J. C., Beltrán, M. T., Caselli, P., et al. 2014, in Protostars and Planets VI, ed. H. Beuther, R. S. Klessen, C. P. Dullemond, & T. Henning, 149–172, doi: 10.2458/azu_uapress_9780816531240-ch007

Tan, J. C., Kong, S., Butler, M. J., Caselli, P., & Fontani, F. 2013, ApJ, 779, 96, doi: 10.1088/0004-637X/779/2/96

Testi, L., & Sargent, A. I. 1998, ApJ, 508, L91, doi: 10.1086/311724

van Dokkum, P., Conroy, C., Villaume, A., Brodie, J., & Romanowsky, A. J. 2017, ApJ, 841, 68, doi: 10.3847/1538-4357/aa7135

Virkar, Y., & Clauset, A. 2014, The Annals of Applied Statistics, 8, 89–119

Walker, D. L., Longmore, S. N., Bally, J., et al. 2021, MNRAS, 503, 77, doi: 10.1093/mnras/stab415

White, E. P., Enquist, B. J., & Green, J. L. 2008, Ecology, 89, 905, doi: 10.1890/07-1288.1

Williams, B. A., Walker, D. L., Longmore, S. N., et al. 2022, MNRAS, 514, 578, doi: 10.1093/mnras/stac1378

Wilson, T. L., Rohlfs, K., & Hüttemeister, S. 2013, Tools of radio astronomy (Springer Science & Business Media)

Wolfire, M. G., & Cassinelli, J. P. 1987, ApJ, 319, 850, doi: 10.1086/165503

Wu, B., Tan, J. C., Christie, D., et al. 2017, ApJ, 841, 88, doi: 10.3847/1538-4357/aa6ffa

Zhang, Y., & Tan, J. C. 2015, ApJ, 802, L15, doi: 10.1088/2041-8205/802/2/L15

A

Technical details of ALMA data

The Brick (ALMA ID: 2012.1.00133.S, PI: G. Garay) was observed by 32 antennas in Cycle 1, with baselines in the range 15-360 m. Four spectral windows with bandwidth 1.875 GHz and center frequencies 251.521, 250.221, 265.523 and 267.580 GHz were used. The resulting continuum image has a center frequency of 258 GHz, corresponding to a wavelength of 1.16 mm. Calibration was done with the sources J1924-2914, J2230-1325, J1744-3116 and Neptune. The mosaic consists of 140 pointings.

Sgr B2-DS (ALMA ID: 2017.1.00114.S, PI: A. Ginsburg) was observed by 43 antennas in Cycle 5, with baselines in the range 15-783 m. Four spectral windows with bandwidth 1.875 GHz and center frequencies 217.366, 219.199, 231.308 and 233.183 GHz were used. The resulting continuum image has a center frequency of 225 GHz, corresponding to a wavelength of 1.33 mm. Calibration was done with the sources J1924-2914 and J1744-3116. The mosaic consists of 11 pointings.

Finally, Sgr C (ALMA ID: 2016.1.00243.S, PI: Q. Zhang) was observed by 39 antennas in Cycle 4, with baselines in the range 15-460 m. Four spectral windows with bandwidth 1.875 GHz and center frequencies 217.915, 219.998, 232.110 and 234.110 GHz were used. The resulting continuum image has a center frequency of 226 GHz, corresponding to a wavelength of 1.33 mm. Calibration was done with the sources J1924-2914, J1742-1517 and J1744-3116. The mosaic consists of 9 pointings.

Continuum images from the ALMA archive were used directly, without reimaging. The synthesized FWHM beam sizes of the images are $1.03'' \times 0.855''$(Position angle=78°) for the Brick, $0.46'' \times 0.37''$(PA=−86°) for Sgr B2 and $0.80'' \times 0.60''$(PA=84°) for Sgr C. Maximum recoverable scales are $10.62''$, $6.48''$ and $6.38''$ for the Brick, Sgr B2 and Sgr C respectively.

B

Supplementary figures

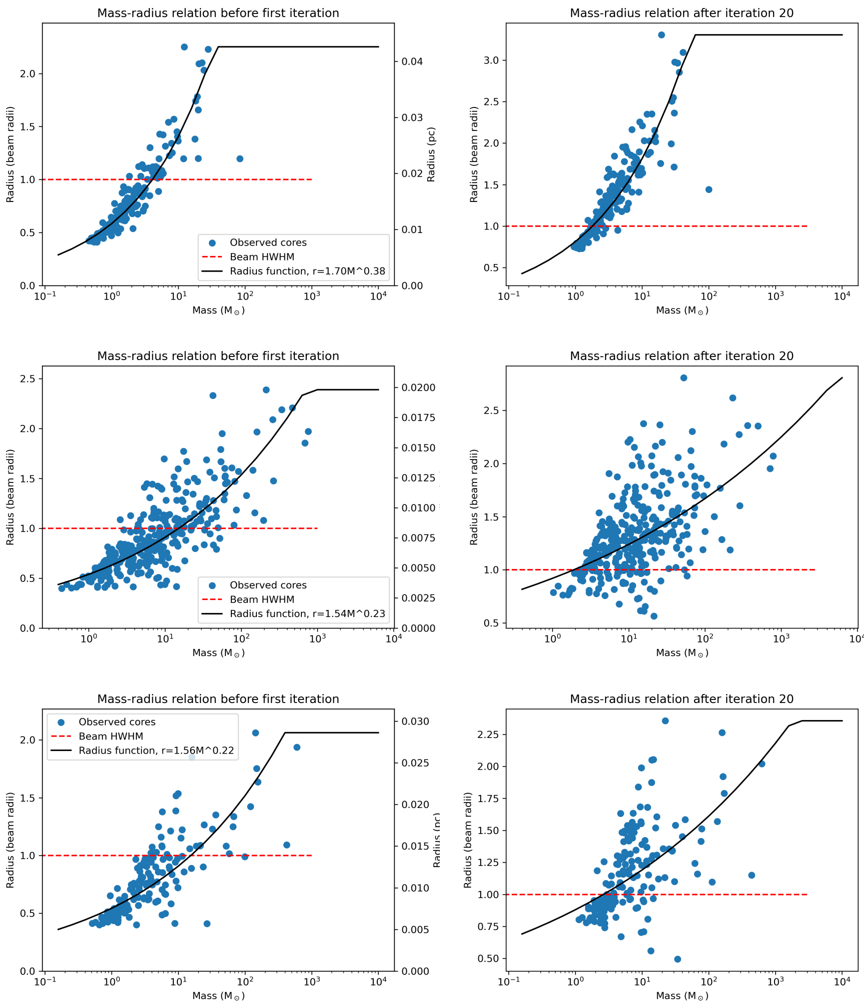

Figure B.1: Mass-radius relations before and after iterations. Top row: The Brick, middle row: Sgr B2, bottom row: Sgr C.

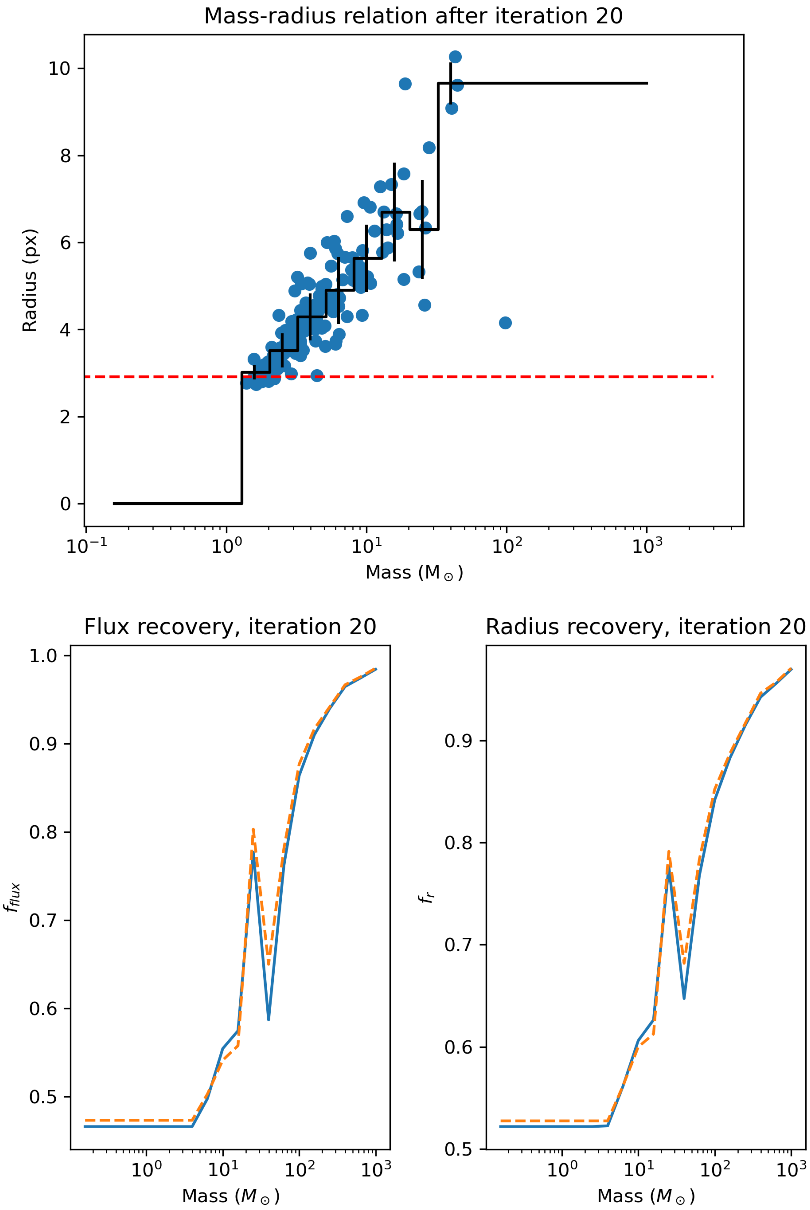

Figure B.2: Illustration of the shortcomings of the first tested mass-radius relation, made by calculating the median radius in each bin instead of fitting a function. The example shows the Brick. Top: core masses (x axis) and radii (y axis) after 20 iterations. Bottom: Flux recovery fraction (left panel) and radius recovery fraction (right panel) as a function of mass after 20 iterations. The large radius increase between 25 M$_\odot$ and 39 M$_\odot$(top) causes an abrupt decrease in the flux and radius recovery fraction (bottom).

C

Core properties

Below follows the properties of each core detected in the Brick, Sgr B2-DS and Sgr C.

Table C.1: Cores in the Brick. Galactic coordinates for the center position of the core (calculated by astrodendro) are given. Note that the radius R_c is the radius of a circle with the same total area as the core, while σ_{dendro} is the astrodendro radius (as described in Section 3.4.1).

ID	l (°)	b (°)	$I_{\nu,peak}$ (mJy/beam)	F_ν (mJy)	M_{raw} ($M_\odot$)	M_{corr} ($M_\odot$)	R_c (0.01 pc)	σ_{dendro} (0.01 pc)	Σ (g cm^{-2})
1	0.260970	0.016159	40.20	60.09	83.79	100.01	5.29	1.92	1.99
2	0.231768	0.011749	3.79	20.16	28.11	41.16	7.86	3.58	0.30
3	0.261278	0.035903	3.79	17.35	24.18	35.96	6.98	3.27	0.33
4	0.257326	0.017097	2.79	16.26	22.67	33.97	6.93	3.38	0.31
5	0.257932	0.015596	2.64	14.66	20.43	30.98	6.96	3.36	0.28
6	0.259142	0.023763	4.29	14.30	19.94	30.32	5.27	2.66	0.48
7	0.261493	0.020899	9.00	14.21	19.81	30.15	4.63	1.93	0.61
8	0.258349	0.013246	3.73	13.84	19.30	29.46	6.16	2.86	0.34
9	0.241813	0.008779	4.04	13.06	18.21	27.99	5.87	2.80	0.35
10	0.262007	0.020272	5.06	12.68	17.68	27.27	4.83	2.22	0.50
11	0.254438	0.024555	2.07	8.83	12.32	19.55	6.17	3.62	0.22
12	0.262032	0.017078	5.25	8.56	11.93	18.97	4.45	1.92	0.40
13	0.255773	0.013019	2.80	7.10	9.89	15.93	4.77	2.19	0.29
14	0.258057	0.014474	2.64	6.97	9.72	15.67	4.73	2.26	0.29
15	0.256611	0.019143	2.19	6.86	9.57	15.45	4.76	2.33	0.28
16	0.244036	0.003723	2.02	6.15	8.58	14.03	4.98	2.52	0.23
17	0.264737	0.034477	2.36	5.80	8.09	13.32	4.17	2.01	0.31
18	0.258870	0.025824	2.22	5.66	7.89	13.04	4.39	2.15	0.27
19	0.265115	0.037631	2.46	5.28	7.36	12.25	4.13	1.97	0.29
20	0.264601	0.028862	1.91	5.07	7.07	11.84	4.60	2.47	0.22
21	0.240493	0.003134	1.89	4.57	6.37	10.80	4.32	2.11	0.23
22	0.262080	0.015967	2.58	4.27	5.95	10.17	3.32	1.70	0.36
23	0.268523	0.027993	1.76	4.23	5.89	10.08	4.45	2.29	0.20
24	0.262948	0.016035	2.36	4.05	5.64	9.73	3.72	1.74	0.27

Continued on next page

Table C.1 (continued)

ID	l (°)	b (°)	$I_{\nu,peak}$ (mJy/beam)	F_ν (mJy)	M_{raw} ($M_\odot$)	M_{corr} ($M_\odot$)	R_c (0.01 pc)	σ_{dendro} (0.01 pc)	Σ (g cm^{-2})
25	0.261258	0.014538	2.51	3.91	5.45	9.46	3.53	1.66	0.29
26	0.234919	0.011150	1.74	3.77	5.25	9.19	4.22	2.30	0.20
27	0.249889	0.007175	1.96	3.69	5.14	9.04	3.89	1.92	0.23
28	0.236783	0.008996	2.30	3.64	5.08	8.95	3.68	1.70	0.25
29	0.258830	0.016056	2.28	3.64	5.07	8.94	3.70	1.72	0.25
30	0.258978	0.022930	2.75	3.63	5.06	8.92	2.88	1.43	0.40
31	0.245485	0.001226	2.29	3.51	4.89	8.69	3.47	1.63	0.27
32	0.245023	0.013633	1.88	3.47	4.84	8.62	3.70	1.78	0.24
33	0.237305	0.007737	1.78	3.33	4.64	8.34	3.62	1.72	0.23
34	0.239938	0.011491	1.93	3.27	4.55	8.22	3.70	1.80	0.22
35	0.256989	0.013691	2.29	3.04	4.23	7.77	3.43	1.65	0.24
36	0.253408	0.013897	1.61	2.96	4.13	7.62	3.70	1.80	0.20
37	0.252323	0.031836	1.58	2.93	4.09	7.56	3.53	1.72	0.22
38	0.240691	0.004983	1.30	2.68	3.74	7.06	3.64	2.09	0.19
39	0.258262	0.028710	2.28	2.68	3.74	7.05	2.74	1.36	0.33
40	0.239740	0.003396	1.43	2.57	3.58	6.83	3.45	1.78	0.20
41	0.262160	0.028104	1.49	2.45	3.42	6.59	3.17	1.61	0.23
42	0.265128	0.032472	1.69	2.30	3.20	6.26	3.02	1.47	0.23
43	0.261447	0.034999	2.91	2.28	3.19	6.23	2.64	1.21	0.30
44	0.238239	0.016185	1.48	2.22	3.09	6.07	3.29	1.77	0.19
45	0.254441	0.028080	1.87	2.22	3.09	6.07	2.95	1.39	0.24
46	0.264166	0.035278	1.70	2.21	3.08	6.04	3.00	1.48	0.23
47	0.252828	0.031811	1.56	2.18	3.04	5.98	3.04	1.48	0.22
48	0.260331	0.015347	2.98	2.14	2.99	5.89	2.59	1.15	0.30
49	0.261769	0.015719	2.54	2.13	2.97	5.86	2.32	1.13	0.37
50	0.249764	0.011032	1.23	2.12	2.96	5.84	3.32	1.80	0.18
51	0.230669	0.015288	1.57	2.05	2.86	5.67	3.13	1.83	0.19
52	0.258736	0.025243	1.72	2.05	2.86	5.66	2.76	1.35	0.25
53	0.234168	0.010837	1.69	2.05	2.86	5.66	3.02	1.46	0.21
54	0.254036	0.007799	1.49	1.96	2.73	5.44	2.93	1.66	0.21
55	0.255463	0.024677	1.57	1.95	2.72	5.42	2.79	1.42	0.23
56	0.257166	0.018506	1.75	1.90	2.66	5.31	2.67	1.42	0.25
57	0.266347	0.035964	1.67	1.88	2.62	5.25	2.86	1.39	0.21
58	0.262799	0.028148	1.43	1.82	2.54	5.10	2.84	1.81	0.21
59	0.235350	0.006751	1.21	1.77	2.47	4.97	2.97	1.51	0.19
60	0.260646	0.015564	2.45	1.75	2.45	4.94	2.34	1.08	0.30
61	0.262416	0.016485	2.13	1.75	2.44	4.93	2.32	1.22	0.30
62	0.232786	0.011536	1.37	1.74	2.43	4.91	2.95	1.50	0.19
63	0.236294	0.010568	1.60	1.68	2.35	4.76	2.72	1.39	0.21
64	0.261309	0.021426	1.88	1.65	2.30	4.68	2.40	1.20	0.27
65	0.244193	0.005606	1.25	1.65	2.30	4.67	2.86	1.48	0.19
66	0.244406	0.006264	1.34	1.65	2.29	4.67	2.84	1.46	0.19
67	0.247439	0.012795	1.51	1.60	2.22	4.54	2.74	1.41	0.20
68	0.263850	0.028035	1.78	1.57	2.19	4.49	2.54	1.20	0.23
69	0.248665	0.006158	1.49	1.55	2.16	4.43	2.67	1.31	0.20

Continued on next page

Table C.1 (continued)

ID	l (°)	b (°)	$I_{\nu,peak}$ (mJy/beam)	F_ν (mJy)	M_{raw} ($M_\odot$)	M_{corr} ($M_\odot$)	R_c (0.01 pc)	σ_{dendro} (0.01 pc)	Σ (g cm^{-2})
70	0.238062	0.012512	1.26	1.54	2.15	4.42	2.84	1.39	0.18
71	0.260533	0.016584	3.03	1.50	2.09	4.30	1.79	0.86	0.43
72	0.228353	0.017226	1.58	1.49	2.08	4.28	2.54	1.24	0.21
73	0.260776	0.022043	1.89	1.48	2.07	4.26	2.37	1.23	0.24
74	0.264935	0.035025	1.54	1.46	2.04	4.21	2.37	1.17	0.24
75	0.246750	0.012981	1.85	1.46	2.04	4.21	2.17	1.09	0.29
76	0.251421	0.009443	1.54	1.46	2.03	4.19	2.54	1.23	0.21
77	0.262238	0.034883	1.39	1.44	2.01	4.16	2.72	1.33	0.18
78	0.266317	0.041685	1.56	1.44	2.01	4.16	2.64	1.29	0.19
79	0.235435	0.005151	1.69	1.39	1.93	4.01	2.51	1.28	0.20
80	0.254638	0.023888	1.29	1.39	1.93	4.01	2.67	1.31	0.18
81	0.230643	0.013070	1.28	1.37	1.91	3.98	2.61	1.28	0.19
82	0.260073	0.035013	1.87	1.34	1.87	3.90	2.43	1.15	0.21
83	0.260746	0.034946	1.29	1.33	1.86	3.87	2.56	1.27	0.19
84	0.230118	0.015597	1.40	1.32	1.84	3.84	2.56	1.66	0.19
85	0.250371	0.009249	1.19	1.31	1.83	3.80	2.59	1.45	0.18
86	0.243387	0.010501	1.19	1.27	1.77	3.69	2.54	1.46	0.18
87	0.235085	0.010391	1.35	1.23	1.72	3.58	2.46	1.21	0.19
88	0.259593	0.021052	1.20	1.23	1.72	3.58	2.56	1.33	0.17
89	0.257691	0.019168	1.47	1.20	1.67	3.48	2.37	1.14	0.20
90	0.267539	0.027551	1.95	1.19	1.65	3.44	2.20	1.01	0.23
91	0.256659	0.019866	1.24	1.15	1.61	3.35	2.43	1.20	0.18
92	0.264030	0.037952	1.21	1.15	1.60	3.34	2.40	1.27	0.18
93	0.246605	0.013341	1.76	1.13	1.58	3.29	1.94	0.98	0.28
94	0.265064	0.035643	1.31	1.13	1.58	3.29	2.46	1.28	0.17
95	0.244946	0.003390	1.10	1.13	1.57	3.28	2.48	1.44	0.17
96	0.266127	0.033489	1.67	1.13	1.57	3.28	2.17	1.05	0.22
97	0.253570	0.007884	1.49	1.13	1.57	3.27	2.23	1.07	0.21
98	0.268871	0.036585	1.39	1.12	1.56	3.24	2.37	1.13	0.18
99	0.234206	0.005697	1.47	1.12	1.56	3.24	2.20	1.06	0.21
100	0.256296	0.013530	1.39	1.10	1.54	3.21	2.26	1.09	0.20
101	0.236708	0.007661	1.35	1.08	1.51	3.15	2.29	1.12	0.19
102	0.255291	0.023880	1.34	1.08	1.51	3.14	2.17	1.08	0.21
103	0.255885	0.027944	1.12	1.08	1.50	3.13	2.40	1.50	0.17
104	0.260104	0.032558	1.24	1.06	1.48	3.09	2.32	1.13	0.18
105	0.232450	0.008312	1.17	1.06	1.47	3.07	2.32	1.22	0.18
106	0.262848	0.033246	1.30	1.06	1.47	3.07	2.32	1.13	0.18
107	0.252952	0.006052	1.62	1.05	1.47	3.06	2.10	1.01	0.22
108	0.264191	0.034555	1.57	1.05	1.46	3.04	1.97	0.99	0.25
109	0.235139	0.006000	1.33	1.05	1.46	3.04	2.23	1.11	0.20
110	0.263147	0.026085	1.45	1.04	1.45	3.03	2.23	1.09	0.19
111	0.257813	0.030005	1.64	1.04	1.45	3.02	2.17	1.04	0.21
112	0.246208	0.004179	1.08	1.03	1.43	2.99	2.37	1.41	0.17
113	0.264467	0.028031	1.35	1.02	1.43	2.97	2.26	1.19	0.19
114	0.265464	0.037962	1.45	1.01	1.41	2.94	2.13	1.04	0.21

Continued on next page

Table C.1 (continued)

ID	l (°)	b (°)	$I_{\nu,peak}$ (mJy/beam)	F_ν (mJy)	M_{raw} ($M_\odot$)	M_{corr} ($M_\odot$)	R_c (0.01 pc)	σ_{dendro} (0.01 pc)	Σ (g cm^{-2})
115	0.263146	0.015036	1.44	1.01	1.41	2.94	2.17	1.05	0.20
116	0.255301	0.024265	1.30	1.00	1.39	2.90	2.10	1.13	0.21
117	0.241951	0.006346	1.44	0.98	1.37	2.85	2.17	1.21	0.19
118	0.254243	0.012476	1.39	0.98	1.37	2.85	2.20	1.06	0.19
119	0.257830	0.028643	1.78	0.97	1.36	2.83	1.76	0.86	0.29
120	0.242733	0.011025	1.24	0.94	1.31	2.74	2.17	1.06	0.19
121	0.243726	0.015833	1.36	0.92	1.28	2.68	2.07	1.04	0.20
122	0.272876	0.027550	1.41	0.92	1.28	2.67	2.10	1.06	0.19
123	0.265168	0.030688	1.31	0.92	1.28	2.67	2.17	1.07	0.18
124	0.256511	0.021915	2.01	0.90	1.25	2.61	1.60	0.80	0.33
125	0.262815	0.014809	1.26	0.89	1.24	2.60	2.13	1.07	0.18
126	0.265919	0.037686	1.20	0.89	1.24	2.58	2.13	1.04	0.18
127	0.256549	0.021613	1.96	0.87	1.22	2.54	1.60	0.89	0.32
128	0.258467	0.021721	1.43	0.87	1.22	2.54	1.90	1.00	0.22
129	0.265241	0.031214	1.38	0.87	1.21	2.53	2.07	1.00	0.19
130	0.260709	0.019080	1.08	0.86	1.20	2.50	2.13	1.14	0.17
131	0.241232	0.014241	1.41	0.86	1.20	2.50	2.04	0.99	0.19
132	0.235345	0.001622	1.67	0.84	1.18	2.46	1.83	0.89	0.23
133	0.265017	0.032966	1.45	0.83	1.16	2.43	1.90	0.98	0.21
134	0.239232	0.011977	1.24	0.83	1.16	2.41	2.07	1.01	0.18
135	0.266496	0.040637	1.02	0.83	1.15	2.40	2.26	1.13	0.15
136	0.264447	0.038031	1.30	0.82	1.14	2.39	2.04	1.01	0.18
137	0.255992	0.024399	1.10	0.82	1.14	2.38	2.10	1.03	0.17
138	0.258212	0.025541	1.48	0.82	1.14	2.38	1.90	0.93	0.21
139	0.261568	0.018520	1.28	0.81	1.13	2.36	1.97	0.97	0.19
140	0.270539	0.031311	1.09	0.79	1.10	2.30	2.10	1.24	0.17
141	0.244664	0.011856	1.29	0.78	1.08	2.26	1.87	0.97	0.21
142	0.260397	0.010416	1.51	0.78	1.08	2.26	1.79	0.89	0.22
143	0.263978	0.039061	1.39	0.75	1.05	2.18	1.94	0.93	0.19
144	0.267106	0.028516	1.28	0.75	1.04	2.17	1.90	0.92	0.19
145	0.258441	0.021235	1.33	0.74	1.03	2.14	1.79	0.91	0.21
146	0.261579	0.021706	1.45	0.73	1.02	2.14	1.68	0.83	0.24
147	0.258241	0.020800	1.13	0.72	1.00	2.09	1.97	0.98	0.17
148	0.265980	0.026872	1.38	0.72	1.00	2.08	1.83	0.87	0.20
149	0.256516	0.021334	1.75	0.71	0.99	2.07	1.55	0.76	0.27
150	0.256142	0.028690	1.10	0.71	0.99	2.07	1.90	0.93	0.18
151	0.268544	0.031675	1.16	0.71	0.98	2.06	1.94	1.04	0.17
152	0.261147	0.011225	1.40	0.71	0.98	2.06	1.79	0.93	0.20
153	0.256410	0.010087	1.26	0.69	0.97	2.02	1.83	0.88	0.19
154	0.259296	0.037020	1.12	0.69	0.97	2.02	1.90	0.94	0.18
155	0.230347	0.010188	1.49	0.68	0.94	1.97	1.76	0.85	0.20
156	0.245419	0.001670	1.28	0.67	0.94	1.95	1.79	0.87	0.19
157	0.244373	0.012005	1.48	0.67	0.93	1.95	1.68	0.81	0.22
158	0.239732	0.011990	1.13	0.66	0.92	1.93	1.87	0.94	0.18
159	0.264594	0.013730	1.39	0.66	0.92	1.93	1.76	0.88	0.20

Continued on next page

Table C.1 (continued)

ID	l (°)	b (°)	$I_{\nu,peak}$ (mJy/beam)	F_{ν} (mJy)	M_{raw} ($M_{\odot}$)	M_{corr} ($M_{\odot}$)	R_c (0.01 pc)	σ_{dendro} (0.01 pc)	Σ (g cm^{-2})
160	0.265892	0.033876	1.37	0.66	0.92	1.92	1.76	0.89	0.20
161	0.262534	0.033316	1.19	0.65	0.91	1.91	1.87	0.93	0.17
162	0.253548	0.030347	1.40	0.65	0.91	1.90	1.76	0.85	0.20
163	0.235465	0.005587	1.18	0.64	0.89	1.85	1.83	0.90	0.18
164	0.259351	0.036588	1.13	0.63	0.87	1.82	1.83	0.92	0.17
165	0.263125	0.028506	1.22	0.62	0.87	1.81	1.79	0.87	0.18
166	0.251896	0.031731	1.25	0.62	0.86	1.81	1.76	0.86	0.19
167	0.260430	0.023680	1.18	0.62	0.86	1.80	1.79	0.89	0.18
168	0.265320	0.017619	1.17	0.62	0.86	1.80	1.79	0.87	0.18
169	0.246054	0.013558	1.22	0.60	0.83	1.74	1.76	0.87	0.18
170	0.236571	0.010218	1.47	0.60	0.83	1.73	1.64	0.81	0.21
171	0.266679	0.031295	1.13	0.59	0.83	1.72	1.79	0.91	0.17
172	0.267101	0.031167	1.12	0.58	0.81	1.68	1.76	0.87	0.17
173	0.267808	0.029264	1.34	0.57	0.80	1.67	1.68	0.83	0.19
174	0.258097	0.025867	1.18	0.55	0.76	1.59	1.64	0.79	0.19
175	0.228373	0.015146	1.28	0.54	0.75	1.57	1.60	0.82	0.20
176	0.257145	0.016451	1.53	0.54	0.75	1.57	1.51	0.72	0.22
177	0.265099	0.020739	1.24	0.53	0.74	1.55	1.64	0.80	0.18
178	0.263646	0.039410	1.08	0.53	0.74	1.54	1.72	0.95	0.17
179	0.263496	0.034827	1.13	0.52	0.73	1.52	1.68	0.83	0.17
180	0.253634	0.031637	1.10	0.51	0.71	1.49	1.68	0.82	0.17
181	0.268484	0.030030	1.22	0.50	0.70	1.47	1.60	0.79	0.18
182	0.246362	0.009060	1.41	0.50	0.70	1.46	1.55	0.78	0.19
183	0.228394	0.017777	1.21	0.49	0.69	1.43	1.55	0.76	0.19
184	0.262505	0.030651	1.19	0.48	0.67	1.41	1.55	0.76	0.19
185	0.260072	0.022600	1.22	0.47	0.65	1.36	1.55	0.76	0.18
186	0.237559	0.012669	1.01	0.47	0.65	1.35	1.64	0.80	0.16
187	0.257954	0.030840	1.14	0.46	0.64	1.33	1.55	0.75	0.18
188	0.254241	0.013554	1.12	0.45	0.63	1.32	1.55	0.75	0.17
189	0.257783	0.013466	1.24	0.45	0.63	1.31	1.51	0.75	0.18
190	0.249132	0.011089	1.34	0.45	0.62	1.30	1.46	0.71	0.19
191	0.263464	0.020470	1.33	0.44	0.62	1.29	1.46	0.71	0.19
192	0.231188	0.012600	1.10	0.44	0.61	1.28	1.55	0.79	0.17
193	0.257869	0.028142	1.16	0.44	0.61	1.28	1.46	0.69	0.19
194	0.255432	0.028120	1.22	0.44	0.61	1.27	1.51	0.75	0.18
195	0.238859	0.006384	1.18	0.44	0.61	1.27	1.51	0.73	0.18
196	0.241696	0.010313	1.16	0.43	0.61	1.26	1.46	0.74	0.19
197	0.261503	0.014936	1.31	0.43	0.60	1.25	1.37	0.66	0.21
198	0.240069	0.005293	1.17	0.43	0.60	1.25	1.46	0.71	0.19
199	0.265761	0.021906	1.13	0.43	0.59	1.24	1.51	0.74	0.17
200	0.252042	0.028962	1.31	0.42	0.59	1.24	1.42	0.69	0.20
201	0.242144	0.004314	1.17	0.42	0.58	1.22	1.46	0.72	0.18
202	0.236027	0.008154	1.06	0.42	0.58	1.21	1.51	0.75	0.17
203	0.265725	0.030223	1.06	0.40	0.55	1.16	1.46	0.70	0.17
204	0.243697	0.006083	1.15	0.39	0.55	1.14	1.42	0.70	0.18

Continued on next page

Table C.1 (continued)

ID	l (°)	b (°)	$I_{\nu,peak}$ (mJy/beam)	F_ν (mJy)	M_{raw} ($M_\odot$)	M_{corr} ($M_\odot$)	R_c (0.01 pc)	σ_{dendro} (0.01 pc)	Σ (g cm^{-2})
205	0.262893	0.013977	1.31	0.39	0.55	1.14	1.37	0.66	0.19
206	0.257684	0.027617	1.13	0.39	0.54	1.13	1.42	0.71	0.18
207	0.257381	0.019850	1.23	0.39	0.54	1.12	1.42	0.68	0.18
208	0.235265	0.007516	1.20	0.39	0.54	1.12	1.42	0.68	0.18
209	0.252537	0.032242	1.15	0.38	0.53	1.11	1.42	0.72	0.18
210	0.265572	0.036117	1.02	0.38	0.52	1.09	1.46	0.72	0.16
211	0.242774	0.004944	1.10	0.36	0.50	1.05	1.37	0.68	0.18
212	0.262980	0.030766	1.08	0.36	0.50	1.04	1.42	0.72	0.17
213	0.233446	0.007947	1.14	0.36	0.50	1.04	1.37	0.67	0.18
214	0.269315	0.035993	0.97	0.35	0.49	1.03	1.46	0.72	0.15
215	0.265590	0.018469	1.06	0.33	0.45	0.95	1.37	0.68	0.16

Table C.2: Cores in Sgr B2-DS. Galactic coordinates for the center position of the core (calculated by astrodendro) are given. Note that the radius R_c is the radius of a circle with the same total area as the core, while σ_{dendro} is the astrodendro radius (as described in Section 3.4.1).

ID	l (°)	b (°)	$I_{\nu,peak}$ (mJy/beam)	F_ν (mJy)	M_{raw} ($M_\odot$)	M_{corr} ($M_\odot$)	R_c (0.01 pc)	σ_{dendro} (0.01 pc)	Σ (g cm^{-2})
1	0.651162	−0.048765	112.00	344.04	756.73	787.67	3.37	1.39	44.42
2	0.656007	−0.040881	107.03	312.94	688.33	718.56	3.13	1.31	46.68
3	0.656907	−0.039534	78.52	213.61	469.84	496.15	4.76	1.56	13.77
4	0.654453	−0.045978	25.96	155.06	341.07	363.97	3.37	1.54	19.92
5	0.653113	−0.038094	61.94	120.96	266.06	286.77	2.69	1.04	24.43
6	0.649557	−0.054456	53.07	118.33	260.26	280.78	4.39	1.47	9.00
7	0.655621	−0.039380	23.87	96.77	212.84	231.81	4.39	1.68	7.35
8	0.654992	−0.039823	67.76	89.07	195.92	214.37	1.90	0.76	36.12
9	0.654827	−0.040507	23.23	72.91	160.37	177.48	3.60	1.39	8.21
10	0.656715	−0.041909	32.73	68.35	150.34	167.00	1.71	0.81	34.01
11	0.653982	−0.041989	39.90	64.85	142.64	158.92	2.86	1.12	11.56
12	0.641769	−0.063329	29.80	53.28	117.19	132.63	2.64	0.94	11.22
13	0.656686	−0.040766	18.73	41.77	91.87	106.05	2.36	1.11	10.94
14	0.647135	−0.055118	27.13	39.21	86.24	100.07	2.08	0.83	13.25
15	0.632166	−0.062780	22.39	37.33	82.11	95.73	2.91	1.04	6.47
16	0.656082	−0.040369	22.48	36.46	80.19	93.72	1.54	0.73	22.42
17	0.649267	−0.052053	17.13	34.31	75.47	88.73	2.96	1.13	5.71
18	0.633379	−0.069538	13.72	29.80	65.55	78.16	2.32	1.03	8.12
19	0.649138	−0.049523	18.05	28.24	62.11	74.46	2.74	1.02	5.50
20	0.653662	−0.043561	10.88	27.96	61.50	73.79	2.45	1.07	6.83
21	0.648592	−0.053232	9.77	27.91	61.38	73.67	2.47	1.07	6.70
22	0.653480	−0.044007	15.78	27.71	60.94	73.20	2.42	0.95	6.93

Continued on next page

Table C.2 (continued)

ID	l (°)	b (°)	$I_{\nu,peak}$ (mJy/beam)	F_ν (mJy)	M_{raw} ($M_\odot$)	M_{corr} ($M_\odot$)	R_c (0.01 pc)	σ_{dendro} (0.01 pc)	Σ (g cm^{-2})
23	0.653448	−0.042257	12.87	27.68	60.89	73.14	2.71	1.13	5.53
24	0.655320	−0.040132	11.62	27.12	59.65	71.80	1.98	0.91	10.10
25	0.653429	−0.046028	7.80	25.60	56.30	68.17	3.13	1.37	3.83
26	0.628974	−0.062909	10.96	24.59	54.08	65.75	2.90	1.17	4.27
27	0.654221	−0.040796	7.92	24.40	53.68	65.31	2.85	1.26	4.41
28	0.654014	−0.041393	21.74	23.76	52.27	63.77	1.43	0.63	16.89
29	0.654216	−0.045098	16.23	22.62	49.76	61.02	1.50	0.71	14.74
30	0.655919	−0.040264	22.43	21.51	47.31	58.32	1.20	0.56	21.81
31	0.631475	−0.062269	15.20	21.46	47.20	58.19	1.97	0.79	8.10
32	0.654431	−0.046555	10.41	21.23	46.69	57.64	1.67	0.83	11.17
33	0.654642	−0.045236	12.75	20.24	44.53	55.23	2.45	1.06	4.92
34	0.657195	−0.041885	16.24	19.68	43.28	53.85	1.18	0.59	20.71
35	0.656634	−0.042354	11.16	19.62	43.15	53.71	2.09	0.90	6.59
36	0.627206	−0.058515	4.01	19.28	42.40	52.87	3.36	1.64	2.50
37	0.654400	−0.047066	11.49	18.53	40.75	51.02	1.67	0.77	9.66
38	0.654094	−0.045320	12.39	17.71	38.96	49.01	1.40	0.67	13.28
39	0.651850	−0.046756	8.93	17.67	38.86	48.90	2.56	1.10	3.93
40	0.655520	−0.045507	10.66	16.97	37.32	47.16	1.78	0.84	7.80
41	0.634752	−0.066263	9.38	16.39	36.06	45.73	1.52	0.74	10.31
42	0.640646	−0.063993	9.45	15.96	35.11	44.67	2.37	0.92	4.16
43	0.631558	−0.062645	5.16	15.90	34.97	44.51	2.46	1.19	3.83
44	0.650989	−0.049941	7.91	15.60	34.32	43.76	2.00	0.90	5.73
45	0.654171	−0.044800	7.52	15.18	33.39	42.70	1.73	0.87	7.42
46	0.634434	−0.066150	12.08	15.10	33.21	42.49	1.39	0.69	11.48
47	0.651358	−0.049526	12.29	15.03	33.05	42.31	1.58	0.70	8.75
48	0.654525	−0.041381	13.82	14.81	32.57	41.76	1.28	0.59	13.29
49	0.632450	−0.069797	8.97	13.89	30.54	39.48	1.93	0.81	5.43
50	0.643181	−0.061458	8.72	13.40	29.48	38.40	1.53	0.76	8.34
51	0.647544	−0.054407	9.63	13.10	28.82	37.71	1.97	0.77	4.95
52	0.654062	−0.046323	7.03	13.00	28.59	37.48	1.67	0.86	6.78
53	0.633920	−0.069349	5.98	12.98	28.54	37.43	1.87	0.88	5.42
54	0.652892	−0.043073	9.20	12.83	28.23	37.10	2.18	0.87	3.95
55	0.643635	−0.061378	4.65	12.15	26.73	35.54	2.47	1.03	2.90
56	0.654498	−0.047426	8.29	11.92	26.21	35.00	1.60	0.75	6.80
57	0.630354	−0.059635	11.77	11.31	24.87	33.59	1.21	0.56	11.25
58	0.646300	−0.055776	7.72	11.08	24.36	33.05	2.00	0.81	4.04
59	0.655070	−0.043222	4.28	11.01	24.21	32.90	2.45	1.06	2.69
60	0.655066	−0.045967	7.82	10.80	23.75	32.41	1.68	0.73	5.58
61	0.652278	−0.050701	5.39	10.57	23.26	31.88	2.09	0.95	3.53
62	0.653201	−0.041367	7.14	10.06	22.14	30.68	1.52	0.70	6.33
63	0.639282	−0.065876	8.81	10.04	22.08	30.61	1.85	0.72	4.29
64	0.653039	−0.041124	7.19	9.95	21.88	30.40	1.50	0.69	6.48
65	0.653092	−0.040261	6.85	9.68	21.30	29.77	1.80	0.78	4.38
66	0.633637	−0.066319	3.59	8.99	19.78	28.12	2.31	1.03	2.46
67	0.630383	−0.060755	2.87	8.75	19.25	27.54	2.48	1.18	2.07

Continued on next page

Table C.2 (continued)

ID	l (°)	b (°)	$I_{\nu,peak}$ (mJy/beam)	F_ν (mJy)	M_{raw} ($M_\odot$)	M_{corr} ($M_\odot$)	R_c (0.01 pc)	σ_{dendro} (0.01 pc)	Σ (g cm^{-2})
68	0.655443	−0.044285	3.50	8.58	18.86	27.11	2.14	0.96	2.75
69	0.656395	−0.044164	7.62	8.51	18.71	26.94	1.36	0.62	6.75
70	0.641014	−0.063801	6.10	8.37	18.42	26.62	1.85	0.84	3.58
71	0.654557	−0.041592	11.28	8.23	18.10	26.27	1.01	0.47	11.85
72	0.653753	−0.044648	6.00	8.11	17.84	25.98	1.58	0.71	4.72
73	0.650937	−0.049576	5.92	8.10	17.82	25.95	1.54	0.76	4.98
74	0.654497	−0.041931	2.45	7.96	17.52	25.62	2.53	1.25	1.82
75	0.632942	−0.069547	4.19	7.79	17.13	25.19	1.95	0.89	2.98
76	0.656581	−0.040240	6.09	7.65	16.83	24.81	1.45	0.67	5.30
77	0.643087	−0.060243	3.94	7.57	16.66	24.59	2.17	0.91	2.34
78	0.651578	−0.046465	6.51	7.20	15.84	23.55	1.63	0.67	3.94
79	0.652136	−0.045976	5.23	7.11	15.63	23.28	1.58	0.70	4.14
80	0.639906	−0.065155	5.26	6.87	15.11	22.61	1.88	0.77	2.85
81	0.654750	−0.047102	5.21	6.87	15.10	22.60	1.56	0.74	4.13
82	0.629300	−0.057957	2.60	6.75	14.85	22.27	2.31	1.13	1.85
83	0.654716	−0.046155	5.77	6.73	14.80	22.20	1.20	0.58	6.82
84	0.644244	−0.058939	3.51	6.64	14.60	21.95	2.16	0.99	2.08
85	0.655054	−0.039604	10.58	6.57	14.45	21.75	0.85	0.41	13.32
86	0.648647	−0.052936	4.34	6.53	14.37	21.65	1.50	0.70	4.26
87	0.654128	−0.040205	7.18	6.51	14.32	21.58	1.46	0.60	4.45
88	0.644312	−0.062946	3.35	6.47	14.24	21.47	2.04	0.90	2.29
89	0.643569	−0.059218	5.21	6.47	14.22	21.46	1.76	0.72	3.05
90	0.656950	−0.041977	19.35	6.43	14.15	21.36	0.59	0.29	27.09
91	0.653566	−0.037937	2.71	6.37	14.02	21.19	1.68	0.98	3.29
92	0.628967	−0.062342	4.39	6.32	13.89	21.03	1.80	0.78	2.86
93	0.650907	−0.046632	6.41	6.22	13.67	20.74	1.49	0.61	4.10
94	0.656640	−0.042669	4.88	6.19	13.62	20.67	1.50	0.68	4.04
95	0.649926	−0.051829	4.13	6.09	13.40	20.39	1.62	0.76	3.40
96	0.639721	−0.064351	3.09	6.00	13.20	20.12	2.29	1.07	1.67
97	0.655610	−0.040929	4.24	5.96	13.10	19.99	1.29	0.65	5.26
98	0.626682	−0.058799	2.39	5.91	12.99	19.85	2.13	1.02	1.90
99	0.629198	−0.063627	5.36	5.68	12.50	19.20	1.32	0.60	4.78
100	0.654133	−0.041213	9.48	5.66	12.45	19.13	0.88	0.42	10.68
101	0.656417	−0.040524	4.81	5.43	11.95	18.47	1.39	0.68	4.13
102	0.642009	−0.060353	3.28	5.24	11.52	17.90	1.90	0.80	2.12
103	0.654976	−0.043663	4.42	5.23	11.51	17.89	1.60	0.68	2.98
104	0.653162	−0.042665	4.32	5.18	11.39	17.72	1.58	0.69	3.01
105	0.630454	−0.059321	6.15	5.02	11.05	17.27	1.03	0.50	6.88
106	0.650463	−0.050646	2.47	4.98	10.96	17.15	1.58	0.80	2.93
107	0.651235	−0.046041	3.18	4.82	10.59	16.66	1.52	0.72	3.03
108	0.656456	−0.044389	5.04	4.80	10.56	16.61	1.12	0.53	5.59
109	0.653113	−0.038649	10.94	4.76	10.46	16.48	0.67	0.33	15.32
110	0.653688	−0.044390	3.07	4.70	10.34	16.32	1.68	0.90	2.43
111	0.654251	−0.036599	3.76	4.66	10.25	16.19	1.39	0.65	3.54
112	0.657412	−0.039612	3.68	4.65	10.22	16.16	1.54	0.68	2.86

Continued on next page

Table C.2 (continued)

ID	l (°)	b (°)	$I_{\nu,peak}$ (mJy/beam)	F_ν (mJy)	M_{raw} ($M_\odot$)	M_{corr} ($M_\odot$)	R_c (0.01 pc)	σ_{dendro} (0.01 pc)	Σ (g cm^{-2})
113	0.641536	−0.060083	2.52	4.61	10.14	16.05	1.67	0.78	2.43
114	0.630506	−0.059572	6.02	4.60	10.11	16.01	0.91	0.45	8.12
115	0.630654	−0.060967	3.22	4.56	10.04	15.91	1.71	0.75	2.29
116	0.651203	−0.048404	12.10	4.54	10.00	15.85	0.63	0.31	16.58
117	0.628248	−0.062551	3.96	4.47	9.84	15.66	1.52	0.66	2.85
118	0.652715	−0.044251	1.34	4.45	9.78	15.58	2.14	1.19	1.42
119	0.651580	−0.049866	5.33	4.37	9.62	15.38	1.13	0.52	4.99
120	0.628037	−0.061176	2.51	4.37	9.62	15.38	1.76	0.80	2.06
121	0.654629	−0.040987	4.98	4.34	9.55	15.29	1.36	0.57	3.44
122	0.654005	−0.043003	4.12	4.30	9.46	15.19	1.47	0.66	2.91
123	0.629128	−0.063832	5.09	4.20	9.24	14.90	1.12	0.51	4.89
124	0.644674	−0.056644	3.78	4.20	9.24	14.90	1.46	0.64	2.87
125	0.648064	−0.052655	2.60	4.16	9.15	14.80	1.74	0.77	2.02
126	0.647162	−0.054858	4.61	4.15	9.12	14.75	1.06	0.51	5.40
127	0.655360	−0.045666	5.82	4.13	9.09	14.71	1.03	0.48	5.66
128	0.652211	−0.046701	1.51	4.12	9.06	14.67	1.83	0.98	1.79
129	0.632153	−0.065823	4.78	4.03	8.87	14.44	1.17	0.53	4.33
130	0.655716	−0.044026	4.78	4.03	8.87	14.44	0.97	0.48	6.31
131	0.652936	−0.045031	1.41	4.00	8.79	14.33	2.00	0.99	1.47
132	0.653122	−0.038515	11.12	3.97	8.73	14.26	0.61	0.30	15.53
133	0.628863	−0.063913	4.09	3.88	8.54	14.02	1.20	0.55	3.94
134	0.654554	−0.047728	2.55	3.86	8.50	13.96	1.43	0.71	2.75
135	0.650882	−0.052378	3.80	3.86	8.50	13.96	1.43	0.62	2.75
136	0.653322	−0.047120	4.24	3.85	8.46	13.91	1.34	0.57	3.14
137	0.629196	−0.060958	3.39	3.83	8.42	13.86	1.56	0.68	2.30
138	0.657561	−0.039893	3.91	3.82	8.41	13.85	1.30	0.59	3.32
139	0.657012	−0.040400	7.45	3.75	8.24	13.63	0.73	0.36	10.25
140	0.653516	−0.042998	4.03	3.74	8.23	13.62	1.35	0.58	3.01
141	0.649114	−0.054696	2.26	3.73	8.20	13.58	1.71	0.82	1.87
142	0.630692	−0.062513	3.20	3.70	8.13	13.49	1.52	0.67	2.33
143	0.654663	−0.043475	1.61	3.67	8.06	13.40	1.87	1.00	1.53
144	0.651906	−0.046086	3.83	3.66	8.05	13.39	1.24	0.57	3.46
145	0.628997	−0.058059	3.68	3.63	7.98	13.29	1.42	0.61	2.65
146	0.641260	−0.063233	2.75	3.59	7.89	13.17	1.71	0.78	1.80
147	0.657084	−0.040271	7.19	3.53	7.77	13.02	0.71	0.35	10.17
148	0.655422	−0.040519	4.89	3.44	7.56	12.75	0.99	0.47	5.08
149	0.631230	−0.062326	3.66	3.41	7.50	12.67	1.30	0.58	2.96
150	0.656315	−0.044614	3.09	3.37	7.41	12.56	1.28	0.60	3.02
151	0.651200	−0.051210	2.29	3.36	7.40	12.54	1.38	0.66	2.59
152	0.650266	−0.050963	3.31	3.31	7.28	12.38	1.14	0.55	3.70
153	0.649760	−0.052464	1.62	3.27	7.19	12.26	1.72	0.83	1.61
154	0.646556	−0.055440	1.48	3.24	7.13	12.18	1.72	0.85	1.60
155	0.640544	−0.061759	1.88	3.23	7.10	12.15	1.77	0.81	1.51
156	0.649873	−0.052140	3.04	3.22	7.09	12.14	1.24	0.58	3.04
157	0.626506	−0.059229	3.14	3.15	6.93	11.92	1.40	0.61	2.36

Continued on next page

Table C.2 (continued)

ID	l (°)	b (°)	$I_{\nu,peak}$ (mJy/beam)	F_ν (mJy)	M_{raw} ($M_\odot$)	M_{corr} ($M_\odot$)	R_c (0.01 pc)	σ_{dendro} (0.01 pc)	Σ (g cm^{-2})
158	0.653667	−0.040789	1.79	3.13	6.89	11.87	1.62	0.78	1.75
159	0.649248	−0.051623	2.27	3.13	6.89	11.87	1.56	0.70	1.88
160	0.644078	−0.062576	1.28	3.10	6.83	11.79	1.92	1.02	1.23
161	0.654970	−0.044689	3.43	3.05	6.71	11.64	1.31	0.56	2.61
162	0.653651	−0.037254	1.83	3.01	6.62	11.51	1.43	0.78	2.14
163	0.651418	−0.047805	3.26	3.00	6.60	11.49	1.02	0.50	4.21
164	0.655096	−0.041652	2.55	2.99	6.59	11.47	1.50	0.70	1.95
165	0.650828	−0.051891	2.96	2.98	6.56	11.43	1.35	0.60	2.40
166	0.655882	−0.044184	4.81	2.92	6.43	11.26	0.82	0.40	6.40
167	0.634031	−0.065681	3.01	2.90	6.39	11.20	1.40	0.60	2.18
168	0.647099	−0.056967	3.32	2.87	6.31	11.09	1.24	0.55	2.71
169	0.642592	−0.060649	1.21	2.86	6.29	11.07	1.90	0.92	1.16
170	0.655111	−0.040227	4.08	2.83	6.22	10.98	0.99	0.47	4.19
171	0.630497	−0.061429	3.22	2.82	6.20	10.95	1.06	0.51	3.67
172	0.656195	−0.044409	2.15	2.79	6.15	10.88	1.32	0.65	2.35
173	0.653463	−0.043684	3.70	2.77	6.09	10.80	0.99	0.47	4.09
174	0.642983	−0.061270	5.44	2.75	6.04	10.74	0.77	0.37	6.84
175	0.653747	−0.046880	2.78	2.72	5.99	10.66	1.32	0.59	2.29
176	0.653851	−0.037102	1.99	2.68	5.90	10.54	1.23	0.61	2.58
177	0.639618	−0.062812	2.71	2.64	5.82	10.43	1.44	0.62	1.86
178	0.655672	−0.041136	4.12	2.64	5.82	10.43	0.86	0.44	5.17
179	0.652813	−0.047260	3.21	2.64	5.81	10.42	1.24	0.55	2.49
180	0.653981	−0.038960	1.21	2.63	5.78	10.38	1.71	1.02	1.32
181	0.653087	−0.039051	3.42	2.56	5.62	10.16	0.92	0.45	4.37
182	0.651151	−0.050932	3.11	2.55	5.61	10.15	1.05	0.50	3.41
183	0.650346	−0.050109	2.99	2.52	5.54	10.05	1.08	0.51	3.13
184	0.630925	−0.062980	2.73	2.45	5.40	9.85	1.30	0.57	2.13
185	0.652766	−0.041397	1.33	2.43	5.35	9.77	1.52	0.99	1.55
186	0.631179	−0.067501	2.20	2.42	5.32	9.74	1.36	0.62	1.92
187	0.650650	−0.050379	2.76	2.41	5.29	9.70	1.07	0.51	3.06
188	0.627333	−0.058159	2.53	2.41	5.29	9.70	1.28	0.57	2.16
189	0.653735	−0.040161	1.42	2.38	5.23	9.61	1.49	0.80	1.57
190	0.630571	−0.059138	2.45	2.35	5.16	9.51	1.05	0.51	3.13
191	0.648936	−0.053873	1.62	2.28	5.02	9.30	1.40	0.68	1.71
192	0.657307	−0.040554	3.11	2.25	4.94	9.19	0.94	0.46	3.73
193	0.653973	−0.044976	4.00	2.22	4.88	9.10	0.80	0.39	5.06
194	0.643769	−0.063177	1.81	2.17	4.77	8.93	1.41	0.63	1.60
195	0.641461	−0.059394	1.13	2.16	4.76	8.91	1.53	0.77	1.35
196	0.654204	−0.036815	2.22	2.15	4.73	8.87	1.11	0.53	2.56
197	0.653299	−0.037763	2.72	2.13	4.69	8.81	0.94	0.47	3.53
198	0.649154	−0.054948	2.27	2.12	4.67	8.78	1.23	0.56	2.04
199	0.653063	−0.039877	1.79	2.11	4.65	8.75	1.17	0.58	2.27
200	0.641345	−0.063537	1.26	2.06	4.53	8.58	1.36	0.70	1.64
201	0.628797	−0.064071	3.15	2.05	4.52	8.55	0.92	0.44	3.51
202	0.652384	−0.047697	1.26	2.02	4.44	8.44	1.48	0.73	1.35

Continued on next page

Table C.2 (continued)

ID	l (°)	b (°)	$I_{\nu,peak}$ (mJy/beam)	F_{ν} (mJy)	M_{raw} ($M_{\odot}$)	M_{corr} ($M_{\odot}$)	R_c (0.01 pc)	σ_{dendro} (0.01 pc)	Σ (g cm^{-2})
203	0.656170	−0.040041	4.03	2.00	4.40	8.39	0.73	0.39	5.48
204	0.655271	−0.045335	3.61	2.00	4.40	8.37	0.78	0.38	4.76
205	0.651416	−0.047264	1.25	1.97	4.33	8.28	1.43	0.71	1.42
206	0.656436	−0.039984	1.65	1.95	4.29	8.21	1.28	0.63	1.75
207	0.640364	−0.061564	1.72	1.92	4.22	8.12	1.40	0.63	1.44
208	0.656188	−0.036648	1.33	1.91	4.19	8.07	1.37	0.69	1.49
209	0.632503	−0.068458	1.98	1.82	4.00	7.78	1.21	0.55	1.81
210	0.650724	−0.050012	2.52	1.80	3.96	7.72	0.91	0.44	3.18
211	0.628635	−0.062440	2.39	1.75	3.85	7.55	1.11	0.50	2.08
212	0.656195	−0.041326	5.09	1.74	3.82	7.51	0.59	0.29	7.32
213	0.656876	−0.041065	2.10	1.73	3.81	7.49	1.02	0.49	2.43
214	0.655515	−0.045803	2.18	1.72	3.79	7.45	0.98	0.48	2.62
215	0.630377	−0.061235	2.59	1.72	3.77	7.43	0.86	0.42	3.35
216	0.653931	−0.044509	2.54	1.67	3.68	7.30	0.90	0.43	3.06
217	0.651084	−0.046876	1.97	1.64	3.61	7.18	1.10	0.52	2.00
218	0.638172	−0.067527	1.60	1.64	3.60	7.17	1.21	0.58	1.63
219	0.650219	−0.051196	2.29	1.64	3.60	7.17	0.88	0.44	3.09
220	0.650845	−0.048245	2.51	1.63	3.59	7.14	0.83	0.41	3.43
221	0.655839	−0.044854	1.18	1.61	3.55	7.08	1.31	0.68	1.38
222	0.639271	−0.064386	1.01	1.61	3.54	7.07	1.51	0.79	1.04
223	0.654203	−0.045705	2.73	1.59	3.50	7.01	0.82	0.40	3.48
224	0.633138	−0.069750	2.11	1.53	3.36	6.80	0.95	0.47	2.46
225	0.632074	−0.066143	1.53	1.51	3.33	6.75	1.11	0.55	1.80
226	0.653294	−0.039855	2.10	1.51	3.32	6.74	0.91	0.46	2.67
227	0.640657	−0.060769	1.86	1.51	3.32	6.73	1.18	0.53	1.59
228	0.643246	−0.064732	1.84	1.50	3.29	6.68	1.13	0.52	1.71
229	0.653298	−0.039692	2.05	1.49	3.28	6.67	0.91	0.45	2.64
230	0.641218	−0.059396	1.22	1.49	3.27	6.65	1.22	0.59	1.45
231	0.653631	−0.041393	1.85	1.48	3.25	6.63	1.10	0.51	1.80
232	0.628421	−0.062420	1.28	1.46	3.20	6.54	1.20	0.58	1.48
233	0.651404	−0.049748	3.14	1.43	3.15	6.46	0.69	0.34	4.35
234	0.652617	−0.045162	1.30	1.39	3.06	6.32	1.17	0.55	1.49
235	0.654530	−0.037458	1.31	1.37	3.01	6.23	1.18	0.57	1.44
236	0.653455	−0.040209	1.40	1.36	2.99	6.20	1.11	0.58	1.62
237	0.649900	−0.050287	1.51	1.34	2.94	6.13	1.12	0.53	1.56
238	0.653297	−0.041804	1.25	1.33	2.93	6.10	1.11	0.59	1.58
239	0.653546	−0.039696	1.39	1.33	2.93	6.10	1.08	0.53	1.66
240	0.644889	−0.062857	1.10	1.31	2.88	6.02	1.22	0.69	1.28
241	0.656024	−0.043008	1.59	1.29	2.83	5.93	1.08	0.52	1.60
242	0.641613	−0.063569	1.58	1.25	2.76	5.81	0.99	0.49	1.85
243	0.649171	−0.054435	1.23	1.25	2.75	5.80	1.12	0.54	1.46
244	0.629592	−0.062662	1.64	1.23	2.72	5.74	1.07	0.50	1.57
245	0.639867	−0.064007	1.14	1.23	2.71	5.73	1.26	0.59	1.14
246	0.651810	−0.044995	1.39	1.21	2.67	5.66	1.08	0.56	1.51
247	0.641689	−0.060268	1.52	1.18	2.60	5.54	0.99	0.48	1.75

Continued on next page

Table C.2 (continued)

ID	l (°)	b (°)	$I_{\nu,peak}$ (mJy/beam)	F_ν (mJy)	M_{raw} ($M_\odot$)	M_{corr} ($M_\odot$)	R_c (0.01 pc)	σ_{dendro} (0.01 pc)	Σ (g cm^{-2})
248	0.633004	−0.063833	0.96	1.18	2.60	5.54	1.20	0.60	1.20
249	0.656692	−0.041135	2.29	1.18	2.59	5.53	0.75	0.37	3.07
250	0.640867	−0.061173	0.97	1.18	2.58	5.52	1.35	0.77	0.95
251	0.651185	−0.050754	2.32	1.17	2.56	5.48	0.77	0.37	2.90
252	0.656644	−0.043209	1.51	1.16	2.56	5.47	0.95	0.47	1.87
253	0.650163	−0.052119	0.98	1.14	2.50	5.37	1.16	0.58	1.25
254	0.650176	−0.050133	2.23	1.14	2.50	5.37	0.80	0.38	2.59
255	0.648459	−0.054651	1.56	1.13	2.48	5.33	1.01	0.47	1.62
256	0.630368	−0.058480	1.48	1.12	2.47	5.32	0.99	0.47	1.66
257	0.651089	−0.045940	1.94	1.09	2.39	5.18	0.80	0.39	2.48
258	0.656662	−0.043010	1.83	1.07	2.36	5.13	0.86	0.42	2.10
259	0.642642	−0.059907	1.76	1.06	2.34	5.09	0.85	0.41	2.16
260	0.655876	−0.045293	1.37	1.06	2.34	5.09	0.98	0.47	1.62
261	0.650200	−0.051464	1.41	1.06	2.33	5.07	0.91	0.45	1.87
262	0.652734	−0.043579	1.59	1.03	2.26	4.95	0.95	0.45	1.65
263	0.644139	−0.062849	1.12	1.02	2.24	4.92	1.08	0.52	1.27
264	0.653605	−0.039922	1.47	1.02	2.24	4.91	0.98	0.46	1.55
265	0.652070	−0.050894	1.50	1.01	2.22	4.88	0.86	0.53	1.97
266	0.657196	−0.040688	3.07	1.01	2.21	4.87	0.59	0.30	4.23
267	0.651257	−0.046915	1.26	0.98	2.16	4.78	0.95	0.46	1.58
268	0.649551	−0.050622	1.29	0.96	2.12	4.71	0.99	0.47	1.43
269	0.650718	−0.047461	1.24	0.95	2.08	4.64	0.99	0.48	1.40
270	0.647990	−0.052330	0.91	0.91	2.00	4.50	1.08	0.56	1.13
271	0.641476	−0.061604	1.03	0.91	1.99	4.48	1.11	0.52	1.08
272	0.653693	−0.038618	1.21	0.89	1.96	4.41	0.98	0.54	1.35
273	0.641018	−0.060021	1.04	0.88	1.94	4.39	1.06	0.51	1.15
274	0.654105	−0.045971	2.12	0.87	1.92	4.34	0.67	0.33	2.81
275	0.651314	−0.050481	1.05	0.86	1.89	4.29	0.99	0.50	1.27
276	0.650503	−0.050094	1.85	0.85	1.87	4.26	0.71	0.35	2.45
277	0.654188	−0.037060	1.23	0.84	1.85	4.22	0.91	0.46	1.48
278	0.651927	−0.045854	1.42	0.84	1.84	4.21	0.83	0.40	1.76
279	0.632706	−0.063571	0.86	0.84	1.84	4.20	1.05	0.53	1.11
280	0.652473	−0.048656	1.22	0.84	1.84	4.20	0.95	0.45	1.34
281	0.652460	−0.047394	1.35	0.82	1.81	4.15	0.91	0.43	1.45
282	0.657365	−0.039978	1.72	0.82	1.80	4.14	0.75	0.37	2.14
283	0.633925	−0.068536	1.17	0.81	1.77	4.08	0.95	0.45	1.30
284	0.651048	−0.053222	1.40	0.81	1.77	4.08	0.85	0.40	1.63
285	0.656811	−0.036566	1.19	0.80	1.77	4.07	0.88	0.43	1.52
286	0.654242	−0.037690	1.05	0.80	1.76	4.06	0.97	0.57	1.25
287	0.632057	−0.065944	2.20	0.79	1.74	4.02	0.63	0.31	2.88
288	0.631856	−0.065886	1.25	0.78	1.71	3.95	0.82	0.41	1.70
289	0.639014	−0.064490	1.02	0.75	1.65	3.83	0.99	0.48	1.11
290	0.654074	−0.036631	1.27	0.74	1.64	3.79	0.82	0.40	1.63
291	0.651134	−0.049378	2.24	0.74	1.62	3.77	0.59	0.29	3.11
292	0.639784	−0.065753	0.91	0.73	1.60	3.71	0.97	0.47	1.14

Continued on next page

Table C.2 (continued)

ID	l (°)	b (°)	$I_{\nu,peak}$ (mJy/beam)	F_ν (mJy)	M_{raw} ($M_\odot$)	M_{corr} ($M_\odot$)	R_c (0.01 pc)	σ_{dendro} (0.01 pc)	Σ (g cm^{-2})
293	0.657020	−0.041258	1.59	0.72	1.59	3.70	0.75	0.37	1.89
294	0.641001	−0.061318	1.13	0.72	1.59	3.69	0.97	0.45	1.13
295	0.642344	−0.059848	0.96	0.71	1.55	3.60	0.97	0.46	1.10
296	0.652126	−0.045708	1.45	0.70	1.54	3.57	0.80	0.38	1.60
297	0.633189	−0.064917	1.07	0.69	1.51	3.50	0.91	0.43	1.21
298	0.628643	−0.061577	1.09	0.67	1.48	3.43	0.86	0.41	1.32
299	0.652520	−0.047882	1.13	0.67	1.47	3.42	0.86	0.41	1.31
300	0.642759	−0.060044	1.54	0.66	1.45	3.36	0.69	0.34	2.00
301	0.631715	−0.065909	1.27	0.65	1.44	3.33	0.75	0.37	1.70
302	0.643658	−0.062226	1.02	0.65	1.43	3.32	0.92	0.44	1.11
303	0.629846	−0.061688	1.08	0.64	1.40	3.25	0.85	0.41	1.29
304	0.653158	−0.042304	1.15	0.63	1.38	3.21	0.80	0.39	1.44
305	0.653485	−0.040962	1.03	0.62	1.36	3.16	0.83	0.41	1.31
306	0.630041	−0.060675	1.14	0.61	1.34	3.11	0.82	0.39	1.33
307	0.648809	−0.054359	1.26	0.60	1.32	3.06	0.78	0.37	1.43
308	0.653349	−0.043506	1.85	0.59	1.30	3.02	0.59	0.29	2.49
309	0.653321	−0.039546	1.76	0.59	1.30	3.02	0.61	0.30	2.31
310	0.644357	−0.059768	0.93	0.59	1.29	3.00	0.88	0.43	1.11
311	0.650875	−0.047711	1.02	0.58	1.27	2.95	0.82	0.40	1.27
312	0.640568	−0.059733	0.91	0.58	1.27	2.94	0.86	0.43	1.13
313	0.647393	−0.053407	1.02	0.56	1.24	2.87	0.80	0.39	1.28
314	0.633907	−0.066034	1.05	0.56	1.24	2.87	0.83	0.39	1.18
315	0.653094	−0.041697	1.09	0.55	1.21	2.81	0.77	0.39	1.37
316	0.652945	−0.046408	0.88	0.55	1.21	2.80	0.83	0.42	1.15
317	0.639005	−0.064659	0.86	0.55	1.21	2.79	0.88	0.43	1.03
318	0.634986	−0.065669	1.11	0.52	1.15	2.68	0.80	0.38	1.20
319	0.631402	−0.061766	1.16	0.52	1.14	2.64	0.75	0.36	1.35
320	0.630928	−0.060847	1.00	0.49	1.07	2.49	0.75	0.36	1.27
321	0.653565	−0.043239	1.40	0.49	1.07	2.48	0.61	0.33	1.90
322	0.654292	−0.042202	1.16	0.49	1.07	2.48	0.73	0.35	1.33
323	0.627349	−0.057975	1.08	0.47	1.04	2.42	0.71	0.34	1.37
324	0.653640	−0.040375	1.15	0.46	1.01	2.34	0.69	0.33	1.39
325	0.653162	−0.043468	1.00	0.45	0.99	2.28	0.71	0.37	1.29
326	0.630333	−0.062582	1.02	0.45	0.98	2.27	0.73	0.35	1.22
327	0.656934	−0.038235	0.98	0.44	0.97	2.24	0.71	0.35	1.27
328	0.634587	−0.065599	0.77	0.38	0.84	1.95	0.75	0.36	1.00
329	0.634998	−0.065880	0.79	0.38	0.83	1.93	0.75	0.36	0.99
330	0.655612	−0.044906	1.02	0.36	0.80	1.85	0.63	0.31	1.32
331	0.654052	−0.043959	0.96	0.35	0.76	1.76	0.65	0.31	1.18
332	0.653270	−0.042855	0.93	0.33	0.73	1.69	0.63	0.31	1.21
333	0.653500	−0.046718	1.01	0.32	0.71	1.65	0.61	0.30	1.27
334	0.655354	−0.039639	1.03	0.31	0.69	1.59	0.61	0.29	1.22
335	0.639797	−0.060339	0.87	0.27	0.59	1.37	0.59	0.28	1.13
336	0.642593	−0.061269	0.67	0.23	0.51	1.19	0.63	0.31	0.85
337	0.641736	−0.061674	0.69	0.20	0.44	1.02	0.59	0.28	0.85

Table C.3: Cores in Sgr C. Galactic coordinates for the center position of the core (calculated by astrodendro) are given. Note that the radius R_c is the radius of a circle with the same total area as the core, while σ_{dendro} is the astrodendro radius (as described in Section 3.4.1).

ID	l (°)	b (°)	$I_{\nu,peak}$ (mJy/beam)	F_ν (mJy)	M_{raw} ($M_\odot$)	M_{corr} ($M_\odot$)	R_c (0.01 pc)	σ_{dendro} (0.01 pc)	Σ (g cm^{-2})
1	359.436048	−0.101738	102.60	275.24	601.96	623.62	6.10	2.28	10.76
2	359.436238	−0.103516	129.50	192.29	420.55	440.63	2.92	1.29	32.76
3	359.441555	−0.103193	23.74	71.13	155.56	170.45	3.62	1.93	7.87
4	359.444070	−0.105303	22.76	68.39	149.58	164.29	4.48	2.07	4.96
5	359.440235	−0.104849	18.11	65.53	143.33	157.84	6.31	2.43	2.39
6	359.441432	−0.105196	25.21	55.31	120.96	134.47	3.79	1.68	5.59
7	359.436552	−0.102944	35.89	45.59	99.70	112.05	2.64	1.17	9.50
8	359.440254	−0.103196	19.26	30.97	67.73	78.38	3.83	1.58	3.06
9	359.452216	−0.106271	17.00	30.27	66.20	76.76	3.21	1.47	4.27
10	359.442441	−0.105701	20.92	26.44	57.83	67.84	2.83	1.20	4.80
11	359.434461	−0.108003	19.87	23.83	52.11	61.68	3.61	1.28	2.65
12	359.440829	−0.110800	7.36	16.61	36.33	44.39	3.83	1.59	1.64
13	359.440388	−0.102297	8.05	14.84	32.46	40.06	2.86	1.45	2.64
14	359.435946	−0.103635	37.58	12.27	26.83	34.22	0.98	0.48	18.49
15	359.442524	−0.102664	6.34	11.19	24.47	31.73	3.22	1.49	1.57
16	359.455302	−0.115455	11.07	10.77	23.55	30.75	2.75	1.06	2.07
17	359.442637	−0.101929	4.99	9.80	21.43	28.47	2.68	1.28	1.98
18	359.447672	−0.102956	7.05	9.68	21.17	28.18	3.05	1.28	1.52
19	359.443028	−0.104266	6.14	8.54	18.68	25.46	3.13	1.28	1.27
20	359.445001	−0.106301	1.92	7.30	15.97	22.22	4.32	2.18	0.57
21	359.440142	−0.102523	5.60	7.19	15.73	21.92	2.15	1.05	2.27
22	359.435819	−0.104636	4.76	6.76	14.79	20.78	2.91	1.25	1.16
23	359.443449	−0.102788	4.80	5.59	12.22	17.59	2.16	1.01	1.74
24	359.435678	−0.102506	3.63	5.22	11.41	16.57	2.60	1.44	1.12
25	359.440355	−0.110846	3.88	5.21	11.39	16.54	2.67	1.17	1.06
26	359.437479	−0.104607	3.87	5.00	10.94	15.97	2.98	1.36	0.82
27	359.453909	−0.105837	2.14	4.54	9.93	14.80	3.31	1.81	0.60
28	359.444316	−0.102774	5.77	4.51	9.86	14.72	1.87	0.85	1.88
29	359.455816	−0.116027	3.65	4.41	9.65	14.47	2.61	1.15	0.94
30	359.437476	−0.101749	1.74	4.22	9.23	13.98	3.27	1.79	0.57
31	359.443575	−0.104219	5.17	4.20	9.19	13.94	2.06	0.92	1.45
32	359.434901	−0.106929	1.83	4.20	9.18	13.93	3.28	1.64	0.57
33	359.438154	−0.100500	3.10	4.13	9.02	13.74	2.28	1.11	1.15
34	359.441735	−0.102744	12.57	4.03	8.82	13.50	0.98	0.49	6.08
35	359.443280	−0.104729	3.53	3.66	8.00	12.53	2.18	0.99	1.12
36	359.441995	−0.105398	5.96	3.54	7.74	12.22	1.39	0.69	2.67
37	359.443350	−0.100040	1.69	3.50	7.65	12.11	2.75	1.43	0.67
38	359.443642	−0.104564	2.83	3.37	7.37	11.77	2.20	1.04	1.02

Continued on next page

Table C.3 (continued)

ID	l (°)	b (°)	$I_{\nu,peak}$ (mJy/beam)	F_ν (mJy)	M_{raw} (M$_\odot$)	M_{corr} (M$_\odot$)	R_c (0.01 pc)	σ_{dendro} (0.01 pc)	Σ (g cm^{-2})
39	359.435369	−0.101004	3.03	3.36	7.35	11.75	2.38	1.16	0.87
40	359.444677	−0.100558	3.13	3.33	7.28	11.66	2.47	1.06	0.80
41	359.433795	−0.103092	2.37	3.10	6.78	11.04	2.33	1.19	0.83
42	359.443097	−0.102648	4.02	2.94	6.43	10.61	1.63	0.78	1.60
43	359.442948	−0.105578	3.51	2.93	6.40	10.58	1.93	0.88	1.15
44	359.444865	−0.105454	6.67	2.92	6.39	10.57	1.22	0.59	2.86
45	359.444881	−0.102714	3.62	2.84	6.21	10.34	1.61	0.79	1.59
46	359.433682	−0.102734	2.76	2.70	5.90	9.95	2.11	1.14	0.88
47	359.434134	−0.101780	2.46	2.66	5.81	9.83	2.18	1.01	0.81
48	359.445308	−0.104179	1.16	2.63	5.76	9.75	3.06	1.63	0.41
49	359.452633	−0.106286	6.00	2.61	5.70	9.68	1.19	0.57	2.69
50	359.440582	−0.110229	1.55	2.60	5.68	9.65	2.64	1.27	0.54
51	359.443937	−0.103545	3.71	2.59	5.67	9.64	1.95	0.83	1.00
52	359.441639	−0.108002	1.44	2.58	5.64	9.59	2.64	1.28	0.54
53	359.433539	−0.105340	1.54	2.51	5.50	9.40	2.51	1.37	0.58
54	359.445738	−0.102180	1.23	2.30	5.03	8.75	2.88	1.47	0.40
55	359.444031	−0.102828	2.14	2.28	4.99	8.69	2.13	1.01	0.73
56	359.444605	−0.102645	3.32	2.25	4.91	8.59	1.47	0.72	1.52
57	359.443029	−0.105927	2.16	2.19	4.79	8.41	1.89	0.91	0.89
58	359.433656	−0.102282	1.56	2.14	4.68	8.26	2.25	1.21	0.62
59	359.455995	−0.115684	1.61	2.10	4.58	8.12	2.26	1.06	0.60
60	359.439925	−0.103360	3.67	2.09	4.57	8.10	1.49	0.70	1.37
61	359.438422	−0.101874	1.63	1.93	4.22	7.60	2.26	1.16	0.55
62	359.435660	−0.100085	2.50	1.86	4.06	7.38	1.81	0.88	0.83
63	359.437908	−0.101287	2.12	1.85	4.04	7.35	1.98	1.19	0.68
64	359.446173	−0.102117	1.09	1.84	4.03	7.33	2.51	1.27	0.42
65	359.443691	−0.107965	1.46	1.79	3.92	7.17	2.11	1.11	0.58
66	359.444255	−0.099791	1.94	1.77	3.87	7.10	2.04	0.93	0.62
67	359.451131	−0.105649	1.29	1.77	3.87	7.10	2.31	1.20	0.48
68	359.434300	−0.101319	1.97	1.74	3.81	7.01	1.93	0.97	0.68
69	359.438503	−0.102462	1.37	1.67	3.65	6.78	2.23	1.14	0.49
70	359.445500	−0.103162	2.42	1.67	3.65	6.78	1.70	0.79	0.84
71	359.438473	−0.100386	2.44	1.65	3.60	6.71	1.49	0.74	1.08
72	359.442608	−0.100014	1.34	1.63	3.56	6.64	1.93	1.00	0.64
73	359.435952	−0.100856	2.52	1.60	3.50	6.56	1.47	0.73	1.08
74	359.434339	−0.107216	1.03	1.58	3.45	6.49	2.31	1.15	0.43
75	359.438395	−0.103820	1.55	1.53	3.34	6.33	2.13	1.07	0.49
76	359.442697	−0.103711	1.72	1.53	3.34	6.32	1.98	0.90	0.56
77	359.438306	−0.106190	1.57	1.52	3.33	6.31	1.81	0.87	0.68
78	359.445934	−0.104726	1.05	1.46	3.19	6.11	2.18	1.08	0.45
79	359.434269	−0.106314	1.12	1.44	3.15	6.05	2.20	1.14	0.43
80	359.443198	−0.103585	2.21	1.40	3.07	5.92	1.61	0.75	0.79
81	359.437815	−0.106053	2.14	1.39	3.04	5.89	1.54	0.74	0.85
82	359.440788	−0.109670	0.98	1.39	3.04	5.89	2.16	1.11	0.43
83	359.439291	−0.102489	1.26	1.33	2.92	5.70	1.98	0.96	0.49

Continued on next page

Table C.3 (continued)

ID	l (°)	b (°)	$I_{\nu,peak}$ (mJy/beam)	F_ν (mJy)	M_{raw} ($M_\odot$)	M_{corr} ($M_\odot$)	R_c (0.01 pc)	σ_{dendro} (0.01 pc)	Σ (g cm^{-2})
84	359.434018	−0.104381	1.44	1.30	2.84	5.58	1.85	0.90	0.55
85	359.437795	−0.100326	1.74	1.27	2.77	5.49	1.57	0.97	0.75
86	359.446222	−0.104968	1.32	1.26	2.75	5.44	1.85	0.94	0.53
87	359.439637	−0.105417	1.11	1.23	2.69	5.36	2.02	1.08	0.44
88	359.437918	−0.103225	1.01	1.23	2.69	5.36	2.09	1.07	0.41
89	359.438716	−0.106042	1.33	1.21	2.65	5.30	1.74	1.02	0.58
90	359.433948	−0.105980	1.29	1.19	2.59	5.22	1.83	0.92	0.52
91	359.433586	−0.101981	1.55	1.18	2.58	5.20	1.63	0.85	0.64
92	359.433834	−0.101457	1.46	1.18	2.57	5.18	1.63	0.83	0.64
93	359.438352	−0.100885	2.15	1.15	2.52	5.11	1.39	0.67	0.87
94	359.452733	−0.104195	1.74	1.15	2.51	5.09	1.59	0.75	0.66
95	359.447505	−0.104297	1.16	1.12	2.44	4.99	1.77	1.05	0.52
96	359.442216	−0.101882	3.37	1.07	2.35	4.84	0.98	0.47	1.62
97	359.445810	−0.105769	1.06	1.05	2.29	4.75	1.85	1.14	0.45
98	359.446404	−0.105708	1.45	1.03	2.26	4.70	1.61	0.76	0.58
99	359.435058	−0.102269	1.26	1.03	2.25	4.69	1.77	0.89	0.48
100	359.446593	−0.105152	1.25	0.99	2.16	4.55	1.68	0.90	0.51
101	359.447940	−0.104201	1.51	0.98	2.14	4.51	1.49	0.73	0.64
102	359.444392	−0.106226	1.32	0.98	2.14	4.51	1.68	0.80	0.50
103	359.435566	−0.106619	1.34	0.93	2.02	4.34	1.66	0.84	0.49
104	359.441740	−0.107751	1.00	0.90	1.97	4.26	1.70	0.88	0.45
105	359.441705	−0.101077	1.14	0.87	1.91	4.15	1.66	0.83	0.46
106	359.443490	−0.105610	2.11	0.84	1.83	4.03	1.12	0.55	0.96
107	359.438056	−0.105919	1.55	0.82	1.80	3.99	1.28	0.63	0.73
108	359.438545	−0.106296	1.49	0.79	1.73	3.82	1.33	0.65	0.65
109	359.438837	−0.102937	1.49	0.78	1.70	3.76	1.44	0.67	0.54
110	359.443233	−0.103844	1.65	0.75	1.64	3.63	1.28	0.61	0.67
111	359.434212	−0.105346	1.09	0.72	1.57	3.47	1.49	0.76	0.47
112	359.441131	−0.109652	1.16	0.72	1.57	3.46	1.49	0.72	0.47
113	359.433670	−0.106285	1.58	0.71	1.55	3.42	1.22	0.59	0.69
114	359.442931	−0.099942	1.37	0.69	1.51	3.34	1.25	0.62	0.64
115	359.439390	−0.104847	1.47	0.68	1.49	3.29	1.36	0.64	0.53
116	359.438797	−0.108280	1.08	0.65	1.43	3.15	1.42	0.72	0.47
117	359.443470	−0.106156	1.23	0.65	1.41	3.12	1.25	0.66	0.60
118	359.442805	−0.112231	1.31	0.63	1.37	3.03	1.25	0.60	0.58
119	359.433743	−0.104912	1.17	0.61	1.34	2.96	1.33	0.67	0.50
120	359.437994	−0.101774	1.18	0.60	1.32	2.91	1.33	0.65	0.49
121	359.444748	−0.099970	0.88	0.60	1.30	2.88	1.49	0.73	0.39
122	359.439902	−0.106590	1.25	0.59	1.29	2.86	1.31	0.63	0.50
123	359.446363	−0.104761	1.02	0.59	1.29	2.85	1.33	0.66	0.48
124	359.440305	−0.100462	1.66	0.57	1.25	2.76	1.09	0.52	0.70
125	359.437519	−0.106011	1.45	0.57	1.24	2.75	1.16	0.55	0.62
126	359.446557	−0.106841	1.76	0.57	1.24	2.74	1.02	0.50	0.79
127	359.435170	−0.102842	0.92	0.56	1.21	2.69	1.39	0.84	0.42
128	359.447782	−0.101616	1.21	0.55	1.21	2.68	1.22	0.58	0.54

Continued on next page

Table C.3 (continued)

ID	l (°)	b (°)	$I_{\nu,peak}$ (mJy/beam)	F_ν (mJy)	M_{raw} ($M_\odot$)	M_{corr} ($M_\odot$)	R_c (0.01 pc)	σ_{dendro} (0.01 pc)	Σ (g cm^{-2})
129	359.433825	−0.105482	1.22	0.55	1.20	2.65	1.25	0.61	0.51
130	359.447827	−0.102206	1.34	0.54	1.18	2.60	1.16	0.55	0.59
131	359.438065	−0.102235	1.32	0.52	1.15	2.54	1.25	0.59	0.49
132	359.438069	−0.101039	1.48	0.51	1.12	2.48	1.09	0.54	0.63
133	359.438974	−0.103466	1.07	0.51	1.11	2.46	1.33	0.63	0.42
134	359.445300	−0.102901	1.31	0.50	1.10	2.44	1.12	0.54	0.58
135	359.447893	−0.101911	1.33	0.50	1.09	2.42	1.12	0.54	0.58
136	359.447580	−0.104670	1.19	0.50	1.09	2.40	1.16	0.59	0.54
137	359.446367	−0.102739	1.02	0.50	1.08	2.40	1.31	0.64	0.42
138	359.437140	−0.105172	1.02	0.49	1.07	2.37	1.28	0.63	0.44
139	359.433850	−0.106486	1.35	0.49	1.07	2.35	1.06	0.52	0.64
140	359.437858	−0.107866	1.17	0.48	1.06	2.33	1.12	0.56	0.56
141	359.437660	−0.107749	1.19	0.48	1.05	2.33	1.12	0.58	0.56
142	359.446815	−0.103119	0.98	0.48	1.05	2.32	1.28	0.62	0.43
143	359.438909	−0.100902	1.23	0.46	1.01	2.24	1.12	0.60	0.53
144	359.446550	−0.103038	0.83	0.44	0.96	2.11	1.31	0.77	0.37
145	359.446945	−0.102511	1.01	0.43	0.94	2.08	1.19	0.57	0.44
146	359.439195	−0.105407	0.95	0.41	0.89	1.97	1.19	0.59	0.42
147	359.438136	−0.101677	1.13	0.40	0.88	1.95	1.09	0.53	0.49
148	359.439005	−0.106160	1.21	0.40	0.88	1.93	1.02	0.50	0.56
149	359.438109	−0.104392	1.03	0.40	0.87	1.92	1.16	0.55	0.43
150	359.445736	−0.101553	0.81	0.39	0.86	1.91	1.25	0.60	0.37
151	359.433924	−0.107026	0.89	0.36	0.78	1.73	1.12	0.55	0.41
152	359.442182	−0.101597	1.03	0.35	0.76	1.68	1.02	0.50	0.49
153	359.438415	−0.101238	1.00	0.34	0.74	1.63	1.02	0.49	0.47
154	359.437274	−0.106260	1.05	0.34	0.73	1.62	1.02	0.49	0.47
155	359.446319	−0.102965	0.80	0.32	0.71	1.57	1.12	0.55	0.37
156	359.445194	−0.102368	0.87	0.32	0.71	1.56	1.12	0.54	0.37
157	359.435774	−0.105354	1.05	0.30	0.66	1.45	0.98	0.47	0.45
158	359.438980	−0.104069	0.82	0.26	0.57	1.27	1.02	0.50	0.37
159	359.439671	−0.104095	0.77	0.23	0.51	1.13	0.98	0.49	0.35

DEPARTMENT OF SPACE, EARTH AND ENVIRONMENT
CHALMERS UNIVERSITY OF TECHNOLOGY
Gothenburg, Sweden
www.chalmers.se

CHALMERS
UNIVERSITY OF TECHNOLOGY